UNDERSTANDING THE GLOBAL IMPACTS OF BIOMASS BURNING AEROSOLS AND MARINE BIOGENIC VOC

A Dissertation
Presented to
The Academic Faculty

by

Aoxing Zhang

In Partial Fulfillment
of the Requirements for the Degree
Doctor of Philosophy in the
School of Earth and Atmospheric Sciences

Georgia Institute of Technology
May 2020

UNDERSTANDING THE GLOBAL IMPACTS OF BIOMASS BURNING AEROSOLS AND MARINE BIOGENIC VOC

Approved by:

Dr. Yuhang Wang, Advisor
School of Earth and Atmospheric Sciences
Georgia Institute of Technology

Dr. Lewis G. Huey
School of Earth and Atmospheric Sciences
Georgia Institute of Technology

Dr. Rodney Weber
School of Earth and Atmospheric Sciences
Georgia Institute of Technology

Dr. Nga Lee Ng
School of Chemical & Biomolecular Engineering
Georgia Institute of Technology

Dr. Yi Deng
School of Earth and Atmospheric Sciences
Georgia Institute of Technology

Date Approved: March 13, 2020

To my maternal grandmother, who didn’t make it until I graduate.

ACKNOWLEDGEMENTS

I would like to especially thank my mother and father, without whose support I could not be here, and my girlfriend who supports and accompanies me everywhere in my life. I want to thank Dr. Tzung-May Fu and Dr. Lei Zhu at Southern University of Science and Technology, Dr. Yongyun Hu at Peking University and Dr. Daniel Jacob at Harvard University for the academic advises in my undergraduate career and for being my referrer in my graduate school applications. I would like to thank Dr. Rodney Weber, Linghan Zeng and Haviland Forrister for great ideas and discussions for the brown carbon modelling studies. Also, I need to thank Dr. Leonardo Alvarado at University of Bremen for helpful suggestions and contribution for understanding glyoxal satellite retrieval data, and thank Dr. Cenlin He, Dr. Simone Tilmes, Dr. Danial Marsh, Dr. Jean-Francois Lamarque, Dr. Jason Knievel and Dr. Rajesh Kumar at NCAR for helpful discussions for my research project.

The most importantly, I want to thank my advisor, Dr. Yuhang Wang, my current and previous groupmates, Dr. Yongjia Song, Dr. Yuzhong Zhang, Dr. Yufei Zou, Dr. Ziming Ke, Dr. Ruixiong Zhang, Dr. Jianfeng Li, Dr. Ye Cheng, Charles Smeltzer, Hang Qu, Qiyang Yan, Kezhen Chong, Fanghe Zhao, Shengjun Xi, and my comprehensive exam and defense committee members, Dr. Rodney Weber, Dr. Lewis G. Huey, Dr. Nga Lee Ng, Dr. Josef Dufek and Dr. Yi Deng, for the review of my proposal and thesis, and all helpful suggestions for my research. I sincerely appreciate the tremendous support of all individuals and organizations during my Ph.D. degree studies.

TABLE OF CONTENTS

LIST OF TABLES

LIST OF FIGURES

LIST OF SYMBOLS AND ABBREVIATIONS

Symbols

A	light absorption
C	concentration
CO	carbon monoxide
CH_3CN	acetonitrile
E	emission rate
Fe(III)	iron in its +3 oxidation state
Fe_2O_3	iron(III) oxide
HCN	hydrogen cyanide
H_2O_2	hydroperoxide
HO_x	hydroxyl radical and hydroperoxyl radical
HO_2	hydroperoxyl radical
k	the imaginary part of refractive index
NO	nitric oxide
NO_x	nitrogen oxides
OH	hydroxyl radical
O_3	ozone
R^2	the coefficient of determination
SO_2	sulfur dioxide
λ	wavelength
ρ	particle density

Abbreviations

AAE	absorption Angström exponent

AAOD	absorption aerosol optical depth
AERONET	the Aerosol Robotic Network
AOD	aerosol optical depth
ATom	the Atmospheric Tomography Mission
BB	biomass burning
BC	black carbon
BF	burned fraction
BrC	brown carbon
CAM5	the Community Atmosphere Model version 5
CCN	cloud condensation nuclei
CESM	the Community Earth System Model
CLM4.5	the Community Land Model version 4.5
CRUNCEP	the Climate Research Unit and National Centers for Environmental Prediction between 1991 and 2010
DC3	Deep Convective Clouds and Chemistry Project
DJF	December, January and February
DRE	direct radiative effect
DRF	direct radiative forcing
ECLIPSE	the Evaluating the Climate and Air Quality Impacts of Short-lived Pollutants
GCM	Global climate model
GEOS	Goddard Earth Observing System
GFED4	the Global Fire Emissions Database 4
GFED4s	the Global Fire Emission Database version 4 including small fires
GHG	greenhouse gases
GOME-2A	the Global Ozone Monitoring Experiment–2A

HIAPER	High-Performance Instrumented Airborne Platform for Environmental Research
HIPPO	HIAPER (High-Performance Instrumented Airborne Platform for Environmental Research) Pole-to-Pole Observations
HULIS	humic-like substances
IPCC AR5	the Intergovernmental Panel on Climate Change Fifth Assessment Report
JJA	June, July and August
MAE	Mass Absorption Efficiency
MAM	March, April and May
MAM3	3-mode version of the modal aerosol model
MBL	marine boundary layer
MISR	the Multi-angle Imaging SpectroRadiometer
MODIS	Moderate Resolution Imaging Spectroradiometer
MMC	the Mean Meridional Circulation
NMHC	non-methane hydrocarbon
NN	neural network
OA	organic aerosols
OC	organic carbon
OMI	the Ozone Monitoring Instrument
PC	principal-component
PSD	power spectral density
RESFire	the REgion-Specific ecosystem feedback Fire model
RRTMG	the Rapid Radiative Transfer Method for GCMs
SCIAMACHY	the SCanning Imaging Absorption spectroMeter for Atmospheric CHartographY
SEAC4RS	Studies of Emissions, Atmospheric Composition, Clouds and Climate Coupling by Regional Surveys

SOA	secondary organic aerosols
SON	September, October and November
SP2	single-particle soot photometer
VCD	vertical column density
VOC	volatile organic carbon
WSOC	water-soluble organic carbon

SUMMARY

The emission, transport, and impact of biomass burning aerosols and the oxidation state of the marine boundary layer (MBL) play significant roles in understanding the background climate condition and atmospheric circulation. Biomass burning is provoked by natural factors or humans and has a profound impact on ecosystems, carbon cycles, climate change, and human society. Biomass burning is one major source of atmospheric aerosols, which is a potential medium in fire-climate interactions because of its role in the global radiative balance and cloud processing. The understanding of biomass burning emissions and its interaction with atmosphere and ecosystems is essential for estimating the climate impact due to biomass burning. The MBL volatile organic carbon (VOC) strongly impacts the oxidation state MBL, especially over the remote regions. For example, glyoxal, a mid-product in biogenic organic carbon emission, can be photolyzed to produce HO2 radicals, which increases the atmospheric oxidation state and affects various oxidation processes such as ozone production. This study focuses on the modeling approach of the effect of marine glyoxal on the MBL atmosphere oxidation state, local weather and global radiative effect using the Community Earth System Model (CESM),

Carbonaceous aerosols significantly affect global radiative forcing and climate through absorption and scattering of sunlight. Black carbon (BC) and brown carbon (BrC) are light-absorbing carbonaceous aerosols. The direct radiative effect (DRE) of BrC is uncertain. A recent study suggests that BrC absorption is comparable to BC in the upper troposphere over biomass burning regions and that the resulting radiative heating tends to stabilize the atmosphere. Yet current climate models do not include proper physical and

chemical treatments of BrC. In this study, we derived a BrC global biomass burning emission inventory on the basis of the Global Fire Emissions Database 4 (GFED4), developed a module to simulate the light absorption of BrC in the Community Atmosphere Model version 5 (CAM5) of Community Earth System Model (CESM) model, and investigated the photo-bleaching effect and convective transport of BrC on the basis of Studies of Emissions, Atmospheric Composition, Clouds and Climate Coupling by Regional Surveys (SEAC4RS) and Deep Convective Clouds and Chemistry Project (DC3) measurements. The model simulations of BC were also evaluated using HIAPER (High-Performance Instrumented Airborne Platform for Environmental Research) Pole-to-Pole Observations (HIPPO) measurements. We found that globally BrC is a significant absorber, the DRE of which is 0.10 W/m2, more than 25% of BC DRE (+0.39 W/m2). Most significantly, model results indicated that BrC atmospheric heating in the tropical mid and upper troposphere is larger than that of BC. The source of tropical BrC is mainly from wildfires, which are more prevalent in tropical regions than higher latitudes and release much more BrC relative to BC than industrial sources. While BC atmospheric heating is skewed towards the northern mid-latitude lower atmosphere, BrC heating is more centered in the tropical free troposphere. A possible mechanism for the enhanced convective transport of BrC is that hydrophobic high molecular weight BrC becomes a larger fraction of the BrC and less easily activated in a cloud as the aerosol ages. The contribution of BrC heating to the Hadley circulation and latitudinal expansion of the tropics is likely comparable to BC heating.

The effects of climate on wildfires and those of wildfires on climate have been a focus of attention, while little is known how the feedbacks between wildfires and climate

affect the climate system behaviors. The REgion-Specific ecosystem feedback Fire (RESFire) model, implemented in the Community Earth System Model (CESM), allows us to examine the responses of wildfires and climate to their interactions. We find that wildfire-climate interactions due to aerosols tend to decrease precipitation in Africa. With the short-term (days-weeks) aerosol effects, the climate responses can be interseasonal and interannual. The wildfire-climate interaction triggers a positive feedback loop consisting of the wildfire induced precipitation change and the burning caused by drought. This effect is found significantly over Africa with a clear interseasonal and intraseasonal increase of burning.

For a better understanding of the MBL oxidation state, we estimate the marine glyoxal production using inverse modeling in CAM5, the atmospheric module in CESM. When satellite observations show significant glyoxal column concentration over the ocean, current atmospheric chemistry models could not produce glyoxal over the marine boundary layer (MBL) with only continental VOC emissions. We analyzed the relationships among observed marine glyoxal, sea surface chlorophyll-A concentration and model-simulated sea surface downward solar radiation. The high spatial correlation between glyoxal and chlorophyll-A and the high temporal correlation between monthly mean glyoxal and solar radiation shows that MBL glyoxal is probably related to the photochemistry of marine biogenic VOC emissions. This is the first approach to estimate marine glyoxal production based on satellite observation and aircraft measured vertical profile. Our estimation of 43 ± 10 Tg/yr marine glyoxal production is comparable with the land glyoxal budget estimated in the previous study. The simulation results show good agreement with both satellite observations and in-situ measurements. This estimation leads to a significant enhancement

of the oxidation state over the MBL, especially over the Southern Ocean, where marine glyoxal increased 33.0% of HO2, 51.7% of H2O2 and 51.5% of non-methane hydrocarbon (NMHC) oxidation reactivity. This enhancement of the MBL oxidation state further affects atmosphere acidity by accelerating SO_2 oxidation.

CHAPTER 1. INTRODUCTION

1.1 Overview

Biomass burning aerosols and the oxidation state of the marine boundary layer (MBL) play significant roles in the atmospheric circulation and chemical cycle, especially in understanding the background climate condition of the remote regions. Biomass burning is provoked by natural factors or humans and has a profound impact on ecosystems(W. J. Bond, Woodward, & Midgley, 2005), carbon cycles (Ciais et al., 2014), climate change (Bowman et al., 2009) and human society (Moritz et al., 2014). Although the increase of population and land-use conversion lead to a suppress of fire (Andela et al., 2017; Arora & Melton, 2018), biomass burning in the global warming scenario is predicted to increase in the future (Kloster, Mahowald, Randerson, & Lawrence, 2012). Global warming can increase the future annual mean burned area in the western United States by 54%(Spracklen et al., 2009) indicating that the climate effects on fire will be stronger in the future(Pechony & Shindell, 2010). The understanding of biomass burning and its interaction with atmosphere and ecosystems is essential for estimating the climate impact due to biomass burning. On the other hand, the MBL volatile organic carbon (VOC) strongly impacts the MBL oxidation state. For example, glyoxal, a mid-product in biogenic organic carbon emission, can be photolyzed to produce HO_2 radicals, which increase the atmospheric oxidation state and affect various oxidation processes such as ozone production.

Biomass burning is one major source of aerosols (Dentener et al., 2006). Atmospheric Aerosol is a potential medium in fire-climate interactions because of its role in the global radiative balance(Ciais et al., 2014) and cloud processing (Andreae &

Rosenfeld, 2008). Previous studies (Tosca, Diner, Garay, & Kalashnikova, 2015) hypothesized a positive feedback loop between fire, cloud, and precipitation. Atmospheric model studies have focused on the perturbation from fire emission to the regional weather and global climate, but not considering the feedback from the climate back to fire (Ward et al., 2012); most fire models consider only the impact and mechanism from weather to fire (Hantson et al., 2016). The understanding of this feedback loop, thus how the climate response to fire aerosols impact burning, is important but limited.

Carbonaceous aerosols, such as black carbon (BC) and organic carbon (OC), contribute to global atmospheric radiative forcing by scattering and absorbing solar radiation. BC warms the atmosphere by directly absorbing solar radiation (T. C. Bond et al., 2013). OC used to be thought to cool the atmosphere due to its light scattering properties. However, some OC, known as "brown carbon" (BrC), absorbs visible light with a wavelength dependence; the efficiency increases rapidly with decreasing wavelength (Hecobian et al., 2010; T. Kirchstetter & Thatcher, 2012; T. W. Kirchstetter, Novakov, & Hobbs, 2004; M. Yang, Howell, Zhuang, & Huebert, 2009). Laboratory and field studies showed a reduction of BrC absorption when exposed to light, which is usually referred to as "photo-bleaching" (Zhao et al., 2015). Results from the Deep Convective Clouds and Chemistry Project (DC3) found high concentrations of BrC in the continental upper tropospheric due to convective transport, suggesting more efficient atmospheric vertical transport of BrC than previously assumed (Y. Zhang et al., 2017). Previous model estimations of BrC DRE and direct radiative forcing (DRF) treated BrC

similar to BC or considered the photo-bleaching effect, but the deep convective transport effect has not been included.

Glyoxal is one of the smallest bi-carbonyl compounds and is an important factor in atmosphere photochemical oxidation, secondary organic aerosols (SOA) formation (J. Liggio, S.-M. Li, & R. McLaren, 2005a; J. Liggio, S. M. Li, & R. McLaren, 2005b), ozone production (Edwards et al., 2014), and BrC (Shapiro et al., 2009). The source of glyoxal over the continent is both biogenic and anthropogenic. Two of the major precursors of glyoxal are isoprene (biogenic) and acetylene (anthropogenic) (Z. Liu et al., 2012). The major chemical sink of glyoxal is against oxidation (by OH) and photolysis, with a short lifetime of 1~2 hrs. Evidences from in-situ and satellite observations show the widespread distribution of glyoxal over marine boundary layer (MBL) in both coastal sites (Seaman, Charles, & Cahill, 2006; Sinreich et al., 2007) and remote regions (Coburn et al., 2014; Lawson et al., 2015), indicating a potentially large marine source of glyoxal. This source has been missed in current global model simulations (Fu et al., 2008; Lerot, Stavrakou, Smedt, Müller, & Roozendael, 2010), remaining the effect of marine glyoxal to atmospheric oxidation state unknown.

1.2 Outline

CHAPTER 1 introduces the background of this study. This study focuses on the modeling approach of the effect of marine glyoxal on the MBL atmosphere oxidation state, and the impact of biomass burning on local weather and global radiative effect using the Community Earth System Model (CESM).

In CHAPTER 2, we present an estimation of the direct radiative effect (DRE) of brown carbon (BrC), the largest source of which is biomass burning. The BrC DRE (0.10 W/m^2) is estimated to be 25% of that of BC. In the tropics when convective transport is active, contribution to BrC DRE is potentially larger than BC DRE. BrC DRE tends to be larger in the tropics due to different emission distributions and larger BrC levels in the upper troposphere. BrC heating reduces global precipitation by 0.9%, about 60% of the BC induced precipitation decrease. Over the tropics, the reduction of precipitation due to BrC heating is similar to BC heating. The effect of BrC heating on tropical expansion is comparable to BC heating.

CHAPTER 3 describes the study of the impact of the African biomass burning aerosol on the local and regional weather and its feedback on the future biomass burning. We use the Region-Specific ecosystem feedback Fire (RESFire) model in CESM. We find that in Africa, wildfire enhances itself, and the feedback shifts to the region on the transport path of biomass burning aerosols, and regions over which the burning is sensitive to precipitations. This positive feedback is recurrent in a meteorological time scale and has intraseasonal to interseasonal impact.

In CHAPTER 4, we estimate the missing source of MBL glyoxal and discuss the impact of marine glyoxal to the MBL oxidation state. Our estimation of 43 ± 10 Tg/yr marine glyoxal production is comparable with the land glyoxal budget. The CESM model simulation including the MBL glyoxal production shows better agreement with ship and aircraft glyoxal observation over the MBL. We find that MBL glyoxal significantly increases the concentration of oxidants in MBL (e.g. HO_x and H_2O_2), and further increase the MBL acidity.

CHAPTER 5 summarizes the findings in the studies shown in CHAPTERS 2 to 4, and propose future work on the basis of the studies.

CHAPTER 2. MODELING GLOBAL RADIATIVE EFFECT OF BROWN CARBON

2.1 Introduction

Carbonaceous aerosols, including BC and OC, are important factors in global atmospheric radiative forcing. BC warms the atmosphere by directly absorbing solar radiation (T. C. Bond et al., 2013). OC used to be thought to cool the atmosphere due to its light scattering properties. However, some OC, known as "brown carbon" (BrC), absorbs visible light with a wavelength dependence; the efficiency increases rapidly with decreasing wavelength (Hecobian et al., 2010; T. Kirchstetter & Thatcher, 2012; T. W. Kirchstetter et al., 2004; M. Yang et al., 2009).

The primary source of BrC is incomplete combustion of biomass and biofuel (Chakrabarty et al., 2010; Desyaterik et al., 2013; Feng, Ramanathan, & Kotamarthi, 2013; Washenfelder et al., 2015). There is evidence that BrC is also associated with fossil fuel combustion and urban emissions (Costabile et al., 2017; Xie, Hays, & Holder, 2017; Yan et al., 2017; X. Zhang et al., 2011) Secondary BrC is mainly produced from the photo-oxidation of volatile organic compounds (VOCs), such as nitrophenols and aromatic carbonyls (Jacobson, 1999; Tomoki Nakayama et al., 2010; T Nakayama et al., 2013), monoterpenes (J. Laskin et al., 2014), and methylglyoxal (Sareen, Moussa, & McNeill, 2013). Secondary BrC also comes from aqueous-phase reactions in droplets (Nguyen et al., 2012; Updyke, Nguyen, & Nizkorodov, 2012) and homogenous and heterogeneous

reactions of catechol (Magalhães, Esteves da Silva, & Pinto da Silva, 2017; Pillar, Camm, & Guzman, 2014; Pillar & Guzman, 2017) and phenolic compounds (Lavi et al., 2017; Smith, Kinney, & Anastasio, 2016; L. Yu et al., 2016). BrC from biomass burning contributes more to light absorption than the other sources (Chakrabarty et al., 2010; T. Kirchstetter & Thatcher, 2012; McMeeking, 2008; Saleh et al., 2014). Factor analysis of water-soluble organic carbon (WSOC) over the southeastern United States averaged for one year (Hecobian et al., 2010) attributed ~50% of solar absorption at 365 nm to biomass burning emissions, 20-30% to secondary organic carbon, and ~10% to primary urban emissions (mobile sources).

Alexander, Crozier, & Anderson (2008) analyzed the radiative effects of aerosols in the outflow region of East Asia and found that wood smoke BrC accounted for 14% of total aerosol absorption. Liu et al. (2014) found a ~20% reduction of aerosol cooling from BrC absorption at the top of the atmosphere on the basis of measured BrC vertical profiles. However, current observations do not provide enough constraints on the global BrC radiative forcing (Schuster, Dubovik, & Arola, 2016; Schuster, Dubovik, Arola, Eck, & Holben, 2016).

Global models have been applied to estimate Direct Radiative Forcing (DRF) and Direct Radiative Effects (DRE) of BrC. Aerosol DRE represents the difference of radiative budget with and without aerosols, and DRF represents the difference of DRE between present-day and pre-industrial times (Heald et al., 2014). The study by Feng et al. (2013) suggested a +0.04-0.11 W/m^2 warming effect at the top of the atmosphere due to the absorption of BrC and attributed 19% of anthropogenic aerosol absorption to BrC. X. Wang et al. (2014) estimated the global DRF of +0.11 and +0.21 W/m^2 for BrC and BC,

respectively. Jo et al. (2016) estimated a BrC DRE of +0.11 W/m^2. Lin et al. (2014) estimated a BrC DRE of +0.22-0.57 W/m^2, which accounted for 27%-70% of the BC absorption in their model. Park, Kim, Jeong, Youn, & Kim (2010) modeled BrC over East Asia and calculated a DRE of +0.05 W/m^2 at the top of the atmosphere. Brown et al. (2018) estimated a BrC DRE of +0.13±0.01 W/m^2 and 0.01± 0.04 W/m^2 from BrC aerosol-cloud interaction. Saleh et al. (2015) estimated a BrC DRE of 0.22 W/m^2 when BrC externally mixed with BC, and 0.12 W/m^2 when BrC is internally mixed with BC. All of these model estimations of BrC DRE and DRF treated BrC similar to BC, where properties were invariant with atmospheric processing or aging.

Laboratory and field studies showed a reduction of BrC absorption when exposed to light, which is usually referred to as "photo-bleaching" (Zhao et al., 2015). A recently global model simulation (X. Wang et al., 2018) included this effect, constrained with BrC absorption measurements in DC3 and SEAC4RS, resulting in a large reduction of global BrC DRE to +0.048 W/m^2 compared to previous estimates from the studies listed above. Brown et al. (2018) developed a BrC module in the CESM and showed a reduction of BrC DRE to 0.06±0.008 W/m^2 because of photo-bleaching. Other effects of atmospheric processing have not yet been in BrC global modeling. Results from the Deep Convective Clouds and Chemistry Project (DC3) found high concentrations of BrC in the continental upper tropospheric due to convective transport, suggesting more efficient atmospheric vertical transport of BrC than previously assumed (Y. Zhang et al., 2017). In this study, we developed and implemented a BrC module in the Community Earth System Model (CESM) to assess the effects of BrC DRE. Here, we include these effects and make use of the aircraft measurements of BrC absorption profiles from DC3 and SEAC4RS campaigns

to evaluate the model formulation and simulation results. The global BrC emissions from biomass burning, biofuel emissions, and secondary formation were included. We tested the sensitivity of photo-bleaching effect and the deep convective transport of BrC to its DRE, and estimated the global DRE. Model simulation results without considering the differential convective transport and BC and BrC are compared to previous studies. This is the first attempt to comprehensively analyze how convective transport and photo-bleaching affect global atmospheric heating by BrC absorption relative to BC.

2.2 Model Description

2.2.1 The CESM model

We developed the brown carbon simulation based on the Community Earth System Model (CESM) version 1.2.2 and its atmospheric component, the Community Atmosphere Model version 5 (CAM5) (Neale et al., 2010). The CAM5 model has a comprehensive mechanism for aerosols and cloud-aerosol interaction (Gettelman et al., 2010; Ghan et al., 2012; X. Liu et al., 2012). The CAM5 radiation scheme is the Rapid Radiative Transfer Method for global climate models (GCMs) (RRTMG), which provides an accurate method for radiative flux calculation (Iacono et al., 2008; Mlawer, Taubman, Brown, Iacono, & Clough, 1997). The atmospheric chemistry module, turbulence scheme, convection scheme, and cloud physics are coupled in the model (Bretherton & Park, 2009; Morrison & Gettelman, 2008; S. Park & Bretherton, 2009; Richter & Rasch, 2008; G. Zhang & McFarlane, 1995) We used a 3-mode version of the modal aerosol model (MAM3) for aerosol modeling in CAM5. The 3 modes are Aitken, accumulation, and coarse modes (Neale et al., 2010). In our BrC simulations, we used CAM5 with a spatial resolution of

1.9°x2.5°. The wet scavenging scheme of aerosols in CAM5 includes below-cloud scavenging and in-cloud scavenging, which was found to have a high bias (X. Liu et al., 2012; M. Wang et al., 2011). For the simulations used to compare with field observations, we nudged CAM5 meteorological field (temperature, humidity, wind, surface pressure, and heat) to the same meteorological year, month, and day as the observations using Goddard Earth Observing System (GEOS)-5.2.0 meteorological data products (Rienecker et al., 2008) every 6 hours in order to evaluate the model simulations with BrC observations (Chipperfield, 2006; Ma et al., 2013). We also conducted 5-year free-running model simulations using the climatology of 2010 to analyze the climate response to BrC and BC heating. The spin-up time is 3 months in the nudged CAM5 simulations and is 1 year in the free-running simulations.

2.2.2 Emission

We derived global BrC emissions from biomass burning, biofuel, and secondary formation. Same as Brown et al., 2018, we used the parameterization by Saleh et al. (2014) for biomass and biofuel burning, in which emitted BrC absorption is a function of BC/Organic Aerosols (OA) emission ratio. We included secondary aerosols from the oxidation of aromatic as the major source of secondary BrC (Hecobian et al., 2010; Lin et al., 2015; Sareen et al., 2013). Secondary BrC produced from aromatic oxidation absorbs more solar radiation in high-NOx conditions (A. Laskin, Laskin, & Nizkorodov, 2015; Lin et al., 2015; X. Liu et al., 2012; Tomoki Nakayama et al., 2010; L. Yu et al., 2014; Zhong & Jang, 2011). We did not consider the NOx dependence of secondary BrC in this study. More details will be described in Section 2.3.

The biomass burning emissions we used are from the Global Fire Emission Database version 4 including small fires (GFED4s) (Giglio, Randerson, & Werf, 2013; J. Randerson, Chen, Werf, Rogers, & Morton, 2012). It contains global burned area distribution and biomass burning emission factors of related aerosols and gas species for different fire types, with a spatial resolution of 0.25°x0.25°. In CAM5, we aggregated it to a spatial resolution to 1.9°x2.5° and used GFED daily emission and diurnal cycle factors. The different emission factors for the tropical forest, temperate forest, boreal forest, savanna, agriculture waste, and peat burning are based on Akagi et al. (2011). Fire emissions can reach high altitudes (e.g., Neale et al., 2010). We used an observation-constrained global fire plume rise dataset in which MODIS fire hotspot and fire radiance power data were used in a 1-D fire plume rise model and the resulting fire plume distribution is in good agreement with the Multi-angle Imaging SpectroRadiometer (MISR) observations (Ke, 2020). Biomass burning emissions have high uncertainties caused by burned area, emission factors, fuel loads and combustion completeness factors (Akagi et al., 2011; Giglio et al., 2013), and the complex interactions between fire, terrestrial ecosystem, and climate systems amplify these uncertainties (Zou et al., 2019).

Anthropogenic emissions are from the IPCC AR5 emission dataset (Lamarque et al., 2010), and BC and OC emissions are updated based on the emission inventory of 2000 (T. C. Bond et al., 2007; Junker & Liousse, 2008). We increased anthropogenic emissions in China by 50% according to Zhang et al. (2009). For the Arctic region (> 66°N), we used the Evaluating the Climate and Air Quality Impacts of Short-lived Pollutants (ECLIPSE) emission dataset, which includes an improvement for the Arctic BC emissions (Klimont et al., 2015; Stohl et al., 2013).

For the optical properties of BC, we used 10 and 8.1 m2/g for 345- 442 nm and 442-625 nm, respectively, as the MAE values of BC (T. C. Bond & Bergstrom, 2006; Knox et al., 2009). The MAE values are lower than the estimation by Bond et al. (2013) (11 m2/g) and Jacobson (2012) (16 m2/g including high-RH conditions), and are higher than the estimation by Schulz et al. (2006) (7.9±1.9 m2/g). MAM3 assumes that primary carbon is internally mixed with secondary aerosols in the accumulation mode.

2.3 Brown carbon module

2.3.1 BrC optical property and photo-bleaching

BrC absorption depends on its Mass Absorption Efficiency (MAE), which is the ratio of light absorption in the wavelength λ to BrC mass concentration (m^2 g^{-1}),

$$MAE_{BrC}(\lambda) = \frac{A(\lambda)}{C_{BrC}} \quad (1)$$

where $A(\lambda)$ represents the absorption of BrC at the wavelength of λ (m^{-1}), and c_{BrC} is the mass concentration of BrC (g m^{-3}).

Similar to Jo et al. (2016), we used a constant MAE value for primary BrC, 1.0 m^2/g at 550 nm (McMeeking, 2008), and we used an MAE value of 0.19 m^2/g at 550 nm for secondary BrC based on the work by Nakayama et al. (2010). There are other MAE estimates in experiments such as 3.6-4.1 m^2/g (Alexander et al., 2008) and 0.58-0.64 m^2/g (Hecobian et al., 2010), and model-specified values such as 0.35 m^2/g by X. Wang et al. (2018). MAE value may also change in different seasons (Cheng et al., 2011). At present, there are not enough observations to specify variable MAE values in the model. The MAE

value at the other wavelengths was calculated using the following function (T. C. Bond & Bergstrom, 2006),

$$\mathrm{MAE}(\lambda) = \mathrm{MAE}(\lambda_0) * (\lambda_0/\lambda)^{AAE} \quad (2)$$

where AAE is absorption Angström exponent, and λ_0 is 550 and 365 nm for primary and secondary BrC, respectively. We used AAE = 5.0 for λ < 2 μm (Jo, Park, Lee, Kim, & Zhang, 2016; T. Kirchstetter & Thatcher, 2012). BrC AAE varies depending on its source and wavelength used (T. Kirchstetter & Thatcher, 2012; J. Liu et al., 2014). Jo et al. (2016) found BrC/BC ratio decreases when the BrC AAE increases from 5 to 6.19, Saleh et al. (2014) also found BC/OA ratio is negatively related to BrC AAE and positively related to BrC absorption. Therefore, the variation of BrC AAE leads to additional uncertainty of the BrC simulation.). The imaginary part of the refractive index for BrC is estimated using the following equation (J Liu et al., 2013):

$$k_{BrC,\lambda} = k_{OA,\lambda} * \frac{c_{OA}}{c_{BrC}} = \frac{\rho\lambda \cdot A(\lambda)}{4\pi \cdot c_{BrC}} = \frac{\rho\lambda \cdot MAE(\lambda)}{4\pi} \quad (3)$$

where ρ is particle density (g m^{-3}), A(λ) is the light absorption at wavelength λ, and c is mass concentration.

The estimated k_{BrC} value is 0.045 at 550 nm for primary BrC and 0.043 at 365 nm for secondary BrC, respectively.

There is observational evidence that both primary and secondary BrC are affected by photochemical aging (or bleaching), which reduces BrC light absorption when exposed

to light (Forrister et al., 2015; Lee, Aiona, Laskin, Laskin, & Nizkorodov, 2014; Sareen et al., 2013; Wong, Nenes, & Weber, 2017; Wong et al., 2019; Zhong & Jang, 2011). Previous modeling of the BrC photo-bleaching effect by Xuan Wang et al. (2018) and Brown et al. (2018) applied a 1-day e-folding time for BrC before reaching a threshold of 25% of the original BrC absorption. Our approach to BrC photo-bleaching considers different bleaching effects depending on the BrC source. We specify a decay half-life of 12 hours when light is present for primary biomass and biofuel BrC in the daytime until 6% is left and no further photobleaching occurs (Forrister et al., 2015) due to stable high molecular weight chromophores (Di Lorenzo et al., 2017; Di Lorenzo & Young, 2016; Wong et al., 2017; Wong et al., 2019). Different components of SOA have different photo-bleaching lifetimes. Aromatic SOA has a half-life of 12-24 hours (Lee et al., 2014; Jiumeng Liu et al., 2016; Zhong & Jang, 2011), limonene SOA has a half-life of <0.5 hours (Lee et al., 2014). Methylglyoxal SOA has a half-life of 90 minutes (Zhao et al., 2015; Wong et al., 2017). Therefore, the half-life for secondary aromatic BrC is specified at 12 hours in daytime until it is completely removed (Jiumeng Liu et al., 2016). The other secondary BrCs that have shorter lifetimes contribute little to global radiative forcing and are not included in the model.

The analysis of aircraft BrC observations by Y. Zhang et al. (2017) showed that BrC transported by deep convection plays a significant role in radiative heating of the upper troposphere, and that BrC warming is about one third of BC warming at the tropopause. The standard model simulations show a large low bias of BrC in the upper troposphere compared to the observations by Y. Zhang et al. (2017). In addition, in-cloud heterogeneous BrC production is another possible reason for the high level BrC in the

upper troposphere. A fraction of biomass burning BrC from heterogeneous oxidation by ozone will stay free from photo-bleaching, and BrC from heterogeneous oxidations by OH has a long lifetime of days (Browne et al., 2019). Therefore, we conducted sensitivity simulations of BrC to investigate the effects of photo-bleaching and wet scavenging during deep convection.

One important finding by Y. Zhang et al. (2017) is that wet scavenging of BrC during convection differs from BC and OC. Therefore, BrC is simulated using a different tracer from OC in this work unlike Brown et al. (2018). The BrC property of interest is absorption and we assume that the tracer's optical property is light absorption only (no scattering). Consequently, there is no double counting of OC scattering. However, it should be noted that BrC is a class of organic aerosols that both scatter and absorb light. We analyzed in this study the effect of BrC light absorption. The model simulation of OC mass and scattering was not affected by the simulation of a BrC tracer that only absorbs light. In the following analysis, the DRE from BrC is for light absorption only such that it represents the DRE of the OC absorption and can be compared to the DRE of the BC absorption.

2.3.2 BrC emissions

We assumed that BrC is emitted in the accumulation mode (J Liu et al., 2013). Sources of the more stable forms of BrC include primary emissions of biomass burning and biofuel, as well as secondary formation from aromatic oxidation. Similar to previous model approaches (Brown et al., 2018; X. Wang et al., 2018), biomass burning BrC emissions were parameterized as a function of BC to OA ratio of the emissions (Saleh et al., 2014):

$$k_{OA,550} = 0.016 log_{10}\left(\frac{E_{BC}}{E_{OA}}\right) + 0.03925 \quad (4)$$

where $k_{OA,550}$ is OA absorptivity at 550 nm, and E_{BC} and E_{OA} are BC and OA emission rates (g m^{-2} s^{-1}), respectively. We computed $k_{OA,550}$ in order to calculate BrC emissions. In the model, the absorption of the OC tracer was specified to be 0. All OC absorption was due to the BrC tracer. We scaled BrC Emissions based on $k_{OA,550}$, MAE and OA emissions using the following equation by J Liu et al. (2013):

$$E_{BrC} = \frac{4\pi k_{OA,550} \cdot E_{OA}}{\rho \cdot 550nm \cdot MAE_{BrC}(550\ nm)} \quad (5)$$

where ρ is particle density (g m^{-3}), and E_{BrC} is BrC emission rate (g m^{-2} s^{-1}).

Using the GFED emissions inventory, we estimated an annual average global BrC source from biomass burning of 3.6 TgC/yr, ~23% of OC emissions (15.9 TgC/yr) and about twice as large as BC emissions (1.9 TgC/yr). The variability of BrC emission rate among biomes therefore depends on the BC to OA emission ratios in the GFED emission inventory. Using the same equations and an average E_{BC}/E_{OA} ratio of 0.41 (Junker & Liousse, 2008), we estimated an E_{BrC}/E_{OA} ratio of 0.38 and an annual global BrC biofuel source of 3.1 TgC/yr on the basis of biofuel emission inventory by T. C. Bond et al. (2007). The estimates of primary BrC emissions are comparable to previous studies (Table 1). BrC emissions from fossil fuel combustion are not yet well characterized to be included in a global model (Saleh et al., 2014; Xie et al., 2017).

The major fraction of secondary BrC that affects atmospheric heating is formed during the oxidation of aromatics (Jacobson, 1999; T Nakayama et al., 2013; Zhong, Jang, Oliferenko, Pillai, & Katritzky, 2012). As in previous studies (Jo et al., 2016; X. Wang et al., 2014a), we assumed that secondary BrC is from aged aromatic SOA. In the CAM5 MAM3 aerosol mechanism, the SOA mass yield for aromatics oxidation is 15% (Neale et al., 2010; Odum et al., 1997). We estimated a global secondary BrC source of 4.1 TgC/yr in agreement with previous studies.

BrC emissions used in this study and the comparison to previous studies are summarized in Table 1, and the emission distribution is shown in Figure 1. Biofuel emissions are high in China and India, and secondary BrC sources are also large in Europe and North America. Figure 2 shows the annual cycle of BrC emissions in 2010. Biofuel and secondary BrC sources have little seasonal variation in the model, while biomass burning has significant seasonal variation. The BrC source is the highest in August at 18.9 TgC/yr. Biomass burning emission accounts for more than 60% of the BrC emissions in August.

Table 1 - BrC emission sources (TgC yr^{-1}) of this and previous studies.

	This work	Jo et. al. (2016)	(X. Wang et al., 2014a)
Primary biomass burning source	3.6	3.0±1.7	8 for primary sources
Primary biofuel source	3.1	3.0±1.3	

Table 1 continued

Secondary formation	4.1	5.7	3.2

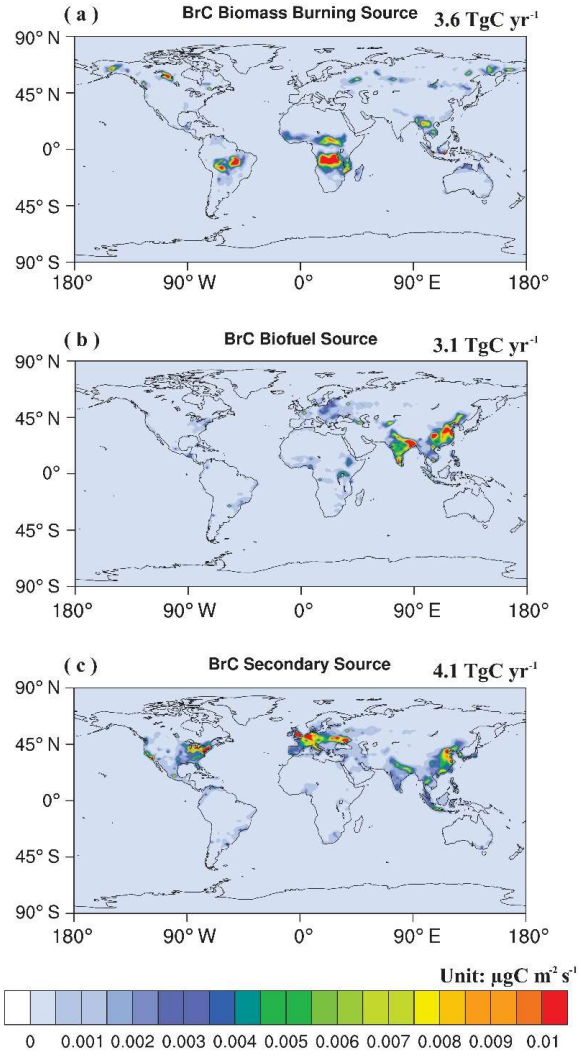

Figure 1 - Spatial distributions of global emissions of BrC from biomass burning (a), anthropogenic biofuel combustion (b) and secondary formation (c) in 2010. Unit is

μg C m^{-2} s^{-1}. The total emission is 3.6, 3.1, and 4.1 Tg C yr^{-1} for biomass burning, biofuel, and secondary formation, respectively.

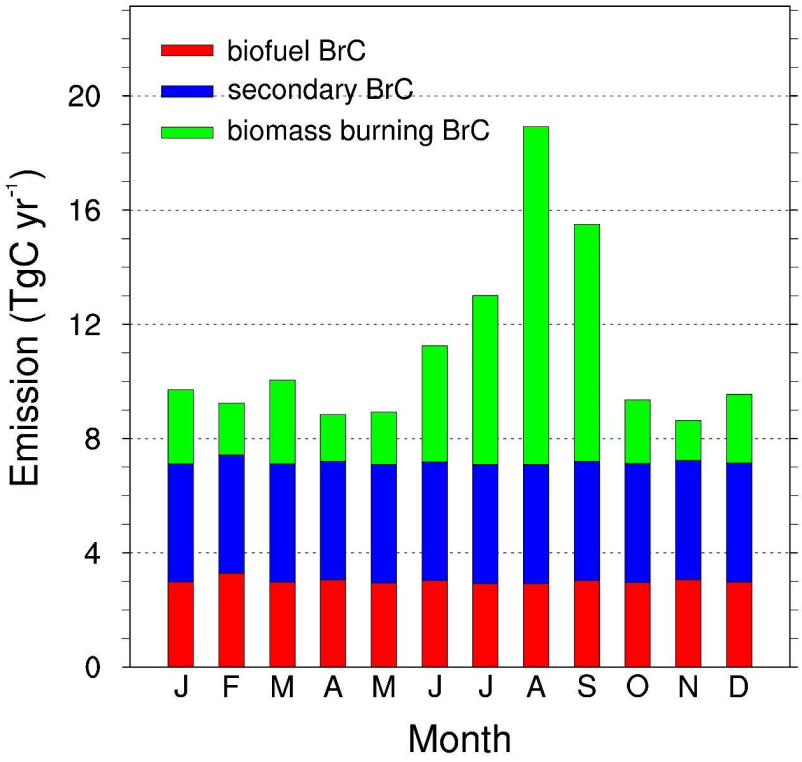

Figure 2 - Monthly mean global BrC emission rates (Tg C yr^{-1}) in 2010. Green, blue, and red bars represent the emissions from biomass burning, biofuel combustion, and secondary BrC formation, respectively.

2.4 Model evaluation

2.4.1 Black carbon measurements from HIPPO

HIAPER (High-Performance Instrumented Airborne Platform for Environmental Research) Pole-to-Pole Observations (HIPPO) measured atmospheric composition approximately from the Arctic to the Antarctic over the Pacific Ocean (Wofsy, 2011).

HIPPO executed 5 missions from January 2009 to September 2011. The flight path of each HIPPO mission is shown in Figure 3. Measurements over continental North America east of 140°W were not included in our model evaluation. BC measurements for particles with a size range of 90-600 nm were made from a single-particle soot photometer (SP2) and we increased measured BC data by a factor of 1.1 to account for larger sized BC in the model evaluation (Schwarz et al., 2010; Schwarz et al., 2013). We make use of HIPPO BC measurements to constrain convective transport and wet scavenging.

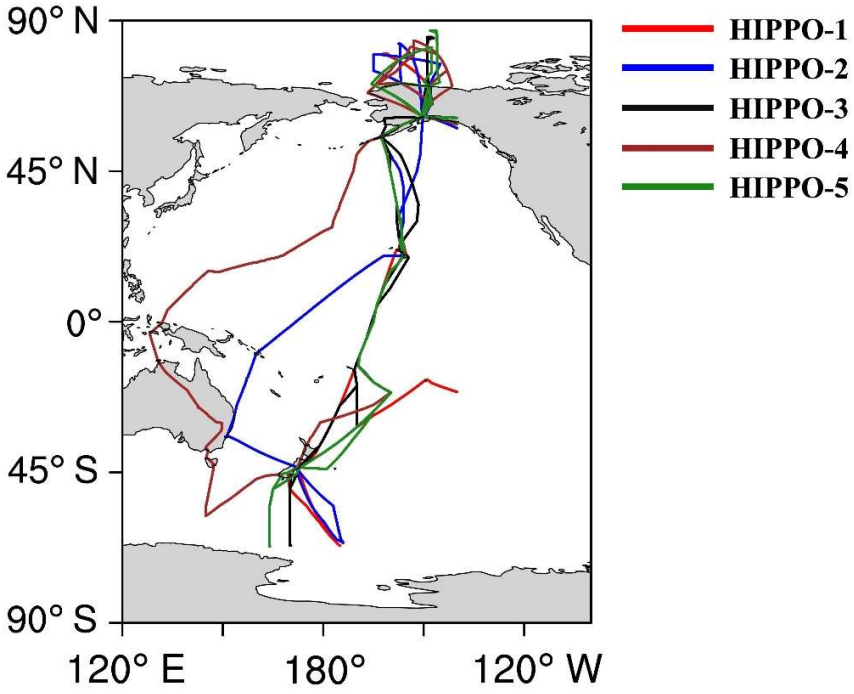

Figure 3 - Flight track of the 5 HIPPO missions. Colored lines in red, blue, black, brown, green represent flight track of HIPPO-1 to HIPPO-5 respectively. Flights over continental North America east of 140°W were not included in this study.

Wet scavenging is uncertain in 3-D global modelling of BC (Schwarz et al., 2010; Liu et al., 2011). Wang et al. (2013) tested the sensitivities of different physical

mechanisms and found a high sensitivity of BC simulations to convective transport and wet removal. Comparison of CAM5 BC simulations with HIPPO observations in Figure 4 shows large overestimates of BC in the tropics and the upper troposphere. Since the emissions of BC are from the surface, the model high biases in these regions suggest insufficient wet scavenging during convection. X. Wang et al. (2014) updated the model wet scavenging by scavenging hydrophobic aerosols in convective updrafts and scavenging hydrophilic aerosols from cold clouds. In all simulations of this study, we increased interstitial BC scavenging by a factor of 5 to increase wet scavenging and reduced stratiform liquid-containing cloud based on model evaluations using HIPPO observations. The high biases above 300 hPa at mid and high latitudes persisted particularly for HIPPO-1 in January 2009 and HIPPO-2 in November 2009. In winter, the simulated high BC concentrations were above the tropopause level at mid and high latitudes, indicating that convective transport reached too high an altitude. We therefore limited deep convection mass transport to an altitude of 50 hPa below the model estimated tropopause, after which the high biases at mid and high latitudes above 200 hPa were corrected. During HIPPO-3 in March-April 2010, model simulated free tropospheric BC at northern mid and high latitudes were much lower than the observations, suggesting excessive scavenging in the model. We reduced cloud-born BC scavenging to 10% when cloud ice is present and to 50% for the other conditions, which improved the model simulations of free tropospheric BC simulations at mid and high latitudes in HIPPO-3 (and HIPPO-2). The modification slightly worsened the model high bias at northern mid and high latitudes in the summer for HIPPO-5 in August-September 2011 and to a lesser extent for HIPPO-4 in June-July 2011. Figure 5 shows the comparison between BC vertical profiles during all HIPPO campaigns

with CAM5 simulations for 5 latitude bins (90°S-60°S, 60°S-20°S, 20°S-20°N, 20°N-60°N, 60°N-90°N), respectively. The modified CAM5 simulations agreed better with the observations in all regions, but still overestimated BC in the middle and upper troposphere over the tropics, which may lead to a low bias in the model simulated BrC/BC heating ratio in the tropics (to be discussed in Section 2.5.3).

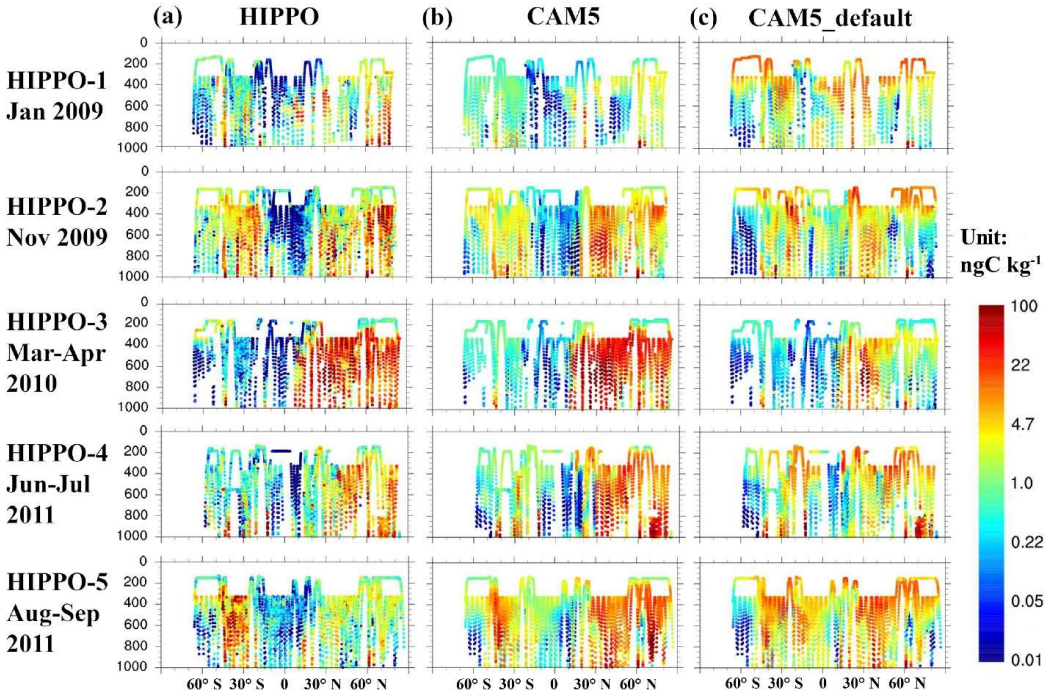

Figure 4 - Comparison of HIPPO BC (ng C kg^{-1}) measurements (a), simulated BC data from the modified CAM5 model (b) and simulated BC data from the default CAM5 model (c) during HIPPO mission 1-5. The 5 rows from top to bottom are HIPPO-1 (Jan 2009), HIPPO-2 (Nov 2009), HIPPO-3 (Mar-Apr 2010), HIPPO-4 (Jun-Jul 2011), and HIPPO-5 (Aug-Sep 2011), respectively. Measurement data

along the flight tracks of Figure 3 are 1-min averages. Model data are selected corresponding to the location and time of aircraft measurements.

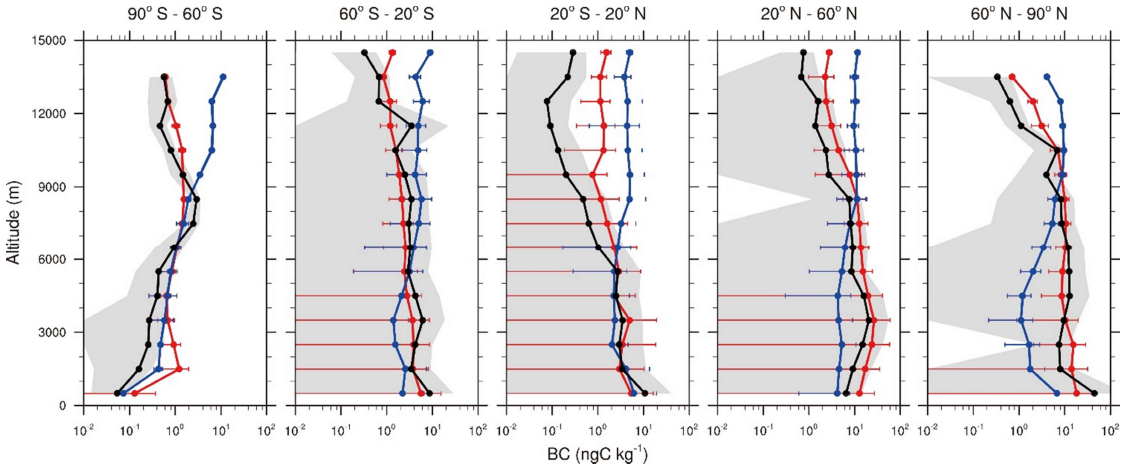

Figure 5 - Comparison of observed and simulated BC vertical profiles during HIPPO missions for the latitude bins of 90° S-60° S, 60° S-20°S, 20° S-20° N, 20° N-60°N and 60° N-90°N. Black lines and shaded areas show the means and standard deviations of the observations binned in 1-km intervals, respectively. The colored vertical lines and horizontal bars show the means and standard deviations of the default (blue) and modified CAM5 results (red), respectively.

2.4.2 Aerosol optical depth (AOD) and absorption aerosol optical depth (AAOD) over fire emission dominated regions

Direct assessments of BrC sources using observations are difficult because of limited observations. We can, however, evaluate model simulations of fire aerosols with AOD and AAOD measurements. For this purpose, we chose the months and regions in model simulations that >50% of monthly mean AOD data are from fire emissions for 2010. The distribution of model simulated mean AOD for data points selected in this manner are shown in Figure 6(a). For comparison purpose, the ground-based AOD measurements were obtained from the Aerosol Robotic Network (AERONET) version 3 level 2.0 dataset (Holben et al., 1998). To compare with model simulated AOD data at 550 nm, the AOD

measurements at 500 and 675 nm were used to compute Ångström exponent (Ångström, 1964) and calculate the corresponding AOD values at 550 nm (Kumar, Sivakumar, Reddy, Gopal, & Adesina, 2013). Figure 7(a) compares the monthly mean fire dominated 550 nm AOD observations in 2010 in AERONET with corresponding monthly mean model results for selected months and regions. The correlation coefficient, *r*, is high at 0.88. We performed principal-component (PC) regression analysis of observed and simulated data. The low regression slope (0.56) indicates that the observed AOD data were underestimated, implying a low bias in fire emissions.

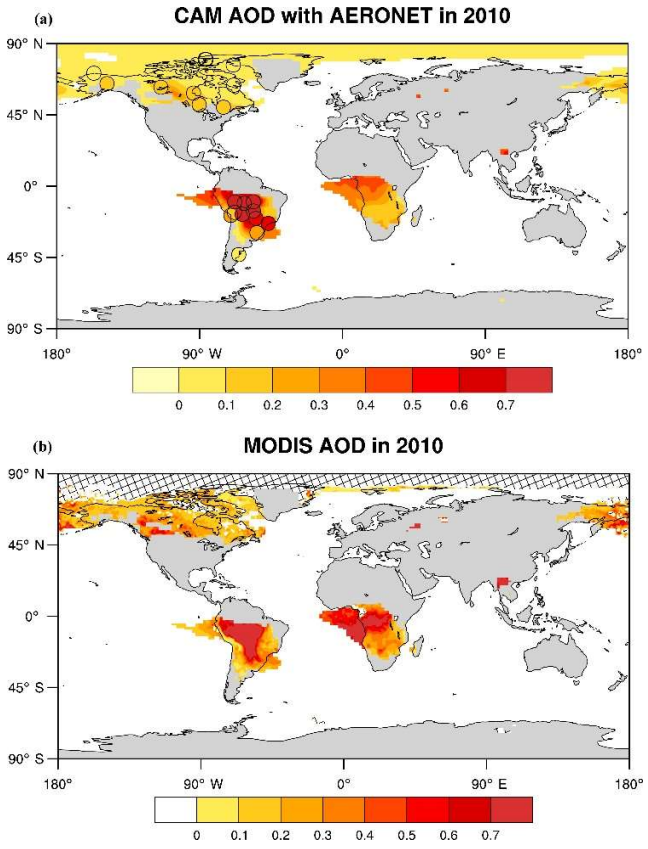

Figure 6 - Simulated (a) and MODIS observed (b) 550 nm AOD data averaged for the months and regions in which fire emissions account for < 50% of the total AOD for 2010. AERONET measurements in the corresponding months and regions are shown as color-coded open circles in (a). MODIS data in the shaded Arctic region in

(b) are not used due to the uncertainty of MODIS retrieval above bright surface (Remer, Mattoo, Levy, & Munchak, 2013).

We also compared AOD with the measurements from Moderate Resolution Imaging Spectroradiometer (MODIS) on Terra (EOS-AM-1) satellite for the months and regions in model simulations that >50% of monthly mean AOD data are from fire emissions for 2010. We used Collection 6 of MODIS level-3 Deep Blue/Dark Target merged product with a resolution of 1°x1° (Platnick et al., 2017). Figure 7(b) shows the comparison. Both the correlation coefficient r (0.67) and the PC regression slope k (0.49) are lower than the comparison with AERONET observations. One reason is that the high AOD data in the outflow region of the tropical Atlantic from fire emissions over Africa were significantly underestimated (Figure 6 (b)); similar low biases were also found in the outflow region of fire emissions in South America. Additionally, CAM5 underestimates AOD at high latitudes (X. Liu et al., 2012). The general low bias of fire aerosol emissions was also found by Ward et. al. (2012). For these data, the effect of BrC absorption on AOD is small; we estimate that BrC absorption contributes 0.37% of the total AOD.

In addition, we compared the model simulations to the AAOD data from the AERONET version 3 level 2.0 inversion dataset (Holben et al., 2006). Since the AAOD estimation is highly uncertain in the low AOD conditions (Dubovik et al., 2000), we used only AAOD measurements for AOD at 440 nm ≥ 0.4 (Holben et al., 2006). Monthly mean AAOD data were computed for AERONET sites with more than 10 days of daily averaged observed AOD at 440 nm > 0.4 in a month. Because of the model underestimation, the corresponding model threshold of AOD at 440 nm is 0.315 based on the PC regression between AERONET observations and model simulation results (Figure 7(a)). Daily model

results with AOD at 440 nm > 0.315 were used to compute simulated monthly means for the grid cells corresponding to the AERONET sites. To show the performance of the model simulation of aerosol absorption, here we compare the observed and simulated AAOD values at 550 nm, which is near the peak wavelength of solar intensity. Because of the strong wavelength dependence of BrC absorption, the enhancement of AAOD by BrC absorption at wavelengths lower than 550 nm is more significant. Figure 7(c) compares the monthly mean 2005-2014 AERONET AAOD data over fire-dominated regions and months with the corresponding monthly mean model results. The observations showed significant interannual variability, which was not included in the model results for a climatological 2010 year. With BrC absorption, the simulated higher AAOD data are in better agreement with AERONET observations with a PC regression slope of 0.59 compared to a slope of 0.43 for the simulation without BrC absorption. For these observations, the model underestimated the AERONET AAOD observations by 39% without BrC absorption. Including BrC absorption reduced the low bias to 17%, which is well within the large variability of the observations. Globally, the AAOD absorption at 550 nm is higher by 8.5% on average when BrC is considered in the model simulations.

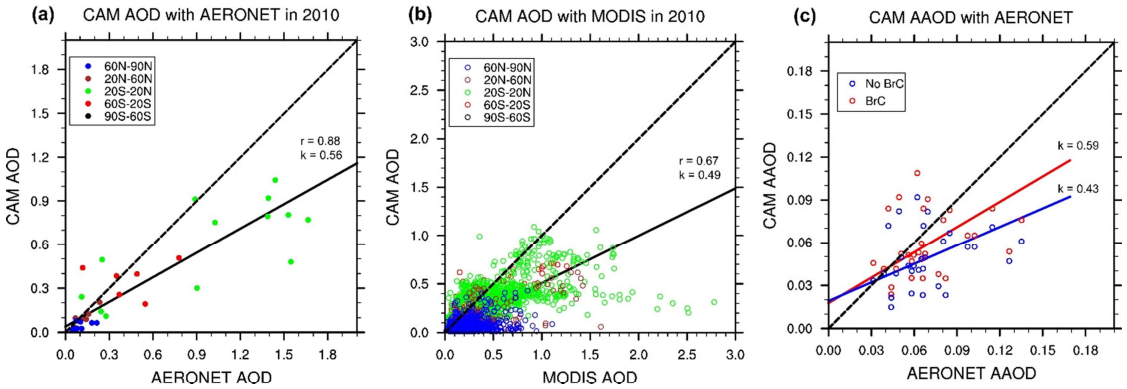

Figure 7 - Comparison of monthly mean AOD and AAOD data in 550 nm for fire dominated months and regions (Figure 6(a)) of model simulations with the observations for (a) 2010 AERONET AOD; (b) 2010 MODIS AOD and (c) 2005-2014 AERONET AAOD. For (a) and (b), model data correspond to the same time and location of the observations. The data points in (a) and (b) are color-coded as a function of latitude. The solid line denotes a PC regression line and the dashed line denotes the 1:1 reference line. For (c), monthly mean values of model data corresponding to AERONET AAOD observations are shown. The solid lines denote PC regression lines for model results with and without BrC absorption, and the corresponding regression slope (*k*) values are shown. The dashed line denotes the 1:1 reference line.

2.5 Results

2.5.1 Model simulations of BrC for DC3 and SEAC4RS missions

We evaluated BrC model simulations using the measured BrC absorption data from the airborne measurements of Studies of Emissions, Atmospheric Composition, Clouds and Climate Coupling by Regional Surveys (SEAC4RS) (Toon et al., 2016) and Deep Convective Clouds and Chemistry Project (DC3) field experiments (Barth et al., 2015). The SEAC^{4}RS campaign was conducted during August 6 to September 23, 2013 over the central and southeast U.S., and the DC3 campaign was conducted from May 18 to June 22, 2012 over a similar region. Flight tracks for these experiments were shown in Figure 8. Fresh fire plume data, diagnosed by plumes with a coefficient of determination between

CO and CH_3CN > 0.5 during the period of enhanced CO, were not included in model evaluation as in previous studies (De Gouw et al., 2004; J. Liu et al., 2014).

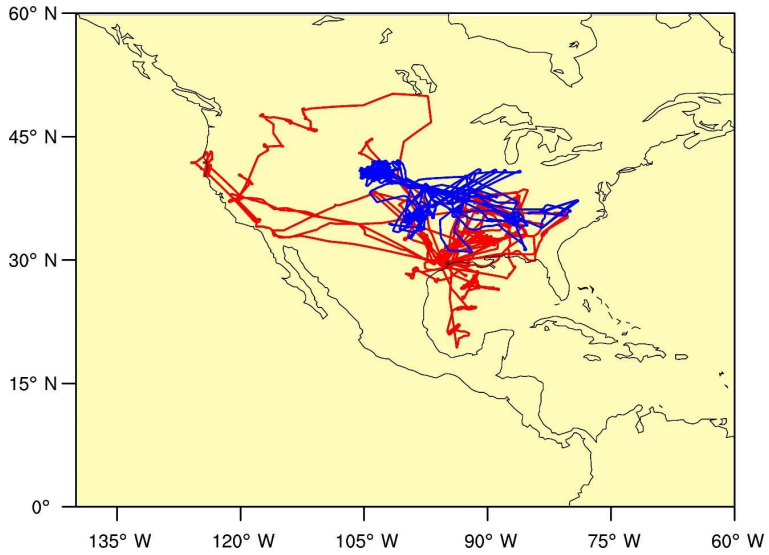

Figure 8 - Flight tracks of SEAC4RS (red) and DC3 (blue) field experiments.

We described in Section 2.3.1 the rationale for sensitivity simulations to evaluate the effects of BrC photo-bleaching and convective wet scavenging. The model sensitivity simulations are listed in Table 2. In the NCNB (base) model, neither effect was included. In the NCB model, the photo-bleaching effect is included. In the ICNB model, the wet scavenging efficiency of convective transported BrC was decreased from 75% simulated in the base model to 30%, such that ~70% of BrC was transported through convection to the free troposphere as suggested by Y. Zhang et al. (2017). In the ICB model, both photo-bleaching and reduced convective scavenging effects were included. The ICBB model is similar to ICB model, but photo-bleaching of all BrC was included; in the other models including the photo-bleaching effect, only non-convectively transported BrC was affected (Y. Zhang et al., 2017).

Table 2 - BrC sensitivity simulations

CAM run name	NCNB (base model)	ICNB	NCB	ICBB	ICB (best model)
Reduced BrC convective wet scavenging	No	Yes	No	Yes	Yes
Photo-bleaching of convective transported BrC	No	No	Yes	Yes	No
Photo-bleaching of non-convective transported BrC	No	No	Yes	Yes	Yes

Figure 9 shows the observed vertical profiles of BrC absorption, BrC to BC absorption ratio (BrC/BC ratio) and concentrations of BC and CO during the DC3 and SEAC4RS experiments in comparison to the corresponding model simulation results. The difference between BC and CO vertical profiles is negligible among the sensitivity simulations. Simulated mean BC concentrations are within the uncertainties of the measurements. The underestimation at 2-5 km during SEAC4RS likely reflects underestimated fire emissions since the coefficient of determination (R^2) is 0.6 for HCN and BC at 2-5 km and it is 0.5 for HCN and BrC, reflecting the effects of biomass burning emissions on BC and BrC. The higher CO concentrations in the model than the observations, particularly near the surface, suggests that the model overestimates surface CO emissions.

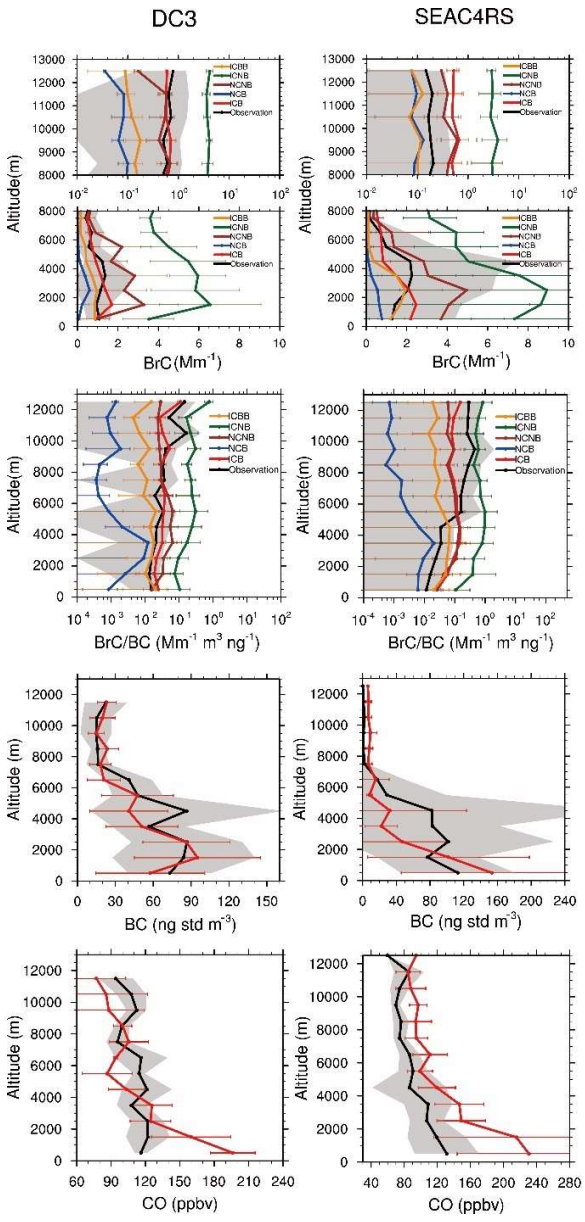

Figure 9 - Comparison between observed and simulated vertical profiles of BrC absorption at 365 nm, the ratio between BrC absorption at 365 nm and BC (BrC/BC), and concentrations of BC and CO for the DC3 (left column) and SEAC^{4}RS (right column) missions. Black lines and shaded areas show the means and standard deviations of the observations binned in 1-km intervals, respectively. The colored vertical lines and horizontal bars show the means and standard deviations of corresponding model results, respectively. Model sensitivity

simulations of BrC are listed in Table 2. The difference among simulated BC and CO vertical profiles is negligible and the ICB simulation results are shown.

Table 2 lists all sensitivity simulations. For BrC and BrC/BC simulations, Figure 9 shows that the NCNB model clearly overestimated BrC compared to the observations at 0-8 km (the overestimate is not as apparent in the BrC/BC comparison because it is a logarithmic scale). The overestimation reflected the importance of photo-bleaching (Forrister et al., 2015; Lee et al., 2014; Sareen et al., 2013; X. Wang et al., 2016; Wong et al., 2017; Wong et al., 2019; Zhong & Jang, 2011). The overestimation in the lower troposphere in NCNB led to a reasonable simulation of BrC in the upper troposphere, although the underestimation at 12 km was obvious relative to the ICB simulation during the DC3 experiment. Similarly, considering enhanced convective transport, but not photo-bleaching, the ICNB simulation clearly overestimated BrC absorption relative to the observations. Including photo-bleaching, but not enhanced convective transport of BrC, the NCB simulation clearly underestimated BrC and the BrC/BC ratio in comparison to the observations. We also included a simulation of ICBB, in which enhanced convective transport of BrC was included with photo-bleaching. Compared to the observations, upper tropospheric BrC and the BrC/BC ratio in the ICBB simulation were clearly underestimated. At 12 km, the observed BrC/BC ratio is ~10 and ~20 times higher than BrC/BC near the surface during DC-3 and SEAC4RS, respectively. This increase in the BrC/BC ratio in the upper troposphere was captured by the ICB simulation. On the basis of our current understanding of BrC processes (Forrister et al., 2015; Lee et al., 2014; Sareen et al., 2013; X. Wang et al., 2016; Wong et al., 2017; Wong et al., 2019; Y. Zhang

et al., 2017; Zhong & Jang, 2011) and the model evaluation with the observations, we chose the ICB simulation to investigate the effects of global BrC radiative forcing.

During the SEAC^{4}RS experiment, Figure 9 shows that the models overestimated both BC and BrC in the upper troposphere (except ICBB and NCB, which underestimated BrC in both experiments), and all model simulations except ICNB was underestimated the BrC/BC ratio in the upper troposphere and all model simulations except NCB was overestimated the BrC/BC ratio in the middle-lower troposphere. The simulation bias is mostly due to biases in BC simulation in that BC was overestimated in the upper troposphere and underestimated in the middle-lower troposphere (Figure 9).

In the ICB simulation, wet scavenging of BrC was reduced relative to BC in order to simulate the observed BrC/BC ratios in DC3 and SEAC^{4}RS. The mechanisms are not yet clear due to a lack of laboratory and field observations. Hydrophobic OC, such as humic-like substances (HULIS), is more likely to have high light-absorption compared to hydrophilic OC (Hoffer et al., 2006). BrC with high molecular weight dominates the aged biomass burning plume (Wong et al., 2017; Wong et al., 2019). Since higher molecular weight compounds have lower hygroscopicity (Dinar et al., 2007), and it is harder to activate hydrophobic OC in cloud, less BrC is removed in deep convection. Another possible mechanism is production of BrC through in-cloud heterogeneous processing of fire plumes (Y. Zhang et al., 2017). However, there is no observation data to implement such a mechanism in a model.

2.5.2 Simulated global zonal mean distribution of BrC

We performed diagnostic model simulations to investigate the contributions of BrC absorption from biomass burning emissions, biofuel emissions, and secondary formation, respectively. Figure 10 shows the results. Secondary BrC production has a relatively small contribution because of photo-bleaching of secondary BrC is 100%, while a small fraction of BrC is left after photo-bleaching of biomass burning and biofuel BrC (Forrister et al., 2015). Both biofuel and secondary production are largest at northern mid latitudes since they are due to anthropogenic emissions.

Biomass burning BrC shows drastically different distributions from biofuel BrC. The latitudinal maximum is in the tropics and subtropics, with a secondary peak at 60°N due to fires over Canada and Siberia. The vertical extent of biomass burning BrC is much higher than biofuel BrC due to fire plume rise (Ke, 2020) and the higher vertical extent of tropical convection than midlatitudes. While the effect of biofuel BrC is primarily in the lower troposphere, the radiative forcing of biomass burning BrC is much more substantial in the free troposphere and therefore more strongly affects the atmosphere since solar heating of the atmosphere is generally weak.

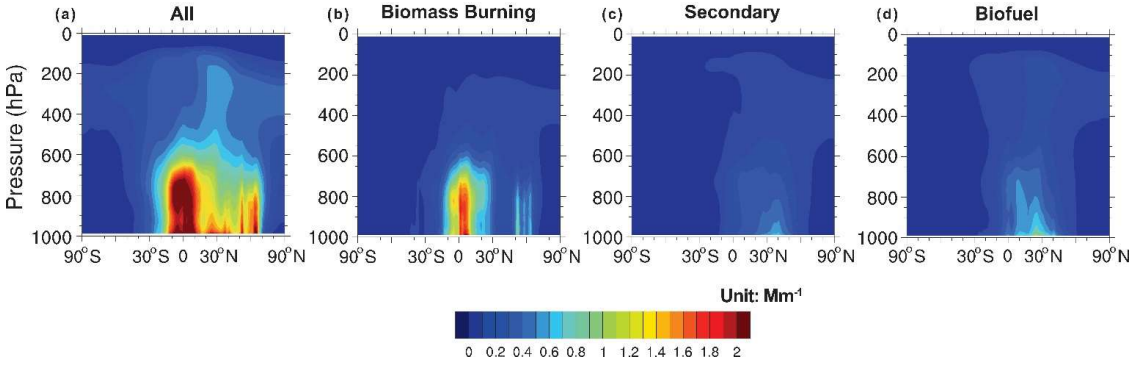

Figure 10 - Simulated zonal averaged annual mean BrC absorption at 365 nm (Mm^{-1}) for (a) all sources, (b) biomass burning emissions, (c) secondary BrC formation, and (d) biofuel BrC emissions. Unit is Mm^{-1}. Color bar is in log scale.

2.5.3 Global directive radiative effect of BrC

Aerosol DRE represents the instantaneous radiative effect of aerosols, which is sometimes confused with DRF (Ghan, 2013; Heald et al., 2014). We applied the Rapid Radiative Transfer Method for GCMs (RRTMG) to BrC and BC radiative forcing. We parameterized the imaginary part of BrC refractive index as an external input of RRTMG. As discussed in Section 2.3.2, the imaginary refractive index is specified at 0.045 at 550 nm and 0.043 at 365 nm for primary and secondary BrC, respectively. The wavelength boundaries for RRTMG shortwave and longwave are listed in Table 3 and Table 4 (Iacono et al., 2008; Mlawer et al., 1997; Neale et al., 2010). We calculated the imaginary refractive index at a different wavelength by introducing wavelength dependence w (Saleh et al., 2014):

$$w = AAE - 1 \tag{6}$$

$$k_{BrC,\lambda} = k_{BrC,550} \times (\frac{550}{\lambda})^{w} \tag{7}$$

where $k_{BrC,\lambda}$ denotes the imaginary refractive index of BrC, and w is the wavelength dependent AAE value. Calculation and parameterization of MAE and the imaginary refraction index of BrC were discussed in Section 2.3.1.

Table 3 - RRTMG wavelength boundaries for shortwave

Band Index	Lower boundary Wavelength (nm)	Upper Boundary Wavelength (nm)
1	3077	3846
2	2500	3077
3	2150	2500
4	1942	2150
5	1626	1942
6	1299	1626
7	1242	1299
8	778	1242

Table 3 continued

9	625	778
10	442	625
11	345	442
12	263	345
13	200	263

Table 4 - RRTMG wavelength boundaries for longwave

Band Index	Lower boundary Wavelength (μm)	Upper Boundary Wavelength (μm)
1	28.57	1000
2	20	28.57
3	15.87	20
4	14.29	15.87

Table 4 continued

5	12.2	14.29
6	10.2	12.2
7	9.26	10.2
8	8.47	9.26
9	7.19	8.47
10	6.76	7.19
11	5.56	6.76
12	4.81	5.56
13	4.44	4.81
14	4.2	4.44
15	3.85	4.2
16	3.08	3.85

In our estimation of BrC DRE, we only considered the absorption of BrC, and the effect of scattering is not considered. We computed the clear sky net solar flux at the top of atmosphere in two simulation, one with BrC tracer absorbing light and the other without. The difference between the two simulations is BrC DRE. The same method was used to calculate BC DRE.

The ICB model calculated global DRE distributions of BrC and BC and the DRE ratio of BrC to BC are shown in Figure 11. For 2010, we estimated the global averaged DRE of BrC absorption at 0.10 W/m^2 in comparison to 0.39 W/m^2 by BC. While the global DRE by BrC is less than BC, regional BrC DRE can be as large as that of BC due to the large difference in emission distributions. BC DRE is large at northern mid latitudes due to anthropogenic emissions from China and India. BrC emissions are relatively low in these regions (Figure 1) and consequently BC DRE dominates. Over regions with large fire emissions, both BC and BrC are important. Over most regions of the remote tropical ocean, BrC DRE is larger than BC, despite a model high bias of simulated BC in the middle and upper tropical troposphere (Figure 5), suggesting significant broad regional effects by BrC radiative forcing in the tropics. This simulated feature is due to two factors. In the ICB simulation, wet scavenging removes much more BC than BrC. Therefore, BrC is enriched relative to BC in the free troposphere (e.g., Y. Zhang et. al., 2017). In the tropics, the easterly trade wind in the boundary layer become westerlies in the middle and upper troposphere. The regions of boundary layer BC transport and free tropospheric BrC transport are in opposite directions. As a result, the DRE ratio of BrC to BC is low to the east of the fire emission regions and it is high to the west of the fire emission regions.

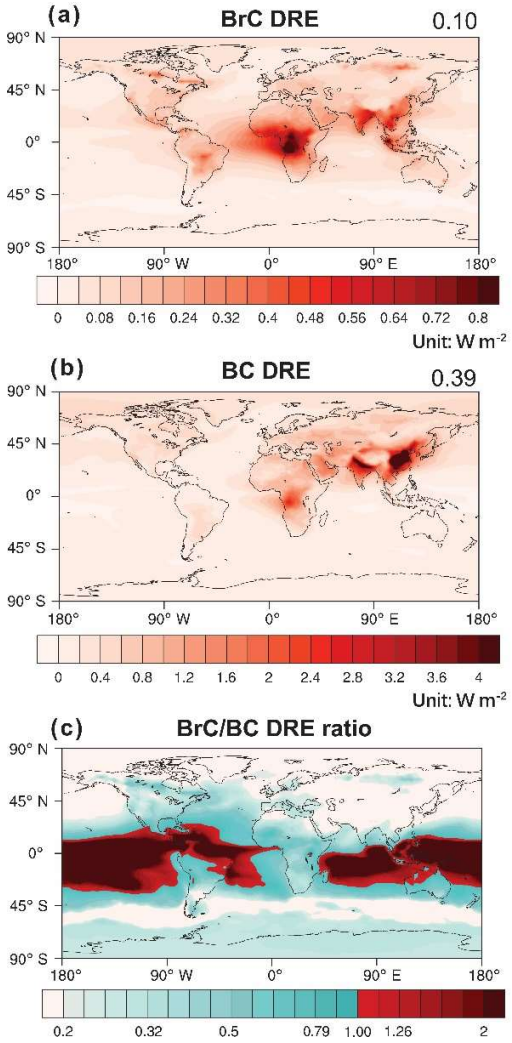

Figure 11 - Annual averaged global distributions of (a) BC DRE, (b) BrC DRE, and (c) ratio of BrC/BC DRE for 2010. The unit is W m^{-2}. The global averaged DRE is shown in the upper right corner. In (c), BrC/BC DRE ratios larger than 1.0 are specified by a different color bar.

To discuss our simulation results in the context of previous modeling studies, which did not use the ICB assumptions, we show the annual mean DRE distributions for all model simulations (Table 2) in Figure 12. Comparing the global mean DRE relative change of ICB (0.10 W/m^2) to NCB (0.013 W/m^2) with that of NCNB (0.077 W/m^2) to NCB shows that the global effect of convective scavenging efficiency decrease is larger than photo-

bleaching. A similar conclusion can be obtained by comparing the global mean DRE relative change ICNB (0.26 W/m^2) to NCNB with that of ICNB to ICB. The DRE relative change from ICB to ICBB (0.030 W/m^2) indicates the photo-bleaching effect of convectively transported BrC is larger than the enhancement of BrC convective transport. The 0.013 W/m^2 DRE in the NCB simulation is lower than previous model studies considering the photo-bleaching effect (Brown et al., 2018; X. Wang et al., 2018). In the NCB simulation, remote BrC concentrations are mostly affected by the threshold for photo-bleaching, which is 6% in this study (Forrister et al., 2015) in comparison to 25% in Xuan Wang et al. (2018) and Brown et al. (2018), causing the difference in the global DRE estimates with photo-bleaching between this work and previous studies. The 0.077 W/m^2 DRE in the NCNB simulation is comparable to previous studies (Feng et al., 2013; Jo et al., 2016; X. Wang et al., 2014b).

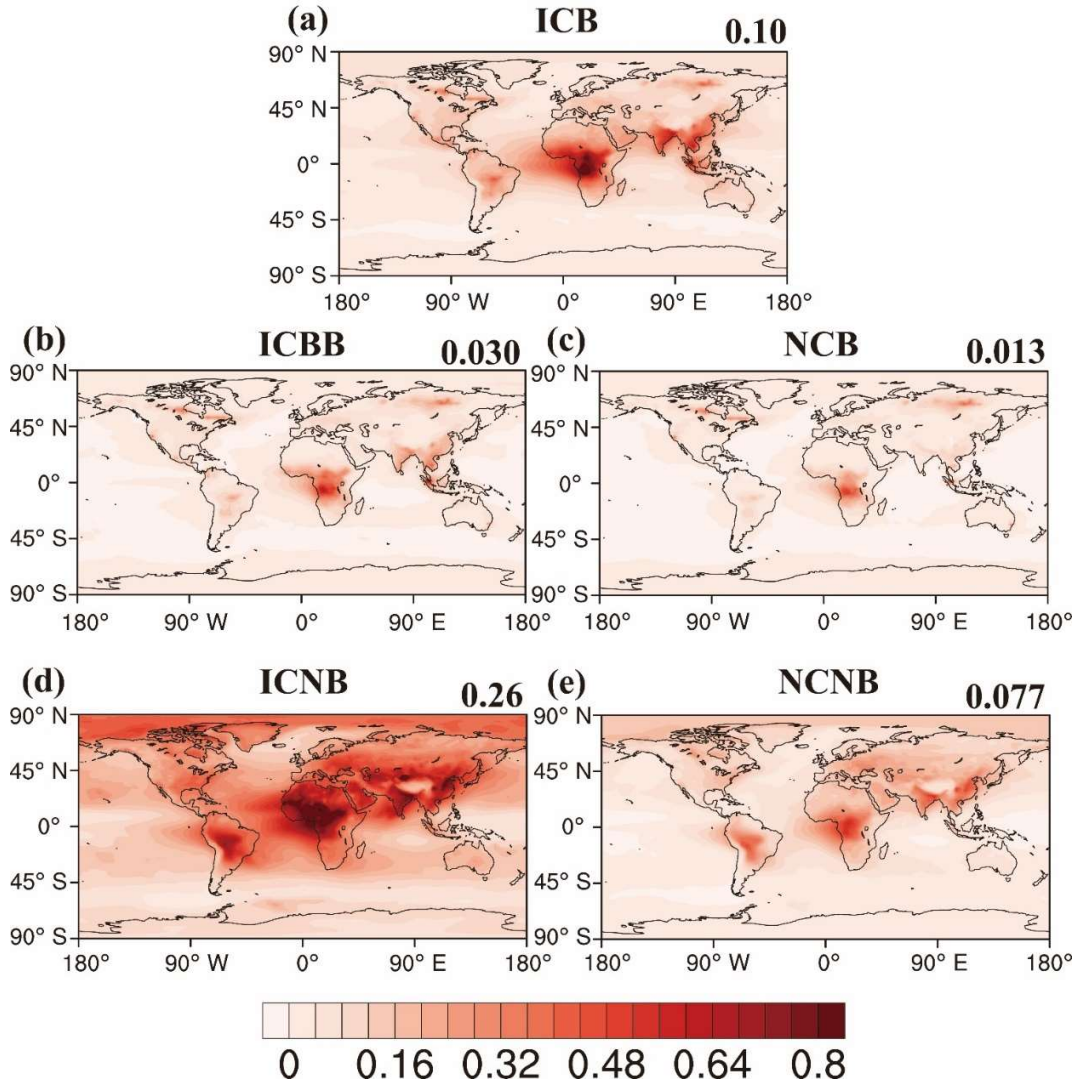

Figure 12 - Annual averaged global distributions of BrC DRE for all sensitivity simulations (Table 2). The unit is W m^{-2}. The global averaged DRE is shown in the upper right corner.

Only ICB simulation results are discussed hereafter. Figure 13 shows the seasonally BrC DRE distributions. The seasonal variation is due primarily to biomass burning. Figure 2 shows that the largest fire emissions in August, September, July, and June. While fire emissions are mostly in the tropics in SON, burning at northern mid and high latitudes much more pronounced in JJA in addition to tropical burning.

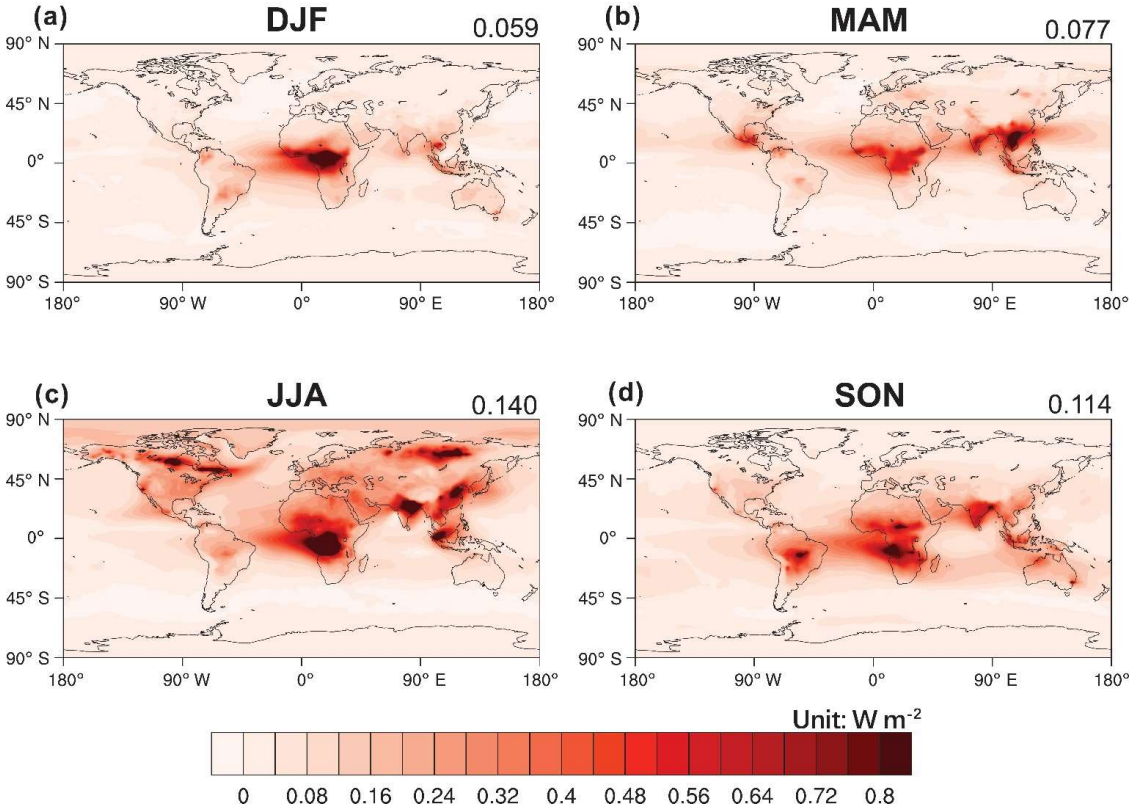

Figure 13 - Same as Figure 11 but for seasonal global DRE distributions of BrC for (a) DJF, (b) MAM, (c) JJA, (d) SON in the ICB simulation.

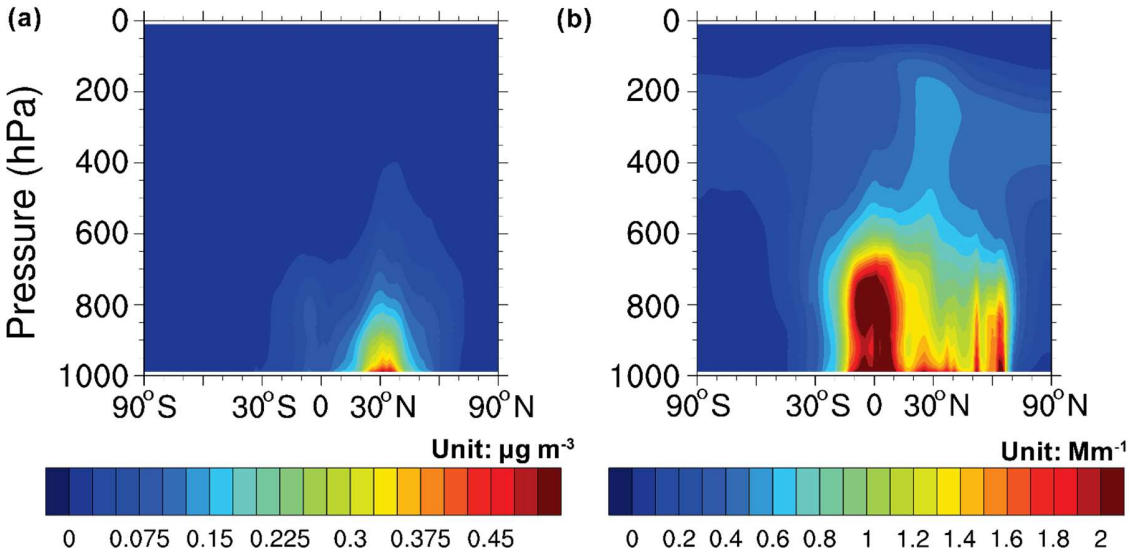

Figure 14 - Global zonal mean distributions of (a) BC mass concentrations (μg std m^{-3}) and (b) BrC absorption at 365 nm (Mm^{-1}) for 2010.

2.5.4 Global effects of BrC absorption on the atmosphere

As found by Y. Zhang et al. (2017), the importance of radiative heating by BrC relative to BC increases with altitude due to convective transport. We compared the difference of average vertical profiles of BrC to BC heating rate ratio in Figure 15. Over regions directly affected by convection, where the convective mass flux is $>10^{-5}$ kg/m^2/s, the simulated result is in agreement with Y. Zhang et al. (2017). Globally, the average BrC/BC heating rate ratio is 15% below 500 hPa and is 44% above 500 hPa. In deep convection regions, the average BrC/BC heating rate ratio is 60% below 500 hPa and 118% above 500 hPa, indicating in deep convection regions, atmospheric heating of BrC is stronger than that of BC. In comparison, over the regions not directly affected by deep convection, the globally averaged BrC/BC heating rate ratio increases from 9% at surface level to 53% in the upper troposphere. Geographically, Figure 16 shows that the difference between BrC and BC is particularly large over the tropics.

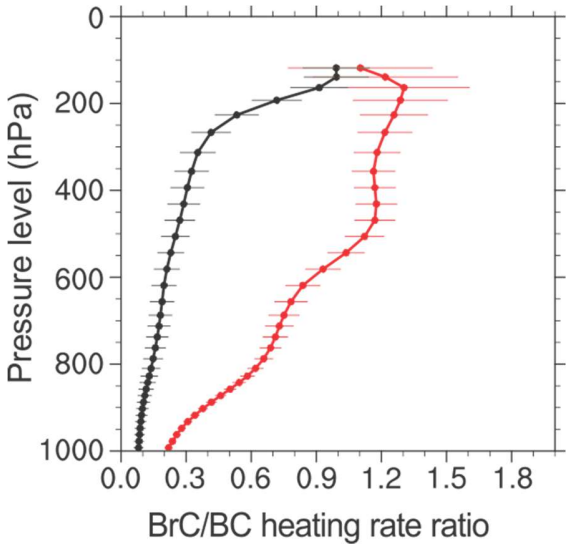

Figure 15 - Global averaged vertical profile of BrC to BC heating rate ratio for 2010. The black and red lines are the average profiles for regions without and with

deep convection events, respectively. Standard deviations are indicated by the horizontal bars.

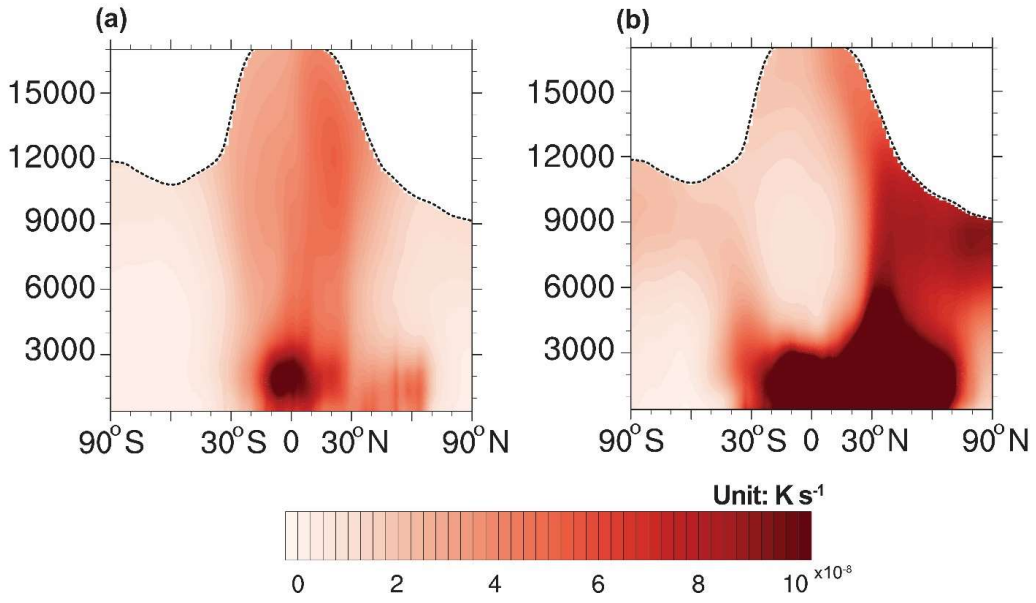

Figure 16 - Global zonal mean distributions of heating rate of (a) BrC and (b) BC for 5 years of present-day simulations. The dash line denotes the tropopause.

The heating rate from aerosols, especially its vertical profile, has significant implications on cloud dynamics (e.g., Bond et al., 2013), and can also induce feedback from regional circulation and the planetary boundary layer dynamics (e.g., Ramanathan and Carmichael, 2008). We conducted three 5-year free-running model simulations for the present day (the year 2010). In the control simulation, both BrC and BC heat were included. We then conducted sensitivity simulations in which only BrC or BC heating was included. By comparing the sensitivity simulation results to the control simulation, we diagnosed the climate response to differential BrC and BC heating.

The latitudinal and vertical difference between BrC and BC heating (Figure 15 and Figure 16) implies that BrC heating is more dominant in the tropics and tends to decrease

the vertical gradient of temperature. Allen, Sherwood, Norris, and Zender (2012) suggested that light-absorbing aerosols may contribute to tropical expansion. They did not consider the effect of BrC, the atmospheric heating effect of which is more concentrated in the tropics than BC heating (Figure 16). Using the latitude where the Mean Meridional Circulation (MMC) at 500 hPa becomes zero on the poleward side of the subtropical maximum to diagnose the boundary of the tropics (Y. Zhou, Xu, Sud, & Betts, 2011), we estimated a 1.0° ± 0.9° latitude of tropical expansion due to BrC heating in comparison to a 1.2° ± 2.9° expansion due to BC heating. The large uncertainty comes from 5 years of free-running simulations and the relatively low model spatial resolution. Another effect from BrC heating is the decrease of deep convective mass flux over the upper troposphere (Feingold, Jiang, & Harrington, 2005; Yoshimori & Broccoli, 2008). We estimated a decrease of deep convective mass flux by 4.41×10^{-5} kg/m^2/s or 4.1% over the tropics, which is about one-third of the corresponding BC heating effect (1.52×10^{-4} kg/m^2/s or 12.9%).

(Hodnebrog, Myhre, Forster, Sillmann, & Samset, 2016) suggested that biomass burning aerosols suppress precipitation regionally due primarily to aerosol-cloud interactions. On a global basis, BrC heating reduces precipitation by 0.9% ± 7.0%, which is about 60% of the precipitation reduction by BC simulated in the model. Over the tropical region with high-intensity convection and precipitation, BrC heating decreased precipitation by 3.9% ± 17.8%, similarly to that from BC heating (4.0% ± 17.1%). The effect of BrC heating on tropical precipitation (~100%) is larger than on convective mass flux (~1/3) relative to BC heating because of the stronger BrC than BC heating in the upper than lower troposphere (Figure 15 and Figure 16). BrC heating decreased precipitation by

0.3% ± 10.7% in the northern mid and high latitudes, which is much lower than the effect of BC heating (-4.8 ± 13.5%).

2.6 Conclusions

Light-absorbing aerosols, including BC and BrC, have significant impacts on the global radiative balance. Observational evidence emerged from the DC3 mission of large enhancements of BrC relative to BC over biomass burning regions (Y. Zhang et al., 2017). We developed a module for simulating the effects of brown carbon light absorption in CESM CAM5 and conducted two sets of model experiments, 2010 with nudged meteorological fields and 5-year free-running simulations. Compared to previous studies which did not consider differential convective transport of BrC and BC, the simulated BrC DREs without (NCNB) and with (NCB) photo-bleaching are comparable to previous studies (Brown et al., 2018; Feng et al., 2013; Jo et al., 2016; X. Wang et al., 2018). However, evaluations with DC3, SEAC^{4}RS, and HIPPO observations suggested that the model could simulate the observed concentrations of BrC and BC, although model biases were also found. Reducing the convective scavenging efficiency and including photo-bleaching were necessary to simulate the observed BrC distributions. Globally, the former effect is larger than the latter on simulated BrC absorption. Since the two factors have opposite effects on simulated BrC DRE, our best estimation of global DRE of BrC is 0.10 W/m^2.

The BrC DRE is estimated to be 25% of that of BC. Since biomass burning emissions tend to occur during the warm seasons when solar insolation is strong and these emissions tend to occur in the tropics when convective transport is active, the proportional

contribution to BrC DRE by biomass burning emission is larger than its fraction in the total emissions. For example, biofuel BrC emissions are seasonal and occur in mid and high latitudes, the combination of BrC absorption and solar radiation of biofuel BrC is less than biomass burning BrC for a unit of BrC emission. Relative to BC DRE, BrC DRE tends to be larger in the tropics due to different emission distributions and larger BrC levels in the upper troposphere. BrC heating reduces global precipitation by 0.9%, about 60% of the BC induced precipitation decrease. Over the tropics, the reduction of precipitation due to BrC heating is similar to BC heating, but its effect on reducing tropical convective mass flux is only ~1/3 of BC heating because BrC heating is strongly skewed to high altitudes compared to BC heating. Consequently, the effect of BrC heating on tropical expansion is comparable to BC heating.

There are still considerable uncertainties in modeling BrC absorption and its effects in the atmosphere. Parameterizations of emissions, photo-bleaching, and convective transport of BrC all require more field and laboratory observations. The uncertainty of model simulated BC also affects the comparison between the DRE and heating of BC and BrC. For example, the model overestimates of BC in the middle and upper tropical troposphere (Figure 5) may lead to an underestimate of the BrC to BC DRE ratio over the remote tropics. The modeling result of stronger atmospheric heating by BrC than BC over the tropical free troposphere in this study are also subject to these uncertainties. Field measurements over tropical convective regions during periods of biomass burning are critically needed to further improve our understanding of BrC processes and its climate effects. Continuous model development by coupling BrC related processes and climate effects into an interactive climate-fire-ecosystem model (Zou et al., 2019) in CESM would

also benefit future projections of climate radiative forcing given large impacts of fire emitted BrC in the tropics found by this study.

CHAPTER 3. INCREASED AFRICAN WILDFIRES DUE TO THE INTERACTIONS BETWEEN FIRE AND CLIMATE

3.1 Introduction

Biomass burning, or fire, is provoked by natural factors or humans and have a profound impact on ecosystems (W. J. Bond et al., 2005), carbon cycles (Ciais et al., 2014), climate change (Bowman et al., 2009) and human society (Moritz et al., 2014). Although the increase of population and land-use conversion leads to a suppression of fire (Andela et al., 2017; Arora & Melton, 2018), biomass burning in the global warming scenario is predicted to increase in the future (Kloster et al., 2012). Global warming can increase the future annual mean burned area in the western United States by 54% (Spracklen et al., 2009) indicating that the climate effects on fire will be stronger in the future (Pechony & Shindell, 2010).

The interaction between wildfire aerosols and climate change is established in a variety of ways (Y. Liu, Goodrick, & Heilman, 2014). The fire impacts climate by reducing local precipitations (De Sales, Okin, Xue, & Dintwe, 2019; Hodnebrog et al., 2016) and affecting global radiative balance through the emission of greenhouse gases (GHG) and aerosols (Bowman et al., 2009; Jiang et al., 2016). On the other hand, drought-related fire increase has been found especially in Amazon (Anderson et al., 2015; Aragão et al., 2018; Gatti et al., 2014; Y. Yang et al., 2018). Climate change increases the emergence of fire weather over the past 40 years (Jolly et al., 2015) and potentially continue to grow in the future (Abatzoglou, Williams, & Barbero, 2019). Fuel aridity shows a strong positive

antecedent correlation to burning one or two years later, indicating a potential interannual interaction between fire and climate (Abatzoglou, Williams, Boschetti, Zubkova, & Kolden, 2018).

Biomass burning is one major source of aerosols (Dentener et al., 2006). The atmospheric aerosol is a potential medium in fire-climate interactions because of its role in the global radiative balance (Ciais et al., 2014) and cloud processing (Andreae & Rosenfeld, 2008). Previous studies (Tosca et al., 2015) hypothesized a positive feedback loop between fire, cloud, and precipitation. Atmospheric model studies have focused on the perturbation from fire emission to the regional weather and global climate, but not considering the feedback from the climate back to fire (Ward et al., 2012); most fire models consider only the impact and mechanism from weather to fire (Hantson et al., 2016). The understanding of this feedback loop, thus how the climate response to fire aerosols impact burning, is important but limited.

Africa is a major biomass burning region containing clear fire regions both to the north and south of the equator. It is vulnerable to climate change (Niang et al., 2014). Observations have found a reduction of African precipitation since the 1950s (Greve et al., 2014). Central Africa has experienced a decrease in heavy precipitation extremes and an increase in warm extremes (Aguilar et al., 2009). Therefore, we expand our analysis of climate-fire interaction over Africa because of its sensitivity to both climate and fire.

Here we use the REgion-Specific ecosystem feedback Fire (RESFire) model in the Community Earth System Model (CESM) (Zou et al., 2019) to simulate wildfire constrained by fire weather variables (surface temperature, precipitation, and soil moisture)

and to estimate the atmosphere response to fire impact. We conduct 10-year RESFire run with fully coupled fire-climate interaction (the “BB aerosol feedback” case), and 10-year RESFire control run with no fire aerosol feedback (the “No BB aerosol feedback” case), in which only non-biomass burning aerosol emissions affect the atmospheric state in the model. All the RESFire simulations are conducted based on the climatology of 2000. In this study, we take the difference of burned fraction (BF) between the “BB aerosol feedback” case and the “No BB aerosol feedback” case to represent the feedback from the biomass burning aerosol (BB aerosol) and explore the mechanism and impact of this feedback.

3.2 Model Description

The RESFire model (Zou et al., 2019) is a model developed in CESM 1.2.2. It improves the default Community Land Model version 4.5 (Ward et al., 2012) (CLM4.5) by constraining fire ignition and spread, enhancing parameterization of fire impacts including online fire emissions and fire-induced land cover changes, and correcting modeling bias for online fire weather simulation. The RESFire model offers the ability to reproduce the observed burning patterns and trends, to comprehend climate procedures linked to fire, and to estimate atmospheric responses to fire emissions.

We run a 10-year ensemble of RESFire model with the climatology of 2000, with 1-year spin-up. The model spatial resolution of 0.9°x1.25° and the timestep is 30 minutes. In this research, the two-way CLM4.5 was driven by the atmospheric condition simulated in CAM5 (Neale et al., 2010).

3.3 Results

3.3.1 The impact of fire aerosol feedback on the temporal burning fluctuation

We used the periodogram with a rectangular window function to estimate the spectral density of the time series of the BF. The spectral density describes the distribution of the total amplitude of burning into different frequency or period components. Figure 17 shows the periodogram power spectral density (PSD) of monthly mean BF after detrending within 10 years for model results with and without fire aerosol feedback in the Central Africa region (10° S - 10° N, 10° E - 28° E). Aerosol feedback enhanced seasonal and annual fluctuation in periods of 3, 4, 6 and 12 months by 160% on average. Furthermore, for the PSD with interannual periods (1 year to 5 years), the BB aerosol feedback case has an overall PSD that is 7 times larger than the case without BB aerosol feedback. This implies a stronger interannual fluctuation coming from the BB aerosol feedback. The stronger seasonal fluctuation in the BB aerosol feedback case indicates the strong impact of fire from one season to the following seasons, and the stronger interannual fluctuation shows a potentially long-term effect on African burning from fire aerosol. Because of the limit of model running years, the potential interannual effect may have bias in the periodogram.

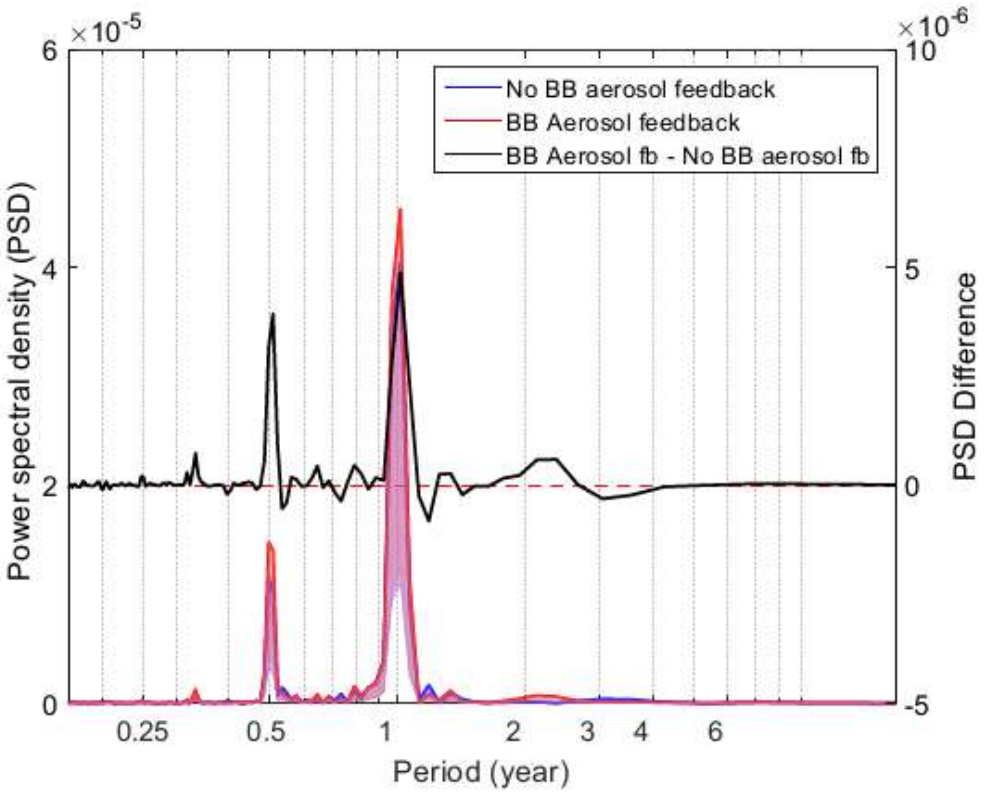

Figure 17 - A periodogram for burned fraction showing frequency spectra of biomass burning with (shown in red) and without (shown in blue) fire aerosol feedback over Africa. The difference between the burned area spectrum is shown in black. The color shaded area is the lower interval of 95% confidence level of the PSD.

3.3.2 The mechanism of fire aerosol feedback

In Figure 18, we show the changes of BF, precipitation and aerosol optical depth (AOD) from BB aerosol feedback in the two strongest fire seasons. In northern tropical Africa, the strongest fire occurs in December, January and February (DJF); in southern Africa, fire is prevailing in June, July and August (JJA). Figure 18(a) and (b) show the seasonal averaged BF in the BB aerosol feedback case and the BF change from the BB aerosol feedback. Overall, in both DJF and JJA, fire aerosol enhanced local burning and produced more aerosol. Nevertheless, the enhancement of burning is not evenly spread

over the fire region. In DJF, the increase of BF is more significant in the south of the fire region, close to the equator (2° N - 8° N, 15° E - 30° E). In JJA, the increase of BF occurs mainly in the northeast of the fire region (15° S - 5° N, 30° E - 40° E). Over the other part of the fire region, the BB aerosol feedback is relatively weak.

We explore the mechanism of this positive feedback by analyzing the corresponding change in the atmosphere. Figure 18(c) and (d) show the precipitation and aerosol optical depth (AOD) change between the cases with and without BB aerosol feedback, which represents the impact from the BB aerosol to the atmosphere. AOD distribution represents a vertically integrated condition of aerosols induced by fire aerosol feedback, and precipitation is closely related to the fire occurrence. The agreement between the distribution of AOD and precipitation changes indicating the potential correspondence between precipitation reduction and fire aerosol increase, which is also addressed in previous studies(Hodnebrog et al., 2016). On the other hand, since fire occurs mostly in dry regions and seasons, and the precipitation change is more significant in wet regions and seasons, the location of significant precipitation change is staggered with where the BF is high. The precipitation changes (Figure 18 (c)) and the BF distribution (Figure 18 (a)) overlap only in some regions that are both in the fire season and is sensitive to precipitation reduction. These regions, mainly located on the edges of fire regions, have strong BB aerosol feedback. In this case, the fire aerosol impact plays a role to expand or shift the fire region to places that have significant precipitation reduction caused by fire aerosols.

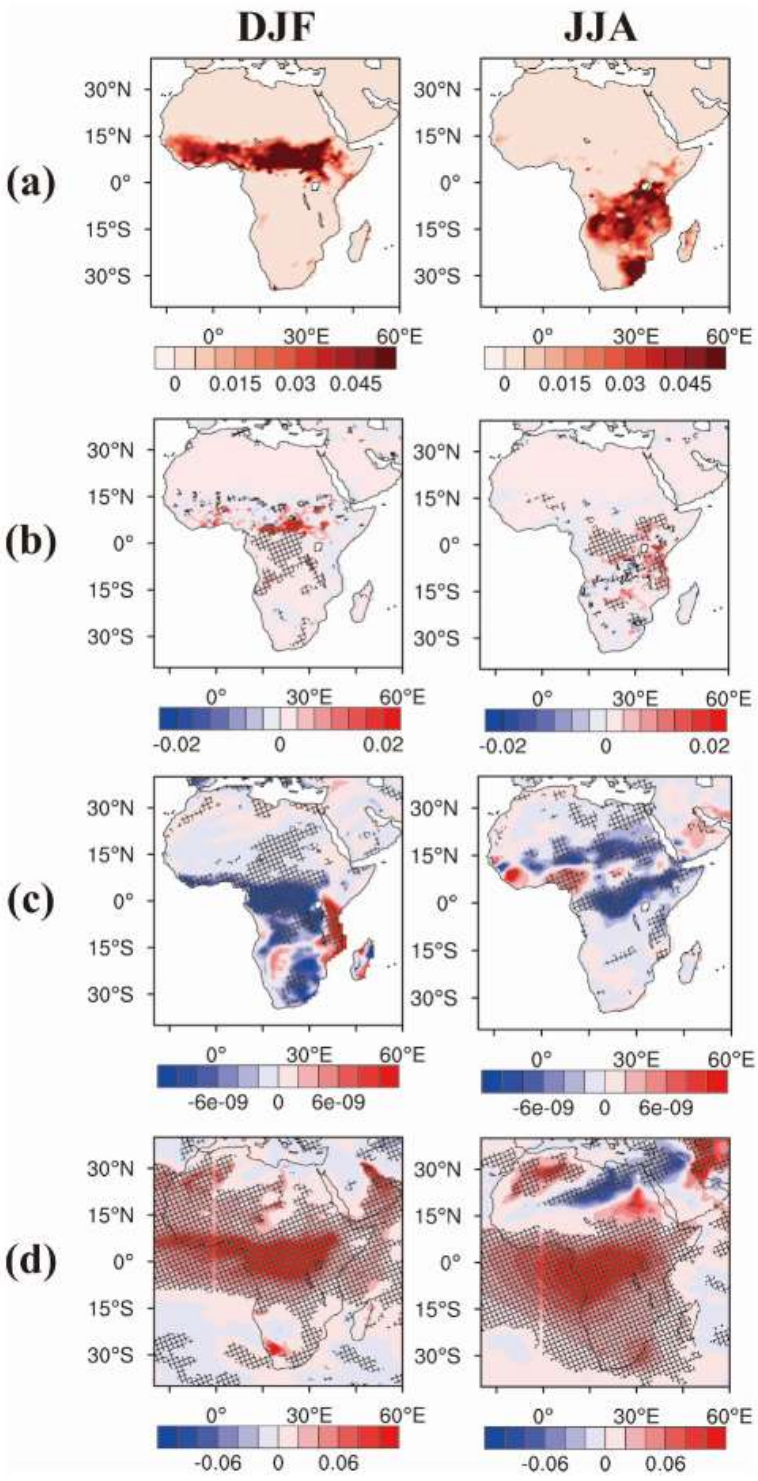

Figure 18 - Fire aerosol induced effect in Africa in DJF and JJA. (a) Burned fraction without fire aerosol impact. (b) Burned fraction change caused by fire aerosol effects. (c) Precipitation change due to fire aerosol effects (unit: m/s). (d)

AOD change from fire aerosol impact. The grid boxes that have passed the paired Student's t-test are shaded.

3.3.3 The temporal and spatial shift of fire aerosol feedback

The mechanism of fire-induced precipitation change is further demonstrated in Figure 19. Figure 19(a) shows that in DJF the latitude with the maximum BF change because BB aerosol feedback is at 3.3° N, which is 4.7° south to the peak latitude of BF over Africa. The maximum increase of BF in DJF accounts for 89% of local BF and is 20% compared to the maximum zonal mean BF over Africa. In JJA the peak of BF change due to BB aerosol feedback is at 4.2° S, which is 8.5° north to the peak latitude of BF over Africa. The maximum increase of BF in JJA accounts for 16% of local BF, and is 12% compared to the maximum zonal mean BF over Africa. The prevailing meridional wind direction over 0-4 km is to the south over the main fire region in DJF (0° - 15° N), and is to the north over the main fire region in JJA (0° - 20° S). Figure 19(b) shows the temperature change because of BB aerosol impact. Over the burning region, the temperature decreases at the lower troposphere (0-2 km) by 0.30 °C and increases by 0.09 °C at the mid-high troposphere (3-6 km). This change of the temperature vertical profile indicates that the BB aerosol tends to stable the atmosphere, weaken the convection, thus suppress the precipitation. Figure 19(c) and (d) indicated the cloud liquid amount is increased in regions with increased AOD and decreased precipitation. Figure 19(c) shows that the precipitation decreased by 0.34 mm/day in DJF and 0.19 mm/day in JJA, and the precipitation suppression is mainly at the edge of the fire region. At the edge of the fire region, which is relatively dry, compared to cloud condensation nuclei (CCNs), water vapor is relatively limited for precipitation. With the same amount of water input, when

more aerosol serves as CCNs, humidity is limited for cloud droplets to grow, thus precipitation is reduced. Therefore, the weakening of convection and the increased CCNs with limited humidity are two reasons to suppress the precipitation, then trigger the positive BB aerosol feedback. This mechanism is also described in (Tosca et al., 2015).

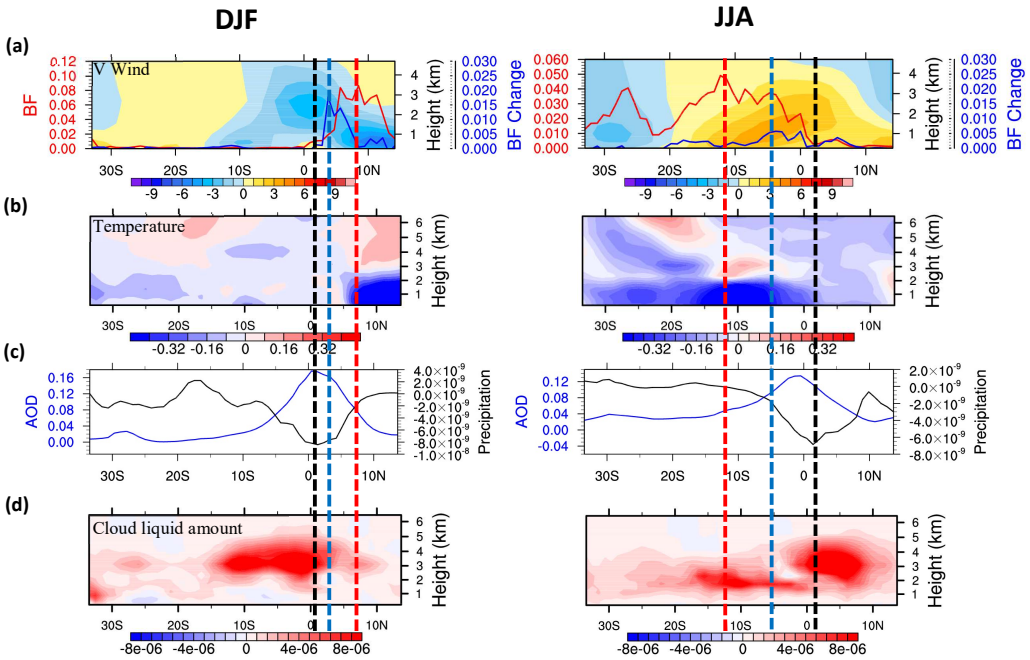

Figure 19 - The effect and mechanism of meridional distribution of fire aerosol feedback, averaged between 15°E to 40°E, in DJF and JJA. (a) The burned fraction without BB aerosol feedback (in red lines) and the burned fraction change from no BB aerosol feedback simulation to BB aerosol feedback simulation (in blue lines). Colored contours represent averaged northward-southward wind speed (in units of m/s) (b) Temperature (in units of kg/kg) change from no BB aerosol feedback simulation to BB aerosol feedback simulation. (c) AOD (in blue lines) and precipitation (in black lines, in units of m/s) change from no BB aerosol feedback simulation to BB aerosol feedback simulation. (d) Solar heating rate (in units of K/s) change from no BB aerosol feedback simulation to BB aerosol feedback simulation. The dash lines in red represent the latitude of peak burned area; dash lines in blue represent the latitude of peak burned area change, and the black dash lines represent the latitude of the most reduced precipitation.

The localized precipitation suppression is hard to increase burning, the major fire region and season is dry enough and the fuel load is limited for more fire. In this case, the wind plays a critical role to transfer the fire impact to the regions where the potential fire probability is precipitation driven. As mentioned before, the fire aerosol feedback occurs not evenly over the fire region but has a strong effect at the edge of fire regions, causing a fire region expansion. Figure 19(a) shows the direction of this expansion. The meridional distribution of fire aerosol impacted BF change is shifted from the meridional BF distribution. In DJF, the shift of fire aerosol impact is to the south; while in JJA, the shift is to the north. Both shifts of burned fraction agree with the meridional wind direction. The peak latitude of AOD and precipitation change, shown in Figure 19(c), also agrees with the wind direction. In DJF, the location that precipitation reduction is highest is south to the burning region, and in JJA, the strongest precipitation reduction is to the north of the fire region. AOD peaks agree with precipitation reduction. As shown in Figure 19, in both seasons, the peaks of BB aerosol feedback change are located between the burned area peak and the precipitation reduction peak, which indicates that the strongest fire feedback occurs on regions that have enough fuel load and sensitivity to precipitation change.

The wind-driven spatial shift of the fire impact is caused by the transport of aerosols, and with the seasonal variation of wind and fire regions, the effects of fire feedback extend spatially and temporally. The impact from fire aerosols to precipitation change is in a time scale of weeks, and the likelihood of fire increases in dry conditions, which makes it possible to transport the effect temporally from season to season. Figure 20 shows the fire feedback shift in all seasons (DJF, MAM, JJA and SON). In MAM and SON, fire is weaker than major fire seasons, and spatial burning region shift is less

significant than that in DJF and JJA. However, as the sporadic burning is over the continent in MAM and SON, the feedback is still transporting from and to the neighboring seasons.

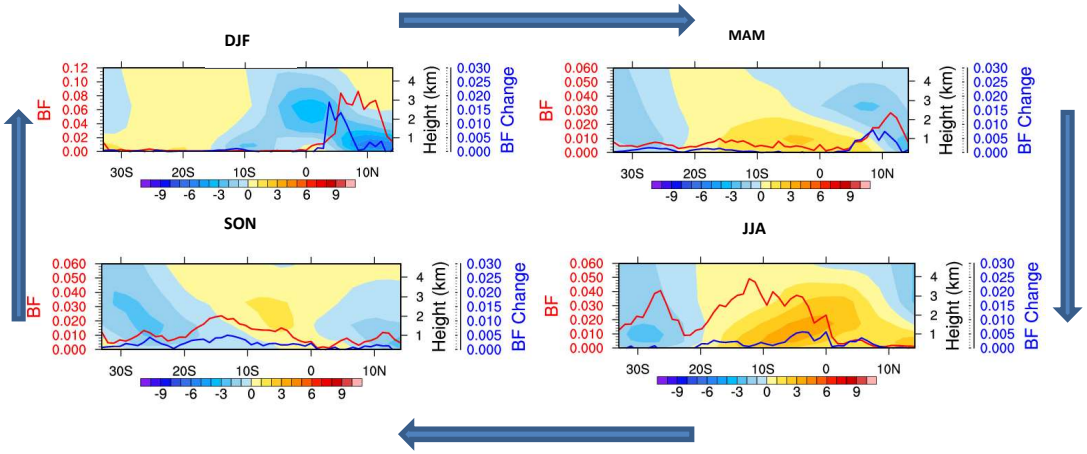

Figure 20 - Seasonal meridional distribution of fire aerosol feedback, averaged between 15°E to 40°E. The BF without BB aerosol feedback (in red lines) and the BF change from no BB aerosol feedback simulation to BB aerosol feedback simulation (in blue lines). Colored contours represent the averaged northward-southward wind speed (in units of m/s)

Figure 21 is based on the comparison between cases with and without fire aerosol feedback shown in Figure 20, which sketches the comprehensive intraseasonal and interseasonal feedback of fire aerosol. With the fact that the precipitation change can only affect fire over the precipitation reduced region, the interseasonal feedback is located in the region of fire enhancement in the last season. Figure 20 shows that the interseasonal feedback is happening for all seasons. In DJF, the intraseasonal burning enhancement locates at 3.3° N, which is 4.7° south to the peak of DJF total BF. This enhancement from DJF continues to MAM, and triggers the burning at the edge of the fire region in MAM. The intraseasonal fire enhancement from local burning in MAM is at 7° N and 16° S, and continues to JJA. In JJA the fire in Southern Africa is transported to the sea, without causing feedback; while the tropical fire triggers the enhancement of burning at 3° N, that

also goes to SON. Because the wind direction of the SON fire region is spreading out to both ways and the local burning is relatively low in SON, the intraseasonal burning enhancement is spread out with the fire region. The peak of SON BB aerosol feedback is at 13° S, which continues to DJF. This interseasonal enhancement has increased local burning in DJF by more than 30%, but with very limited burning because of the local rainy season.

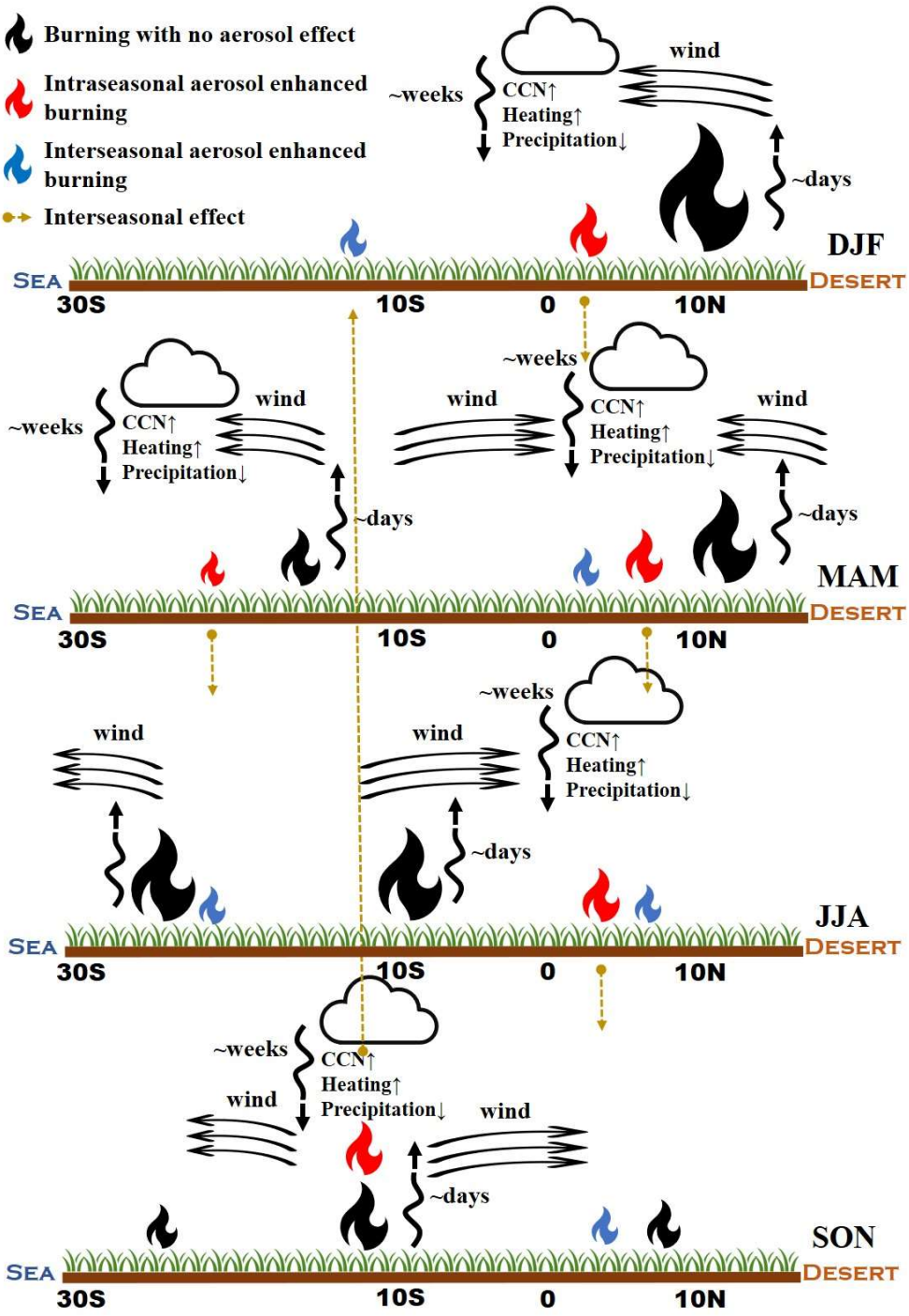

Figure 21 - A sketch of the temporal continuity and spatial shift of fire aerosol feedback. The colors of fire icons represent burning with no fire aerosol feedback (black), burning of fire aerosol feedback in the same season (red), and burning of fire feedback across the season (blue). The size of fire icons qualitatively represents

the burned fractions. The yellow dash lines point to the locations of the interseasonal feedback. The mechanism of the feedback is also sketched in this figure.

3.4 Conclusions

We use RESFire model and address a positive feedback loop between fire and climate in Africa. Biomass burning aerosol emissions increase CCN concentrations in the free troposphere and enhance solar heating, thus reduce precipitations and increase fire activity. The fire feedback shifts to the region on the transport path of biomass burning aerosols, and regions over which the burning is sensitive to precipitations. This positive feedback is recurrent in a meteorological time scale and has intraseasonal to interseasonal impact. This feedback suggests a mechanism contributing to the interannual fluctuation of African biomass burning, also plays a role in understanding the observed and modeled interannual trend of biomass burning in previous studies.

This positive feedback loop between fire and climate indicates a potential long-term impact from extreme fire event and macroscopic increase of fire activity, yet has limited sensitivity to small fires that have minor impact on cloud or on regions that are extremely drought or fuel-limited, because fire aerosol emissions would not drive significant precipitation change when the region is dry enough, the precipitation decrease will not trigger fire if local combustible matters are limited. We suggest future studies on the long-term measurement of the post-extreme-fire fluctuation and fire aerosol feedback over other regions.

CHAPTER 4. MARINE BIOGENIC GLYOXAL SOURCES ENHANCE OXIDATION IN THE MARINE BOUNDARY LAYER

4.1 Introduction

Glyoxal is one of the smallest bi-carbonyl compounds and is an important oxidation product of many VOCs. Glyoxal plays a significant role in atmosphere photo-chemical activity, SOA formation (Liggio et al., 2005a; Liggio et al., 2005b), ozone production (Edwards et al., 2014), and brown carbon (Shapiro et al., 2009). The source of glyoxal over the continent is both biogenic and anthropogenic. Two of the major precursors of glyoxal are isoprene (biogenic) and acetylene (anthropogenic) (Z. Liu et al., 2012). The major chemical sink of glyoxal is against oxidation (by OH) and photolysis, with a short lifetime of 1~2 hrs. glyoxal can be photolyzed and produce HO2, a major atmospheric radical that speed up the atmospheric oxidation processes, such as ozone and sulfate formation.

Fu et al. (2008) estimated a global glyoxal budget of 45 Tg yr-1 on the basis of GEOS-Chem global model, but this budget is mainly over the continent. Evidences from in-situ and satellite observations show the widespread distribution of glyoxal over marine boundary layer (MBL) in both coastal sites (Seaman et al., 2006; Sinreich et al., 2007) and remote regions (Coburn et al., 2014; Lawson et al., 2015), indicating a potentially large marine source of glyoxal. This source has been missed in current global model simulations (Fu et al., 2008; Lerot et al., 2010), remaining the effect of marine glyoxal to atmospheric oxidation state unknown.

This missing marine glyoxal source is unidentified yet, but probably biogenic (O'Dowd et al., 2004; Rinaldi et al., 2011). Heterogeneous oxidation of dissolved organic carbon at the air-water interface (S. Zhou et al., 2014) can produce VOC from the ocean. Zhu & Kieber (2019) observed relatively higher seawater glyoxal concentration over the biogenically productive regions and measured 0.06-0.2 nmol L-1 h-1 of the photoproduction rate of glyoxal. Recent studies in the Arctic boundary layer also demonstrated a biogeochemical connection between oxygenated VOCs and the ocean microlayer(Mungall et al., 2017). On the other hand, measurements show that the flux of the glyoxal air-sea exchange is downwards (Lawson et al., 2015; Sinreich, Coburn, Dix, & Volkamer, 2010; Zhu & Kieber, 2019) Volkamer et al. (2015) measured the vertical profile of glyoxal, showing that the glyoxal concentrations are similar from the surface to 2 km, and the highest glyoxal concentration located at the altitude of ~700 m. We discuss this potential biogenic source of MBL glyoxal in the following section.

In this study, we used inverse modeling to estimate the MBL glyoxal source based on the observation of glyoxal vertical column density (VCD) from the satellite spectrometer measurements of Global Ozone Monitoring Experiment–2A (GOME2-A), Ozone Monitoring Instrument (OMI) and SCanning Imaging Absorption spectroMeter for Atmospheric CHartographY (SCIAMACHY) (Alvarado et al., 2014; Burrows, Hölzle, Goede, Visser, & Fricke, 1995). This is the first modeling study to consider the impact of marine glyoxal using a profiled glyoxal source over 0-2 km according to recent findings of the vertical profile of glyoxal (Volkamer et al., 2015). We apply this source into the CESM to estimate the impact of glyoxal to the oxidation state of the MBL.

4.2 Data and Methods

4.2.1 The CESM model and satellite datasets

We executed glyoxal simulations based on the CESM. Its atmospheric component, the CAM5 (Neale et al., 2010), is online and the other parts of CESM (including land, ocean, sea ice and land ice) are set offline. Atmospheric chemistry, aerosols, convection scheme and cloud physics are well coupled in the model(X. Liu et al., 2012; Morrison & Gettelman, 2008; G. Zhang & McFarlane, 1995). We nudge CAM5 meteorological field (temperature, humidity and wind) to GEOS-5.2.0 meteorological data products(Suarez et al., 2008). We use CAM5 with a spatial resolution of 1.9°x2.5° to simulate all essential atmospheric compounds and VOC including glyoxal. Biomass burning emissions are from GFED4s (Giglio et al., 2013; J. Randerson et al., 2012). IPCC AR5 emission dataset (Lamarque et al., 2010) is used as anthropogenic emissions.

The top-down marine glyoxal source estimation is on the basis of the tropospheric glyoxal column Version 1.5 (Alvarado et al., 2014) retrieved from GOME-2A, OMI, and SCIAMACHY. The inversed glyoxal sources from all satellite instruments show good correspondence over the land. Marine glyoxal seasonal cycle and spatial distribution from different satellite products are also similar, but the average glyoxal VCD differs with satellite products. A possible reason is that the local time of detection for satellites is different. In addition, compared to OMI and GOME-2A, SCIAMACHY has coarser spatial resolution but also global coverage (6 days global coverage for SCIAMACHY, 1-day global coverage OMI and GOME2). The comparison of the glyoxal retrieval dataset from OMI, GOME-2A, and SCIAMACHY over the ocean is shown in Figure 22 and Figure 23.

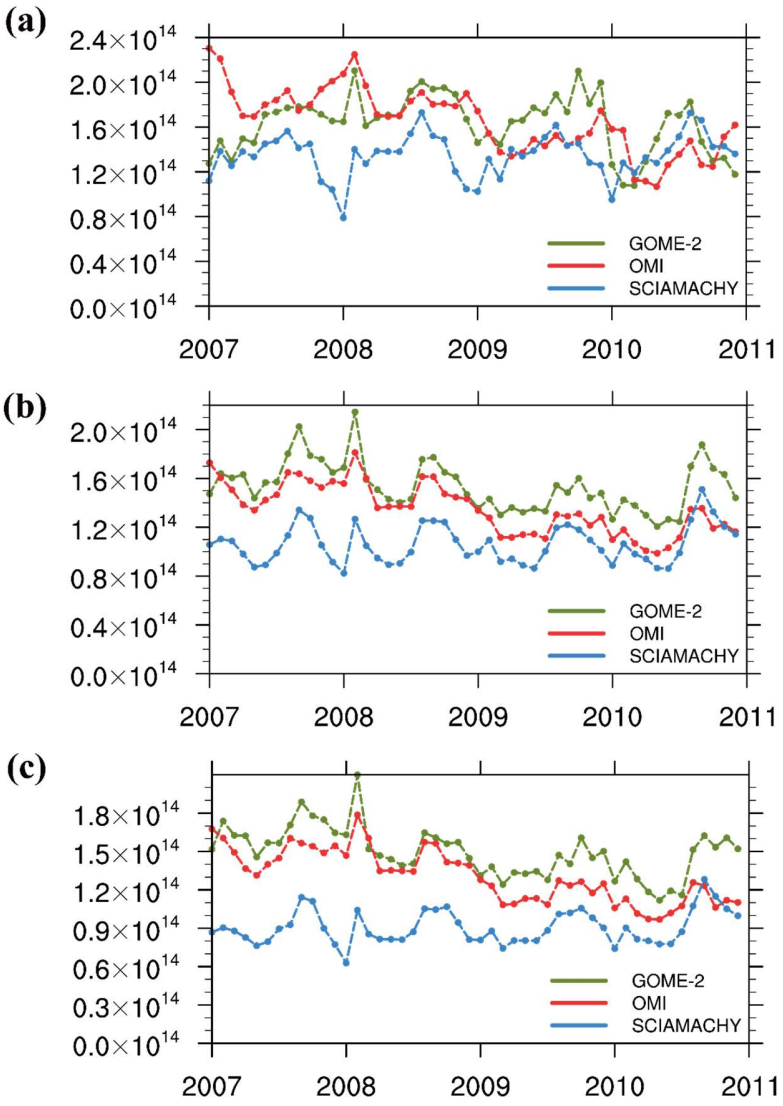

Figure 22 - The zonal mean seasonal cycle of satellite retrieved marine glyoxal VCD (unit: molecules/cm^2)of GOME-2A, OMI and SCIAMACHY from 2007 to 2010, averaged in (a) 30°N-90°N, (b) 30°S-30°N, (c) 30°S-90°S.

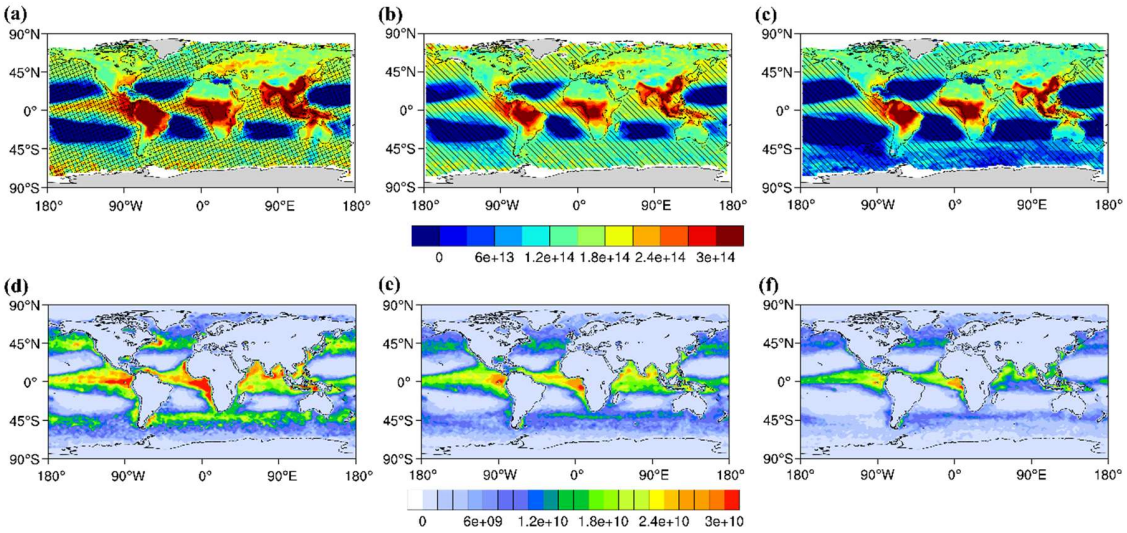

Figure 23 – (a) to (c) show the global distribution of Glyoxal VCD (unit: molecules/cm^2) retrieved from (a) GOME-2A, (b) OMI and (c) SCIAMACHY from 2007 to 2010. The shaded area is the marine region that is used in the inversed model to estimate the marine glyoxal source. (d)–(f) show the annual mean estimation of glyoxal production based on (d) GOME-2A, (e) OMI and (f) SCIAMACHY satellite observations from 2007 to 2010 (Unit: molecules/cm^2/s)

4.2.2 The source of MBL glyoxal

As a glance at the marine glyoxal contribution to the global glyoxal budget, we estimate the total mass ratio of marine glyoxal to the global glyoxal based on satellite observations, then we find that 48% of glyoxal is over the ocean. Global models without considering the marine source cannot simulate enough glyoxal over the remote ocean. Figure 24 shows the default simulated glyoxal VCD. Since no marine source of glyoxal in the model, the default model simulation cannot produce enough glyoxal over the remote ocean compared to satellite observation shown in Figure 25(b). Over mid-latitude downwind regions, because of the short lifetime of glyoxal in oxidation, transport of glyoxal from the continent is near to coastal regions. Although the model simulated significant glyoxal column concentration over the northern mid-latitude Atlantic Ocean,

the simulated column concentration is only less than 20% of the satellite retrieved glyoxal column concentration. This modeled marine glyoxal probably comes from long-term precursors of glyoxal, such as acetylene (Xiao, Jacob, & Turquety, 2007). Nevertheless, long-term anthropogenic glyoxal precursors are still far to explain the high-level glyoxal over the global marine regions.

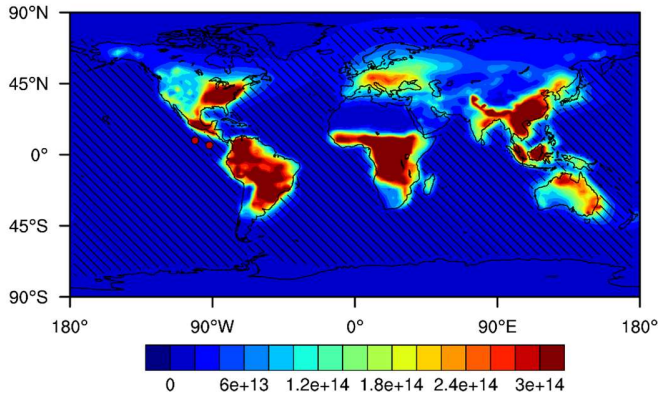

Figure 24 - The simulate global distribution of glyoxal VCD in the default CESM model in 2009 (unit: molecules/cm^2). The shaded area is marine regions that the estimated marine glyoxal production is included. The two scatters represent the aircraft observed glyoxal VCD by Volkamer et al. (2015).

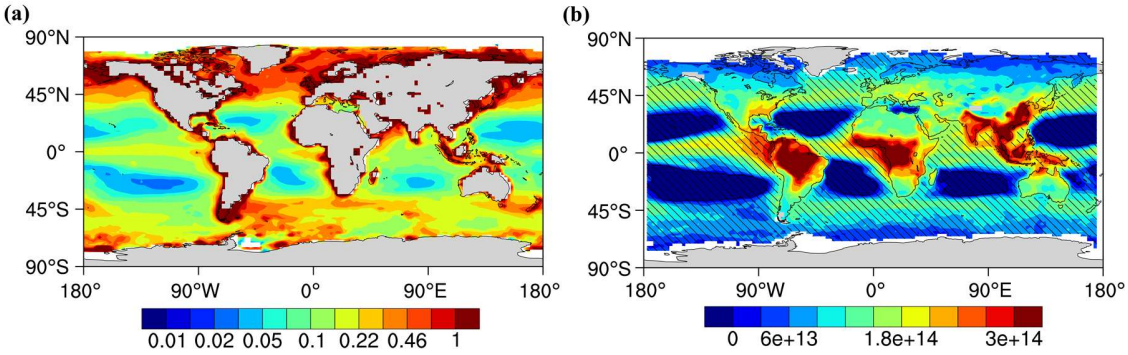

Figure 25 – (a) Global distribution of Chlorophyll-A concentration (unit: mg/m^3) in MODIS-Aqua instrument averaged from 2005 to 2009. (b) Global distribution of Glyoxal VCD (unit: molecules/cm^2) averaged in GOME-2A, OMI and

SCIAMACHY from 2007 to 2010. The shaded area is marine regions that are used in the inversed model to estimate the marine glyoxal source.

We compared the annual mean distribution of glyoxal VCD and near-surface chlorophyll-A concentration. The chlorophyll-A concentration, retrieved from the MODIS on the Aqua satellite (NASA Goddard Space Flight Center, 2014), can represent the distribution of phytoplankton biomass in seawater. Figure 25(b) shows the annual averaged satellite retrieved VCD of glyoxal. Significant glyoxal is over the ocean. Its spatial distribution agrees well with satellite retrieved annual mean near-surface chlorophyll-A concentration, shown in Fig. 1a. High-level chlorophyll-A and marine glyoxal VCD appears along the equator, and from mid-latitude (~40°) to polar regions in both northern and southern hemisphere. Continental glyoxal has precursors from multiple sources including anthropogenic emissions, biomass burning and biogenic emissions(Fu et al., 2008). Because of the strong spatial correspondence between glyoxal VCD and chlorophyll-A concentrations, we propose a potential biogenic source of glyoxal.

The seasonal cycle of marine glyoxal also contains useful information for understanding the glyoxal source. In Figure 26(a), the tropical Pacific glyoxal VCD shows clear double peaks in March and September. We compare the seasonal cycle of tropical glyoxal VCD with variables related to it, including chlorophyll-A concentrations, temperature and surface downwelling solar flux. Surface solar downwelling flux (Figure 26(d)) has a similar bimodal pattern in March and September, but the levels of the two peaks are different. Chlorophyll-A concentration (Figure 26(b)) has a peak in March, and the peak in August is not significant, but chlorophyll-A sharply decline after August. The seasonal cycle of temperature, shown in Figure 26(c), has only one single peak. The

correlation coefficient r is 0.59 between the seasonal cycle of glyoxal and the product of chlorophyll-A and surface downwelling solar radiation, significantly higher than the correlation coefficient between glyoxal and any one of them specifically (r = 0.25 between glyoxal and chlorophyll-A, and r = 0.52 between glyoxal and surface downwelling solar radiation). Over the temperate ocean, glyoxal and all the related components have similar seasonal variation (higher in summer and lower in winter). Over the tropic ocean, temperature, light, and biogenic activity have different seasonal variability, and the seasonal variability of glyoxal agree the most to the interaction between light and biogenic activity, indicating that the marine glyoxal is probably related to the photochemical reactions of marine biogenic VOC over the tropical ocean.

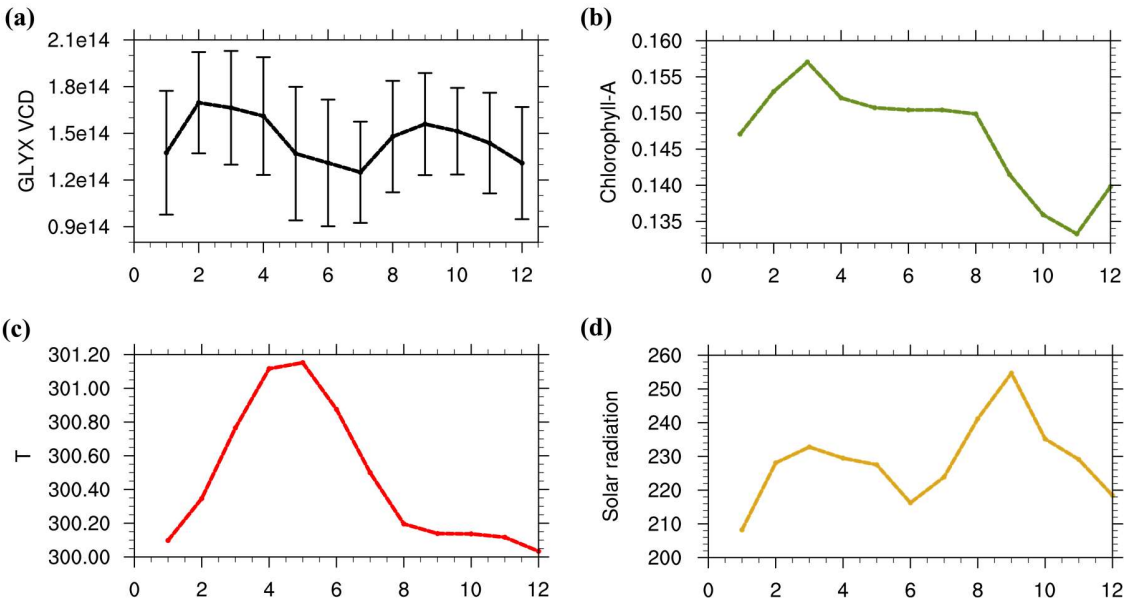

Figure 26 - Seasonal cycles on tropical Pacific regions (10°S - 10°N, 100°W - 160°W) of glyoxal and the potentially related meteorological fields. a, Glyoxal in units of molecules/cm^2. b, Chlorophyll A surface concentrations, in units of mg/m3. c, GEOS5 surface temperature seasonal cycle averaged from 2007 to 2010, in units of K. d, CESM simulated seasonal cycle of surface downwelling solar radiation flux (FSDS) in 2009, in units of W/m2.

4.2.3 The inverse model

In this study, we use inverse modeling to quantify the underestimation of marine glyoxal. We assume a missing precursor emission (E_i). Based on previous studies of VOC inverse modeling using satellite column observations(Fu et al., 2007; Z. Liu et al., 2012; Shim et al., 2005), we put forward a linear relationship between glyoxal VCD (C_{CHOCHO}) and E_i:

$$C_{CHOCHO} \approx \sum_{i=1}^{n} E_i \times \frac{\partial C_{CHOCHO}}{\partial E_i} \quad (8)$$

This approach requires a short lifetime of the precursor. The comparison between Fig. 1b and Fig. S5c indicates that not only the marine glyoxal precursors are negligible in the default model, but also the continental emissions of long-life precursors of glyoxal, such as acetylene, have a negligible contribution to marine glyoxal. As a result, we derive the relationship between model underestimated glyoxal VCD from short time precursors ($\Delta C'_{CHOCHO}$) and the corresponding model underestimated precursor emissions (ΔE_i):

$$\Delta E_i \approx \frac{\Delta C'_{CHOCHO}}{\partial C_{CHOCHO} / \partial E_i} \quad (9)$$

Therefore, as the start of the inversion, the above equation can be written as:

$$E_{i,priori} \approx \frac{\Delta C_{CHOCHO,ocean}}{\partial C_{CHOCHO,ocean} / \partial E_{i,ocean}} \quad (10)$$

We first estimate a priori glyoxal production (Martin et al., 2003):

$$E_{i,priori} = \frac{C_{CHOCHO}}{lifetime} \quad (11)$$

Where "lifetime" represents the lifetime of glyoxal in the daytime (~2 hr) (Coburn et al., 2014). Then, we update a priori glyoxal production by a posteriori glyoxal production based on model simulation:

$$E_{i,posteriori} = \frac{C_{CHOCHO}}{C_{CHOCHO,simulated}} \times E_{i,a\ priori} \quad (12)$$

We iterate using this equation for each 1.9°x2.5° grid box and each monthly mean. Because of the assumption that glyoxal is produced from photo-chemical mechanisms or biological process, the glyoxal production is not temporally even and only occur at daytime. In addition, because the measured downward source of surface glyoxal, we expand the marine glyoxal production $E_{i,posteriori}$ to a profiled source based on an aircraft observed vertical profile, which shows that vertical glyoxal peak is at ~700m and is mixed from the surface to 2 km (Volkamer et al., 2015). After 2 iterations, the variance between the observed and simulated marine glyoxal VCD. We conduct 3 CESM simulations including the marine glyoxal production estimated from OMI, GOME-2A, and SCIAMACHY over the year 2009 with a 1-month spin-up, and we use the average of the 3 simulations as the best model including marine glyoxal production. We also run a default model with no marine glyoxal production as a baseline.

4.2.4 The neural network approaches

For a better understanding of factors related to marine glyoxal production, we set up a neural network (NN) model to parameterize the inverse model estimated marine glyoxal production using independent variables of surface chlorophyll-A concentrations, surface downwelling solar flux and temperature. We train the model using the marine glyoxal estimation based on OMI satellite observation averaged from 2007 to 2010, MODIS retrieval of surface chlorophyll-A concentrations averaged from 2005 to 2009, CESM model simulation of surface downwelling solar flux and GEOS-5 reanalysis of surface temperature in 2009. The model downwelling solar flux is calculated using Rapid Radiative Transfer Method for Global Climate Models (GCMs) (RRTMG). The data of all variables are the monthly mean with a spatial resolution of 1.9°x2.5° in one year.

We built the NN model using the MATLAB® 2015b neural network toolbox. To improve the efficiency of the parameterization, we build separate NNs to handle annual mean spatial distribution and seasonal cycle per grid box. We first build a NN to model the annual mean glyoxal production in each grid box using the annual mean of all independent variables. Then we built another NN model to learn the normalized seasonal cycle for each grid box using the seasonal cycle of all independent variables. Separating spatial and temporal patterns using two NNs significantly improve the model performance compared to using one single NN model to derive marine glyoxal production. We run each NN with a 70% training set, 15% cross-validation set and 15% test set. 5 simulations with 10, 15, 20, 25 and 30 hidden layers showing that increasing the number of hidden layers from 10 to 30 do not show improvement of the simulation.

As is shown in Figure 27(a), NN parameterized glyoxal emission caught the high-production regions over the ocean compared to the OMI satellite inversed glyoxal

production shown in Figure 23(b). As for the temporal pattern, NN parameterization captured the seasonal cycle very well in all 3 major latitude bins, shown in Figure 27(b) to (d). The good correspondence of inversed result and the NN modeled result indicates that the information from temperature, light and biogenic activity is enough to derive the glyoxal source. Furthermore, we discuss the contribution of independent variables in simulating the spatial and temporal pattern of marine glyoxal production. To estimate the contribution from one variable to the seasonal cycle, we remove the seasonal cycle of that variable in the dataset by replacing all data of the variable to be the annual average over the corresponding grid box. To estimate the contribution of one variable to simulating the spatial distribution of the marine glyoxal production, for each value in one grid box, we replace it with the zonal mean in an interval of ± 10 degrees of latitude centered on the grid box. We conduct sensitivity runs using the modified data, and calculate the variance between the NN model result and inversed model result. Figure 28 shows the sensitivity of the input independent variables, which is defined as the percentage of increase of the variance between the inversed model estimation and the NN model output of the marine glyoxal production due to removing specific information from the input independent variables. The increase of the variance is the most when removing the spatial information of chlorophyll-A, and removing the temporal information of solar radiation, which indicates that the chlorophyll-A concentrations are dominating the spatial distribution of glyoxal, while solar radiation is dominating glyoxal seasonal cycle; the temperature has minor contribution compared to the other two variables. The consistency between the NN model and the glyoxal production estimated using inverse modeling (discussed in Section 4.2.3) supports the discussion that the marine glyoxal source is probably biogenic.

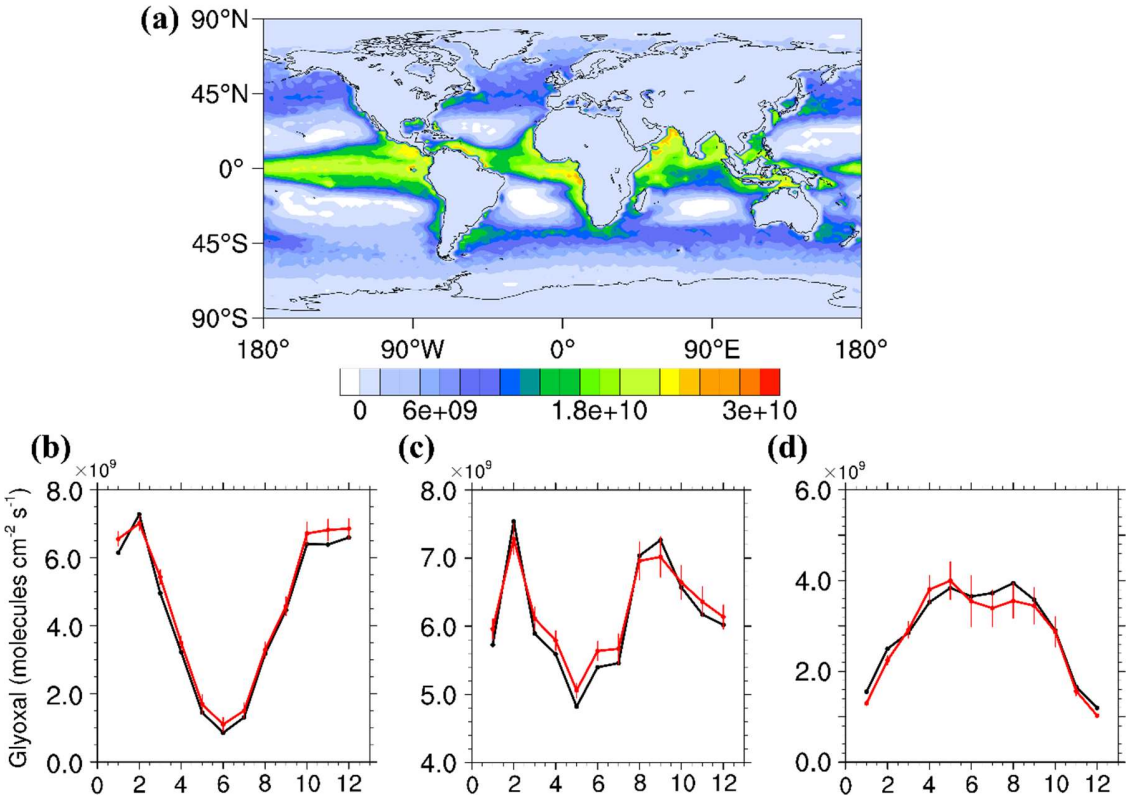

Figure 27 - (a) The annual mean marine glyoxal production estimated from a neural network (NN) approach based on the inverse model estimation from 2007-2010 OMI satellite retrieval in the unit of molecules/cm^2/s. (b) to (d) show the seasonal cycle of the NN estimation (red) the inverse model estimation (black) averaged in (b) 70°S - 30°S, (c) 30°S - 30°N, and (d) 30°N-70°N.

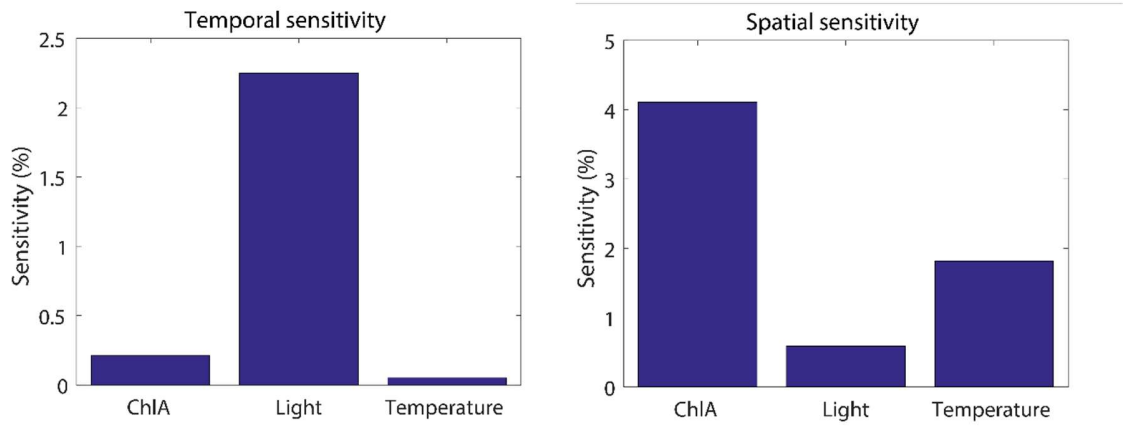

Figure 28 - The temporal and spatial sensitivity (the increasing percentage of the variance between the input and output of the NN model data due to removing

specific information from the independent variables) of variables used in the NN model estimation of glyoxal production.

4.3 Results

Although the mechanisms on glyoxal production are still in discussion, measurements in both coastal and remote marine sites show the high-level MBL glyoxal. Considering the short lifetime of glyoxal photochemical loss and the spatial-temporal correspondence between marine glyoxal column and marine biogenic precursors, we assume the model underestimation of marine glyoxal can be constrained by the input of marine glyoxal production. We derive a marine source of glyoxal by constraining column concentrations between the satellite retrieval and model simulation using the inverse modeling method discussed in Section 4.2.3. Figure 29(a) shows the annual marine production of glyoxal derived in the inverse model. We have estimated a marine glyoxal budget of 43 ± 10 Tg/yr. The regions with high-level glyoxal production are the tropics and mid-high latitude regions (>40°), which are consistent with the chlorophyll-A spatial distribution. Figure 29(b) and Figure 29(c) indicates the difference with and without inversed glyoxal marine source in CESM. The constrained spatial distribution of marine glyoxal agrees well with the satellite observation.

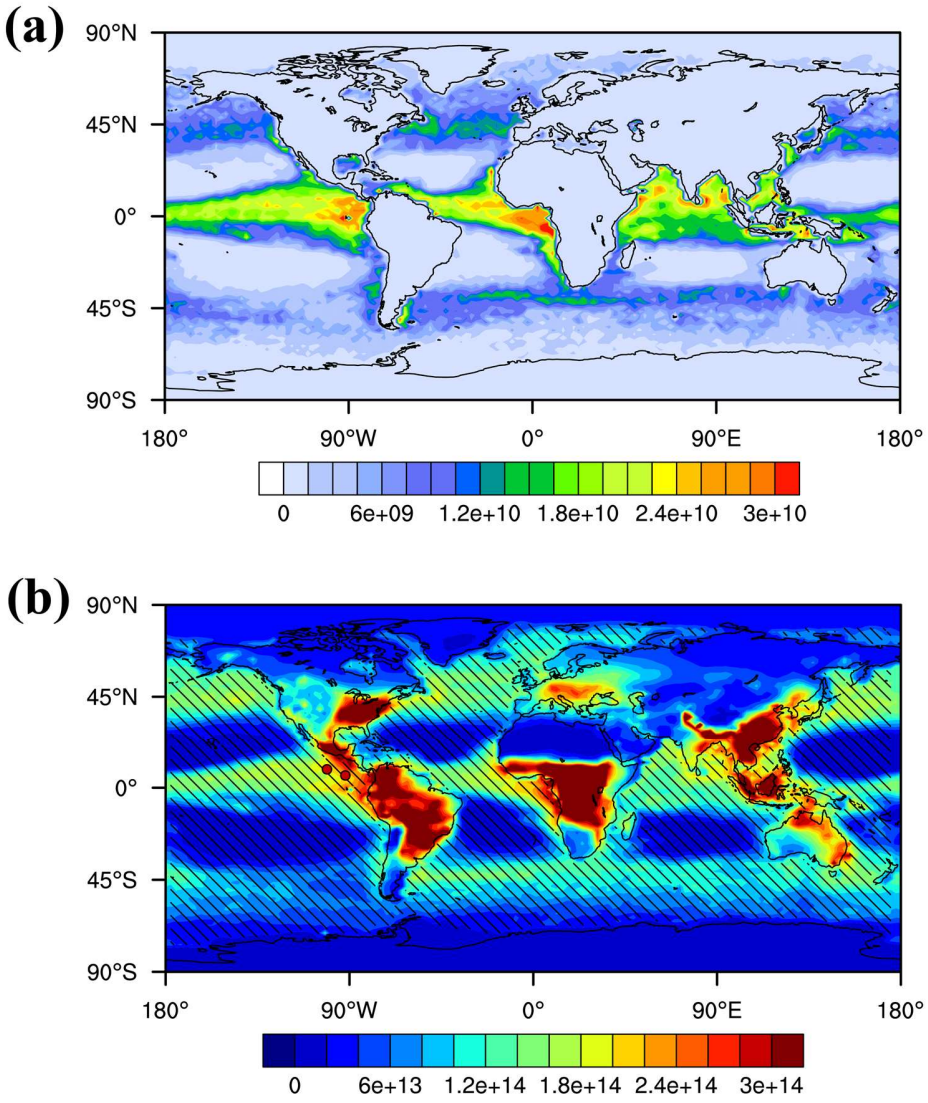

Figure 29 – (a) The annual mean estimation of glyoxal production averaged from the inverse model based on OMI, GOME-2A and SCIAMACHY observations from 2007 to 2010 (Unit: molecules/cm^2/s). (b) The CESM simulation of annual mean glyoxal VCD in 2009 (unit: molecules/cm^2). The shaded area is marine regions that the estimated marine glyoxal production is included. The two scatters represent the aircraft observed glyoxal VCD by Volkamer et al. (2015).

To evaluate the performance of CESM applied with the marine glyoxal production, we compared the measurements of the surface or MBL averaged glyoxal concentration with the corresponding monthly mean of simulated glyoxal concentration in a simulation

of the year 2009. We summarized this comparison in Table 5 and Figure 30. Compared to the default model with no significant marine glyoxal distribution, model simulation with inversed marine glyoxal production has better consistency with site observations. The observations cover the tropical Pacific, Southern Ocean, Caribbean Sea, and Northern Atlantics. For most of the sites, model simulations have shown similar spatial distribution to observations. Except for the measurements of RF12 and RF17 are MBL measurements averaged below 2 km, all the other glyoxal measurements are close to the sea surface. The corresponding model result (45 ppt at RF12 and 54 ppt at RF17) overestimates the observation. The aircraft observation by Volkamer et al. (2015) indicates that a significant amount of glyoxal is over the free troposphere. The model simulation catches the glyoxal vertical profile between 0-2 km by constraining to the observation, but underestimate the glyoxal distribution over the free troposphere, indicating a missing the secondary production of glyoxal from long-lifetime precursors. The comparison of model simulation and aircraft measured glyoxal vertical profile at RF17 is shown in Figure 31. With a limited understanding of free troposphere glyoxal, and the consistency between simulated and satellite observed glyoxal VCD, we potentially overestimate the MBL glyoxal and underestimation glyoxal over the free troposphere. The surface glyoxal concentration agrees well between the observation and the simulation with marine glyoxal production, except that we underestimate the observation at Gulf of Maine (42°N, 67°W) in July 2004 (Sinreich et al., 2007), where glyoxal concentration is largely affected by the continental export. The best model shows significantly better agreement with the observations (correlation coefficient $r = 0.76$, and a slope $k = 0.59$ for linear regression) then the default model simulations ($r = -0.05$, $k=0.02$).

Table 5 Summary of measurement time and location for surface and MBL glyoxal observations.

Name	Time	Local time (LT)	Latitude	Longitude
Salt Point (Seaman et al., 2006)	Aug-Sep 2005	11-14LT	39°N	123°W
Gulf of Maine (Sinreich et al., 2007)	Jul 2004	6-18LT	42°N	67°W
Caribbean Sea (X. Zhou & Mopper, 1990)	Oct 1988	mean	15°N	66°W
Sargasso Sea coast (X. Zhou & Mopper, 1990)	Oct 1988-Mar1989	mean	15°N - 27°N	94°W - 66°W
Tropical Pacific NH (Coburn et al., 2014)	Jan-Mar 2012	mean	5°N - 20°N	133°W - 110°W
Tropical Pacific SH (Coburn et al., 2014)	Jan-Mar 2012	mean	5°S - 10°S	110°W - 93°W

Table 5 continued

Tropical Pacific NH (aircraft RF12) (Volkamer et al., 2015)	Jan-Feb 2012	mean	8.5°N	101.8°W
Tropical Pacific NH (aircraft RF12) (Volkamer et al., 2015)	Jan-Feb 2012	mean	6.1°N - 7°N	90°W – 91.6°W
Cape Grim (Lawson et al., 2015)	Aug-Sep 2011	mean	40°S - 44°S	140°E - 144°E
Chatham Rise (Lawson et al., 2015)	Feb-Mar 2012	mean	50°S - 40°S	175°E - 175°W
Tropical Eastern Pacific Ocean (Sinreich et al., 2010)	Nov2008-Jan2009	mean	15°S - 5°N	85°W - 95°W

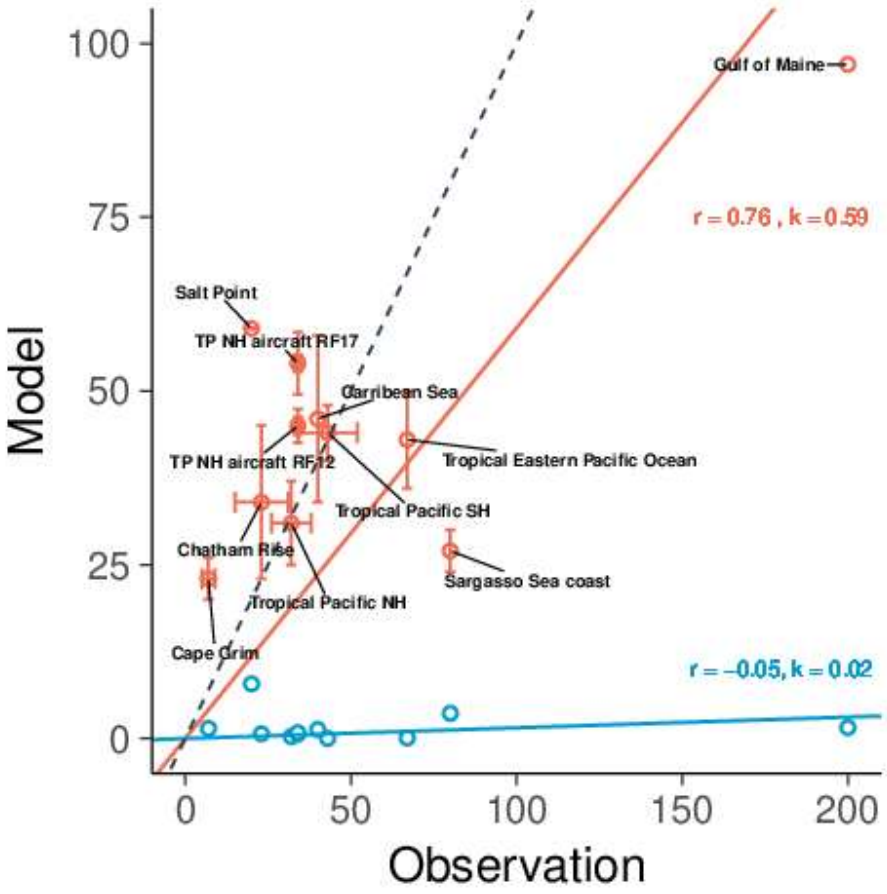

Figure 30 - The best model simulation with inversed production of marine glyoxal (red scatters) and default model simulation with no marine production of glyoxal (blue dots) are compared to the observations. Solid lines represent the corresponding linear regression compared to the 1:1 reference line (dash line). Vertical error bars represent the standard deviation of the model result. Horizontal error bars represent the observation error (if available). The summary and reference of the observation data are shown in Table 5.

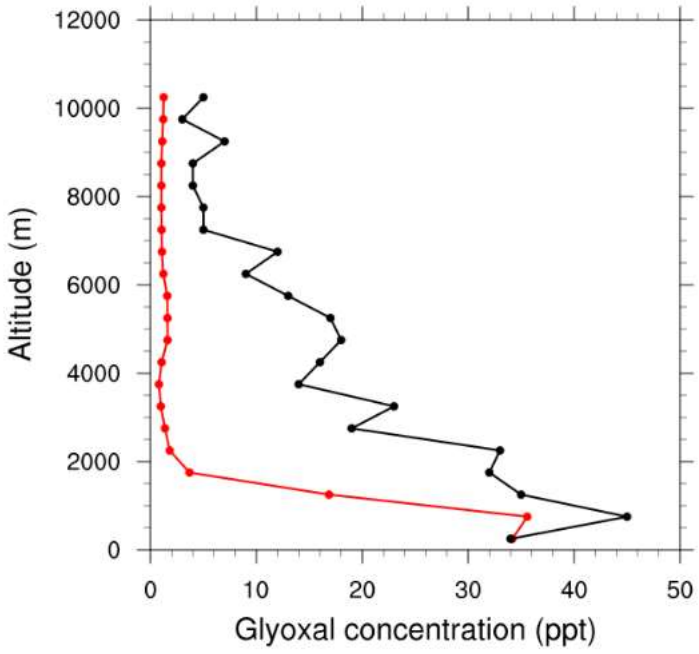

Figure 31 - The vertical profile of glyoxal measured by Volkamer et al. (2015) during RF17, and the vertical profile in the corresponding location and month from the model simulation with marine glyoxal production included.

The impact of glyoxal is significant in terms of its major sink. Over 60% of glyoxal removal is from photolysis and produces CO and HO2, and 14% of glyoxal removal is from OH oxidation. Globally, the impact of marine glyoxal locates over the tropics and the mid-high latitudes, shown in Figure 33. HO_2 and H_2O_2, which is an atmospheric oxidant with a longer lifetime than HO_x radicals and mainly come from HO_2 over the remote region, increases where significant glyoxal production locates. OH decreases in the tropics because of the increased glyoxal speed up the reaction between glyoxal and OH, which can offset the OH increase due to the reaction between HO_2 and NO or O_3, leading to an OH decrease. Over the mid-high latitude region, OH slightly increases, because the glyoxal peak in the mid-high latitude is corresponding with the local summer when the major sink of glyoxal is photo-oxidation. Then the strong increase

of HO_2 speeds up the reaction with NO and O3 and produces OH. Over the region with higher remote NO (e.g. the North Atlantic, where the aircraft NO_x emission is significant), the OH increase is more significant. In terms of the relative change of the oxidants over the remote region, Figure 32 shows the increase/decrease percentage of oxidants due to the marine glyoxal production over the MBL. The marine glyoxal increases the concentration of OH, HO_2, and H_2O_2 over the mid-high latitude ocean, especially over the Southern Ocean. In the summer of the southern hemisphere (December, January, and February), from 45°S to 75°S, the concentration of OH increases by 5.4%. The increasing percentage is 33.0% for HO_2 and 51.7% for H_2O_2. Because the background oxidation state of the Southern Ocean is very low, the enhancement of atmospheric oxidants over this region is very significant. This enhancement of the MBL oxidation state also leads to an increase in VOC oxidation reactivity. As shown in Figure 34(a), the reactivity of the OH oxidation of non-methane hydrocarbon (NMHC) in DJF over the Southern Ocean has increased by 51.5%. In addition, this oxidation state changes speeds up the oxidation of SO_2 and the partitioning of sulfate. SO_2 decreased by 11.7% in DJF over the Southern Ocean, also indicating a potential enhancement of the remote atmosphere acidity.

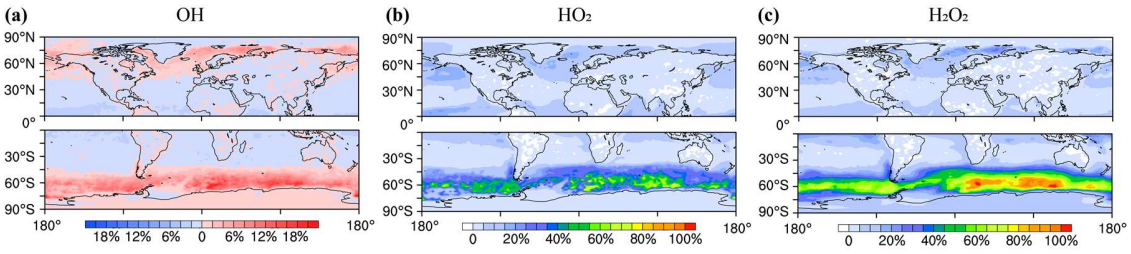

Figure 32 - The global distribution of the increase/decrease percentage of (a) OH, (b) HO_2, (c) H_2O_2 due to the marine glyoxal production averaged over the MBL(0-1km). In each panel, the top half is the JJA (summer in the northern hemisphere)

mean distribution in the northern hemisphere, and the bottom half is the DJF (summer in the southern hemisphere) mean distribution in the southern hemisphere.

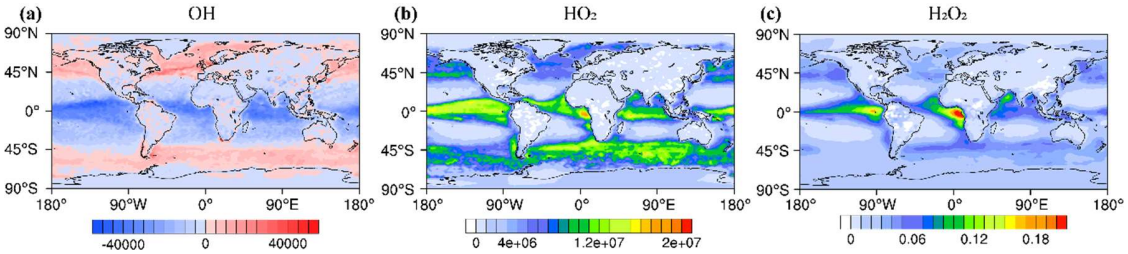

Figure 33 - The global distribution of the annual mean increase/decrease of (a) OH (unit: molecules/cm^3), (b) HO_2 (unit: molecules/cm^3) and (c) H_2O_2 (unit: ppb) due to the marine glyoxal production averaged over the MBL(0-1km).

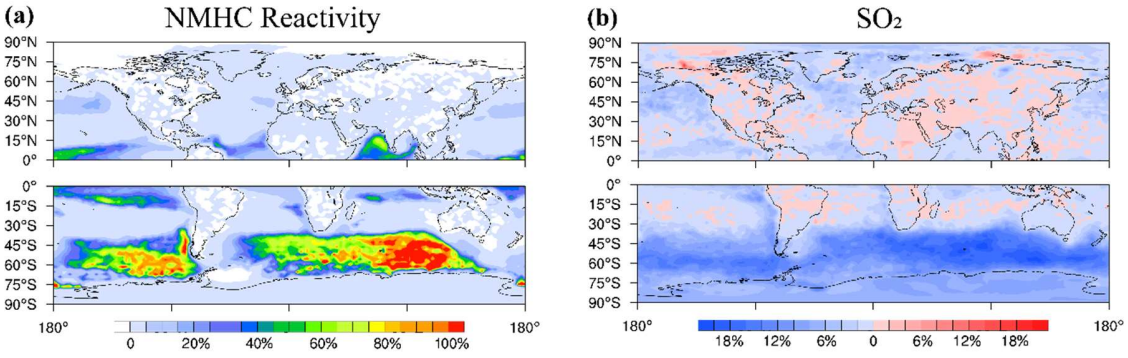

Figure 34 - The global distribution of the increase/decrease percentage of (a) The reactivity of the OH oxidation of non-methane hydrocarbon (NMHC), (b) SO_2 due to the marine glyoxal production averaged over the MBL(0-1km). In each panel, the top half is the JJA (summer in the northern hemisphere) mean distribution in the northern hemisphere, and the bottom half is the DJF (summer in the southern hemisphere) mean distribution in the southern hemisphere.

4.4 Conclusions

In this study, we estimated a potential marine biogenic glyoxal source using the inverse modeling based on the satellite observations. This is the first study to estimate marine glyoxal production including its mixing state in the MBL and explore the impact of glyoxal to the MBL oxidation state using CESM model simulation. Our estimation of

43 ± 10 Tg/yr marine glyoxal production is comparable with the land glyoxal budget of 45 Tg/yr (Fu et al., 2008). This estimation also agrees with a satellite-based estimation of the total mass ratio of marine glyoxal to the global glyoxal VCD, indicating that 48% of glyoxal is over the ocean. After including the marine glyoxal production, the model simulation results agree well with current ship and aircraft observations of surface and MBL glyoxal.

Because glyoxal production over the ocean is possibly secondary(Chiu et al., 2017), glyoxal may not be the only species in the complicate but unclear marine biogenic VOC system, our estimation glyoxal production from the ocean to MBL is a lower limit of the ocean biogenic emissions. In the future, with more VOC measurements in seawater and surface marine atmosphere, the relationship between glyoxal and other VOCs may lead to an estimation of a complete VOC budget in the MBL, which is important in terms of the knowledge of global background ozone, oxidation, and acidity. On the other hand, with a neural network model we developed (see supplement for detail), we can estimate the historical and future change of marine glyoxal production based on the temperature, solar radiation, and chlorophyll-A change. Furthermore, marine glyoxal is one of the major sources of marine SOA. Therefore, calculated based on an SOA yield of 12(Fu et al., 2008), we estimate a lower limit of 5.6 TgC/yr SOA production over MBL, which can help explain the high OC concentration measured over MBL.

One important implementation from this strengthened acidity is the dissolution of the metal in mineral dusts. The deposition of Fe and N on the ocean has increased, because of more aerosol pollutants from the pre-industrial period(Ito, Nenes, Johnson, Meskhidze, & Deutsch, 2016). Iron deposition from mineral dusts is closely related to

marine oxidation and acidity. Iron mobilization can occur in East Asia downwind regions through heterogeneous SO_2 oxidation in an acidified condition(Meskhidze, Chameides, Nenes, & Chen, 2003). When the soluble acidic substances deposit on to the aerosol surface, it can change the particles to be hydrophilic(Song & Carmichael, 2001). Since most Fe in the mineral dust from East Asia is in the form of Fe(III) in Fe_2O_3(Hseung & Jackson, 1952), oxidation is necessary for the mixed SO_2 to dissolve iron from mineral dust in East Asia outflow. Our results provide significant oxidation of SO_2 over MBL, which can further contribute to the iron deposition and enhancement of productivity over the north Pacific. Meanwhile, with the potentially rapid increase of anthropogenic emission in tropical Africa(Liousse, Assamoi, Criqui, Granier, & Rosset, 2014), the metal deposition from African dust may also enhance because of the high glyoxal-induced MBL acidity in the future.

CHAPTER 5. CONCLUSIONS AND FUTURE WORK

5.1 Summary of findings

5.1.1 The global impacts of BrC light absorption on the radiative balance

Observational evidence emerged from the DC3 mission of large enhancements of BrC relative to BC over biomass burning regions (Y. Zhang et al., 2017). We developed a module for simulating the effects of brown carbon light absorption in CESM CAM5. With the consideration of differential convective transport of BrC and BC, the simulated BrC DREs without (NCNB) and with (NCB) photo-bleaching is comparable to previous studies (Brown et al., 2018; Feng et al., 2013; Jo et al., 2016; X. Wang et al., 2018), and the evaluations with DC3, SEAC^{4}RS, and HIPPO observations suggested that the model could simulate the observed concentrations of BrC and BC, although model biases were also found.

We find that reducing the convective scavenging efficiency and including photo-bleaching is necessary to simulate the observed BrC distributions. Since the two factors have opposite effects on simulated BrC DRE, our best estimation of global DRE of BrC is 0.10 W/m^2. The BrC DRE is estimated to be 25% of that of BC. Since biomass burning emissions tend to occur during the warm seasons when solar insolation is strong and these emissions tend to occur in the tropics when convective transport is active, the proportional contribution to BrC DRE by biomass burning emission is larger than its fraction in the total emissions. For example, biofuel BrC emissions are seasonal and occur in mid and high latitudes, the combination of BrC absorption and solar radiation of biofuel BrC is less than

biomass burning BrC for a unit of BrC emission. Relative to BC DRE, BrC DRE tends to be larger in the tropics due to different emission distributions and larger BrC levels in the upper troposphere. BrC heating reduces global precipitation by 0.9%, about 60% of the BC induced precipitation decrease. Over the tropics, the reduction of precipitation due to BrC heating is similar to BC heating, but its effect on reducing tropical convective mass flux is only ~1/3 of BC heating because BrC heating is strongly skewed to high altitudes compared to BC heating. Consequently, the effect of BrC heating on tropical expansion is comparable to BC heating.

5.1.2 The feedback of African biomass burning due to the aerosol induced weather change.

We use RESFire model and address a positive feedback loop between fire and climate in Africa. In DJF, the maximum BF change because of BB aerosol feedback is located at 3.3° N, which is 4.7° south to the peak latitude of DJF BF over Africa. The maximum increase of BF in DJF accounts for 89% of local BF, and is 20% compared to the maximum zonal mean BF over Africa. In JJA the peak of BF change due to BB aerosol feedback is at 4.2° S, which is 8.5° north to the JJA peak latitude of BF over Africa. The maximum increase of BF in JJA accounts for 16% of local BF, and is 12% compared to the maximum zonal mean BF over Africa.

We discussed the mechanism of Biomass burning aerosol emissions increase CCN concentrations in the free troposphere and enhance solar heating, thus reduce precipitations and increase the fire activity. The fire feedback shifts to the region on the transport path of biomass burning aerosols, and regions over which the burning is sensitive to precipitations.

This positive feedback is recurrent in a meteorological time scale and has intraseasonal to interseasonal impact. This feedback suggests a mechanism contributing to the interannual fluctuation of African biomass burning, also plays a role in understanding the observed and modeled interannual trend of biomass burning in previous studies.

5.1.3 The impacts of marine glyoxal production on the MBL oxidation state.

We use the inverse modeling method to estimate marine glyoxal production, which is missing in current global models, based on the satellite observations and the CESM model. Our estimation of 43 ± 10 Tg/yr marine glyoxal production is similar to This estimation also agrees with a satellite-based estimation of the total mass ratio of marine glyoxal to the global glyoxal VCD, indicating that 48% of glyoxal is over the ocean. After including the marine glyoxal production, the model simulation results agree well with current ship and aircraft observations of surface and MBL glyoxal.

The marine glyoxal increases the concentration of major atmospheric oxidants e.g. OH, HO_2 and H_2O_2 over the mid-high latitude ocean, especially over the Southern Ocean. In the summer of the southern hemisphere (December, January, and February), from 45°S to 75°S, the concentration of OH increases by 5.4%. The increasing percentage is 33.0% for HO_2 and 51.7% for H_2O_2. The increase of atmospheric oxidation state leads to the acceleration of VOC oxidation and an increase of air acidity due to SO_2 oxidation.

5.2 Future work

5.2.1 The global model simulation of BrC constraining with ATom campaign

The Atmospheric Tomography Mission (ATom) is conducted by the NASA DC-8 research aircraft, which measures atmospheric chemistry compounds and aerosols along the Pacific and Atlantic Oceans from 180 m to ~13km (Prather et al., 2017). The flight tracks of the ATom missions are shown in Figure 35. The BrC measurement in ATom was conducted by Zeng et al. (2020), which includes ambient WSOC absorption measurement, which represents the light absorption of BrC, every 20 minutes during ATom-2 (January - February 2017), ATom-3 (September - October 2017) and ATom-4 (April - May 2018). BrC is not measured during ATom-1. During ATom-3 and ATom-4, the measurement includes further investigation of Antarctica.

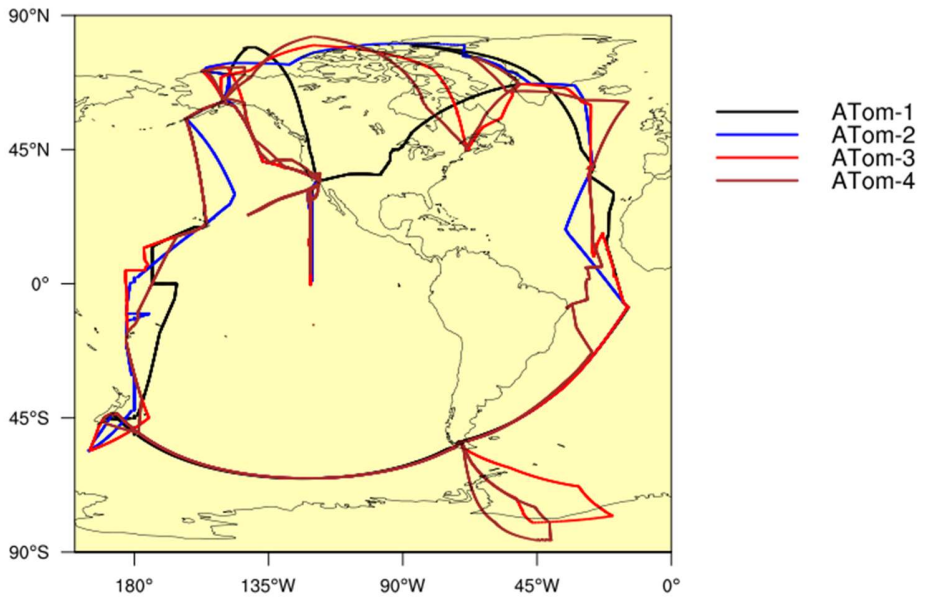

Figure 35 - The flight track of ATom missions.

In Section 2.6, we point out that BrC heating is potentially more than BC in the remote tropics, while the measurement of BrC in the remote regions are still missing. Now

with the ATom measurements, we are able to further understand the long-term transport and the physical-chemical processing of BrC over the remote regions.

Similar to the study in Chapter 2, to evaluate the model performance, we constrain the CESM model with the BC measurements in ATom-2 to ATom-4. Figure 36 shows the distribution of BC in the ATom mission (Katich et al., 2018). Compared to the BC measurement in HIPPO campaign, the ATom measurements show similar BC concentrations, zonal distributions, and vertical profiles to HIPPO over the Pacific Oceans. The ATom measurements over the Atlantic Oceans indicate a significant high-BC region over the tropics (10°S - 10°N), which is the outflow of African wildfire. This African outflow can transport as high as 5 km but is sharply removed in the upper troposphere. In addition, both the Pacific and the Atlantic region have high BC concentrations during ATom-3 over the upper troposphere (> 5 km) of the south polar region (50°S - 70°S). The back trajectory shows that the high-level BC in ATom-3 over the tropics and mid-latitude is related to the transport of continental biomass burning (Zeng et al., 2020), but the BC over polar regions is hard to trace using a 7-day back trajectory. Our previous analysis of fire dominated AOD (Figure 6) indicates that the model simulated polar BC is fire-dominated. Since the high BC concentration over the south polar region is only seen during ATom-3, when the fire is prevailing in both South America and Africa, this upper troposphere high BC is probably due to the long-term transport of biomass burning aerosols.

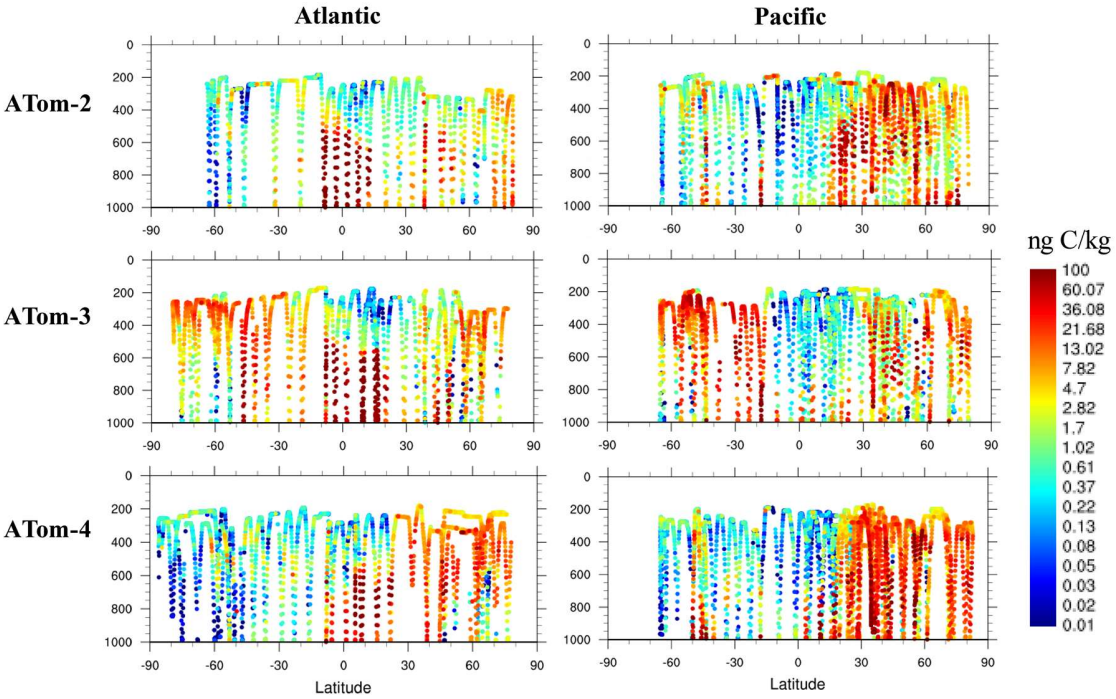

Figure 36 – The zonal distribution and vertical profile of ATom BC (ng C kg^{-1}) measurements The 3 rows from top to bottom are ATom-2 (Jan - Feb 2017), ATom-3 (Sep - Oct 2017) and ATom-4 (Apr - May 2018), respectively. Measurement data along the flight tracks of Figure 35 are 1-min averages. The region "Atlantic" represents the region to the east of 100°W, and the region "Pacific" represents the region to the west of 100°W.

We conducted 4 sensitivity runs to approach the measured BC in the CESM model. The result is shown in Figure 37. In the default model, the simulation significantly overestimates BC over the tropic upper troposphere and underestimates polar BC concentration. In order to fix the model bias over the tropics upper troposphere, we applied the aerosol secondary activation mechanism, which is necessary for the effective wet removal of BC (P. Yu et al., 2019). After including aerosol secondary activation, the tropical high bias of BC in the upper troposphere is significantly removed, but the model simulation underestimates more in all the other regions. Therefore, we applied the BC wet scavenging modification as described in Section 2.4.1, then we find a balance between all

bias. The model simulation including aerosol secondary activation and the scaling of wet scavenging agrees with the ATom-3 observations in the southern mid-high latitude regions and the northern hemisphere mid-latitudes, but still overestimates the BC over the tropics upper troposphere and underestimates the BC over the north polar free troposphere. The current model still cannot well produce the African outflow as the observation, indicating the limited knowledge of the convection transport mechanism in the tropics Atlantic Oceans.

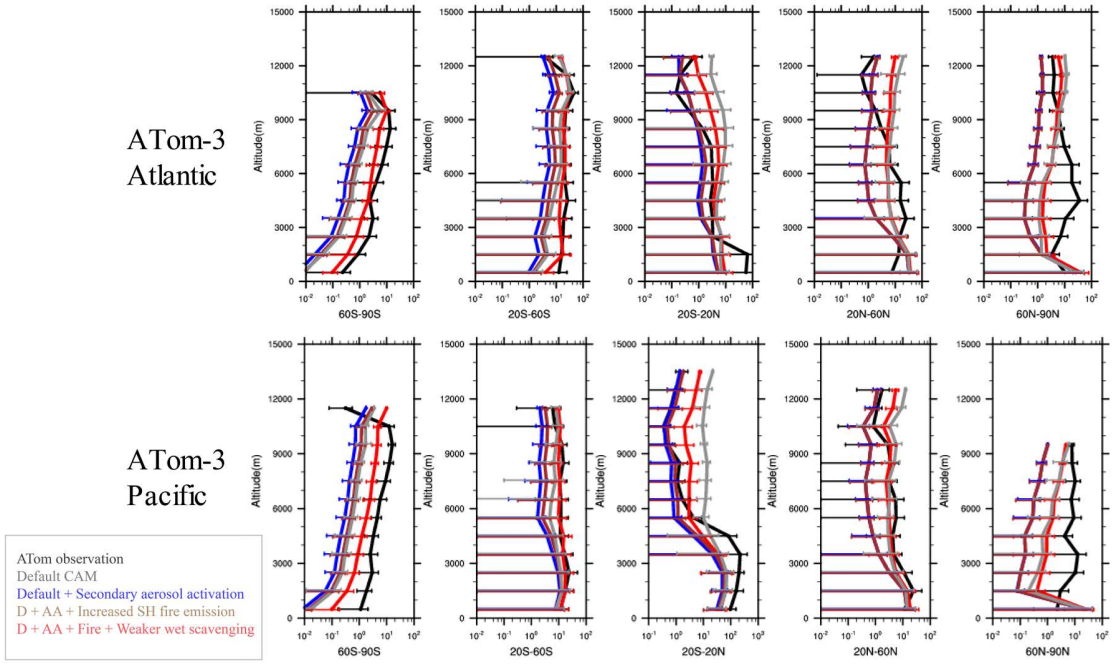

Figure 37 – The comparison among the model sensitivity runs and the ATom-3 measurements of BC (ng C kg^{-1}) in the latitude bins of 60°S - 90°S, 20°S - 60°S, 20°S - 20°N, 20°N - 60°N, 60°N - 90°N.

After this model evaluation, we plan to compare the model simulation of BrC with the BrC module discussed in Chapter 2 to the ATom BrC observations. Our preliminary results show that more than 70% of the remote BrC is below the measurement lower limit

of detection (LOD, which is 0.05 Mm^{-1} for ATom-2, 0.15 Mm^{-1} for ATom-3 and 0.10 Mm^{-1} for ATom-4). The model simulation results are also lower than the measurement LOD, indicating the potential agreement between the model and observation over the remote atmosphere, but the measurement accuracy will be a limit to the further investigation of remote BrC. On the other hand, BrC hotspots are found in the remote atmosphere especially over the polar region and the African outflow but are not simulated in the model, indicating the model is underestimating the transport of BrC in the specific fire plumes or deep convection events.

5.2.2 The biomass burning feedback due to the land cover change

In the future, we plan to simulate biomass burning feedback in the long term (> 10 years) focusing on the land cover change due to the biomass burning, using the RESFire model. The RESFire model introduces the long-term effect of biomass burning on the postfire land cover change and the change of the ecosystem structure (Li, Bond-Lamberty, & Levis, 2014; Zou et al., 2019). The land cover change not only affects the local fuel load of fire but also affect regional and global climate conditions, e.g. increasing surface albedo and decreasing the global radiative forcing (J. T. Randerson et al., 2006). We plan to conduct 2 100-year RESFire sensitivity runs to investigate the fire-climate interaction, and we propose to see long-term fluctuation and the corresponding mechanism behind it.

REFERENCES

Abatzoglou, J. T., Williams, A. P., & Barbero, R. (2019). Global emergence of anthropogenic climate change in fire weather indices. *Geophysical Research Letters, 46*(1), 326-336.

Abatzoglou, J. T., Williams, A. P., Boschetti, L., Zubkova, M., & Kolden, C. A. (2018). Global patterns of interannual climate–fire relationships. *Global change biology, 24*(11), 5164-5175.

Aguilar, E., Aziz Barry, A., Brunet, M., Ekang, L., Fernandes, A., Massoukina, M., . . . Peterson, T. (2009). Changes in temperature and precipitation extremes in western central Africa, Guinea Conakry, and Zimbabwe, 1955–2006. *Journal of Geophysical Research: Atmospheres, 114*(D2).

Akagi, S., Yokelson, R. J., Wiedinmyer, C., Alvarado, M., Reid, J., Karl, T., . . . Wennberg, P. (2011). Emission factors for open and domestic biomass burning for use in atmospheric models. *Atmospheric Chemistry and Physics, 11*(9), 4039-4072.

Alexander, D. T., Crozier, P. A., & Anderson, J. R. (2008). Brown carbon spheres in East Asian outflow and their optical properties. *Science, 321*(5890), 833-836.

Allen, R. J., Sherwood, S. C., Norris, J. R., & Zender, C. S. (2012). Recent Northern Hemisphere tropical expansion primarily driven by black carbon and tropospheric ozone. *Nature, 485*(7398), 350-354.

Alvarado, L., Richter, A., Vrekoussis, M., Wittrock, F., Hilboll, A., Schreier, S., & Burrows, J. (2014). An improved glyoxal retrieval from OMI measurements. *Atmospheric Measurement Techniques, 7*(12), 4133.

Andela, N., Morton, D., Giglio, L., Chen, Y., Van Der Werf, G., Kasibhatla, P., . . . Kloster, S. (2017). A human-driven decline in global burned area. *Science, 356*(6345), 1356-1362.

Anderson, L. O., Aragão, L. E., Gloor, M., Arai, E., Adami, M., Saatchi, S. S., . . . Berenguer, E. (2015). Disentangling the contribution of multiple land covers to fire‐mediated carbon emissions in Amazonia during the 2010 drought. *Global Biogeochemical Cycles, 29*(10), 1739-1753.

Andreae, M., & Rosenfeld, D. (2008). Aerosol–cloud–precipitation interactions. Part 1. The nature and sources of cloud-active aerosols. *Earth-Science Reviews, 89*(1-2), 13-41.

Ångström, A. (1964). The parameters of atmospheric turbidity. *Tellus, 16*(1), 64-75.

Aragão, L. E., Anderson, L. O., Fonseca, M. G., Rosan, T. M., Vedovato, L. B., Wagner, F. H., . . . Aguiar, A. P. (2018). 21st Century drought-related fires counteract the decline of Amazon deforestation carbon emissions. *Nature communications, 9*(1), 536.

Arora, V. K., & Melton, J. R. (2018). Reduction in global area burned and wildfire emissions since 1930s enhances carbon uptake by land. *Nature communications, 9*(1), 1326.

Barth, M. C., Cantrell, C. A., Brune, W. H., Rutledge, S. A., Crawford, J. H., Huntrieser, H., . . . Pickering, K. E. (2015). The deep convective clouds and chemistry (DC3) field campaign. *Bulletin of the American Meteorological Society, 96*(8), 1281-1309.

Bond, T. C., & Bergstrom, R. W. (2006). Light absorption by carbonaceous particles: An investigative review. *Aerosol science and technology, 40*(1), 27-67.

Bond, T. C., Bhardwaj, E., Dong, R., Jogani, R., Jung, S., Roden, C., . . . Trautmann, N. M. (2007). Historical emissions of black and organic carbon aerosol from energy‐related combustion, 1850–2000. *Global Biogeochemical Cycles, 21*(2).

Bond, T. C., Doherty, S. J., Fahey, D., Forster, P., Berntsen, T., DeAngelo, B., . . . Koch, D. (2013). Bounding the role of black carbon in the climate system: A scientific assessment. *Journal of Geophysical Research: Atmospheres, 118*(11), 5380-5552.

Bond, W. J., Woodward, F. I., & Midgley, G. F. (2005). The global distribution of ecosystems in a world without fire. *New phytologist, 165*(2), 525-538.

Bowman, D. M., Balch, J. K., Artaxo, P., Bond, W. J., Carlson, J. M., Cochrane, M. A., . . . Harrison, S. P. (2009). Fire in the Earth system. *Science, 324*(5926), 481-484.

Bretherton, C. S., & Park, S. (2009). A new moist turbulence parameterization in the Community Atmosphere Model. *Journal of Climate, 22*(12), 3422-3448.

Brown, H., Liu, X., Feng, Y., Jiang, Y., Wu, M., Lu, Z., . . . Pokhrel, R. (2018). Radiative effect and climate impacts of brown carbon with the Community Atmosphere Model (CAM5). *Atmospheric Chemistry and Physics, 18*(24), 17745-17768.

Browne, E. C., Zhang, X., Franklin, J. P., Ridley, K. J., Kirchstetter, T. W., Wilson, K. R., . . . Kroll, J. H. (2019). Effect of heterogeneous oxidative aging on light absorption by biomass-burning organic aerosol. *Aerosol science and technology*(just-accepted), 1-15.

Burrows, J., Hölzle, E., Goede, A., Visser, H., & Fricke, W. (1995). SCIAMACHY—Scanning imaging absorption spectrometer for atmospheric chartography. *Acta Astronautica, 35*(7), 445-451.

Chakrabarty, R., Moosmüller, H., Chen, L.-W., Lewis, K., Arnott, W., Mazzoleni, C., . . . Kreidenweis, S. (2010). Brown carbon in tar balls from smoldering biomass combustion. *Atmospheric Chemistry and Physics, 10*(13), 6363-6370.

Cheng, Y., He, K.-B., Zheng, M., Duan, F.-K., Du, Z.-Y., Ma, Y.-L., . . . Zhang, X.-L. (2011). Mass absorption efficiency of elemental carbon and water-soluble organic carbon in Beijing, China. *Atmospheric Chemistry and Physics, 11*(22), 11497-11510.

Chipperfield, M. (2006). New version of the TOMCAT/SLIMCAT off‐line chemical transport model: Intercomparison of stratospheric tracer experiments. *Quarterly Journal of the Royal Meteorological Society, 132*(617), 1179-1203.

Chiu, R., Tinel, L., Gonzalez, L., Ciuraru, R., Bernard, F., George, C., & Volkamer, R. (2017). UV photochemistry of carboxylic acids at the air‐sea boundary: A relevant source of glyoxal and other oxygenated VOC in the marine atmosphere. *Geophysical Research Letters, 44*(2), 1079-1087.

Ciais, P., Sabine, C., Bala, G., Bopp, L., Brovkin, V., Canadell, J., . . . Heimann, M. (2014). Carbon and other biogeochemical cycles *Climate change 2013: the physical science basis. Contribution of Working Group I to the Fifth Assessment Report of the Intergovernmental Panel on Climate Change* (pp. 465-570): Cambridge University Press.

Coburn, S., Ortega, I., Thalman, R., Blomquist, B., Fairall, C., & Volkamer, R. (2014). Measurements of diurnal variations and eddy covariance (EC) fluxes of glyoxal in the tropical marine boundary layer: description of the Fast LED-CE-DOAS instrument. *Atmospheric Measurement Techniques, 7*(10), 3579-3595.

Costabile, F., Gilardoni, S., Barnaba, F., Ianni, A. D., Liberto, L. D., Dionisi, D., . . . Rinaldi, M. (2017). Characteristics of brown carbon in the urban Po Valley atmosphere. *Atmospheric Chemistry and Physics, 17*(1), 313-326.

De Gouw, J., Cooper, O., Warneke, C., Hudson, P., Fehsenfeld, F., Holloway, J., . . . Parrish, D. (2004). Chemical composition of air masses transported from Asia to the US West Coast during ITCT 2K2: Fossil fuel combustion versus biomass‐burning signatures. *Journal of Geophysical Research: Atmospheres, 109*(D23).

De Sales, F., Okin, G. S., Xue, Y., & Dintwe, K. (2019). On the effects of wildfires on precipitation in Southern Africa. *Climate Dynamics, 52*(1-2), 951-967.

Dentener, F., Kinne, S., Bond, T., Boucher, O., Cofala, J., Generoso, S., . . . Ito, A. (2006). Emissions of primary aerosol and precursor gases in the years 2000 and 1750 prescribed data-sets for AeroCom. *Atmospheric Chemistry and Physics, 6*(12), 4321-4344.

Desyaterik, Y., Sun, Y., Shen, X., Lee, T., Wang, X., Wang, T., & Collett, J. L. (2013). Speciation of "brown" carbon in cloud water impacted by agricultural biomass burning in eastern China. *Journal of Geophysical Research: Atmospheres, 118*(13), 7389-7399.

Di Lorenzo, R. A., Washenfelder, R. A., Attwood, A. R., Guo, H., Xu, L., Ng, N. L., . . . Young, C. J. (2017). Molecular-size-separated brown carbon absorption for biomass-burning aerosol at multiple field sites. *Environmental science & technology, 51*(6), 3128-3137.

Di Lorenzo, R. A., & Young, C. J. (2016). Size separation method for absorption characterization in brown carbon: Application to an aged biomass burning sample. *Geophysical Research Letters, 43*(1), 458-465.

Dinar, E., Taraniuk, I., Graber, E., Anttila, T., Mentel, T. F., & Rudich, Y. (2007). Hygroscopic growth of atmospheric and model humic ‐ like substances. *Journal of Geophysical Research: Atmospheres, 112*(D5).

Dubovik, O., Smirnov, A., Holben, B., King, M., Kaufman, Y., Eck, T., & Slutsker, I. (2000). Accuracy assessments of aerosol optical properties retrieved from Aerosol Robotic Network (AERONET) Sun and sky radiance measurements. *Journal of Geophysical Research: Atmospheres, 105*(D8), 9791-9806.

Edwards, P. M., Brown, S. S., Roberts, J. M., Ahmadov, R., Banta, R. M., Dubé, W. P., . . . Graus, M. (2014). High winter ozone pollution from carbonyl photolysis in an oil and gas basin. *Nature, 514*(7522), 351.

Feingold, G., Jiang, H., & Harrington, J. Y. (2005). On smoke suppression of clouds in Amazonia. *Geophysical Research Letters, 32*(2).

Feng, Y., Ramanathan, V., & Kotamarthi, V. R. (2013). Brown carbon: a significant atmospheric absorber of solar radiation? *Atmospheric Chemistry and Physics, 13*(17), 8607-8621. doi:10.5194/acp-13-8607-2013

Forrister, H., Liu, J., Scheuer, E., Dibb, J., Ziemba, L., Thornhill, K. L., . . . Schwarz, J. P. (2015). Evolution of brown carbon in wildfire plumes. *Geophysical Research Letters, 42*(11), 4623-4630.

Fu, T. M., Jacob, D. J., Palmer, P. I., Chance, K., Wang, Y. X., Barletta, B., . . . Pilling, M. J. (2007). Space ‐ based formaldehyde measurements as constraints on volatile organic compound emissions in east and south Asia and implications for ozone. *Journal of Geophysical Research: Atmospheres, 112*(D6).

Fu, T. M., Jacob, D. J., Wittrock, F., Burrows, J. P., Vrekoussis, M., & Henze, D. K. (2008). Global budgets of atmospheric glyoxal and methylglyoxal, and implications for formation of secondary organic aerosols. *Journal of Geophysical Research: Atmospheres, 113*(D15).

Gatti, L., Gloor, M., Miller, J., Doughty, C., Malhi, Y., Domingues, L., . . . Borges, V. (2014). Drought sensitivity of Amazonian carbon balance revealed by atmospheric measurements. *Nature, 506*(7486), 76.

Gettelman, A., Liu, X., Ghan, S. J., Morrison, H., Park, S., Conley, A., . . . Li, J. L. (2010). Global simulations of ice nucleation and ice supersaturation with an improved cloud scheme in the Community Atmosphere Model. *Journal of Geophysical Research: Atmospheres, 115*(D18).

Ghan, S. J. (2013). Technical Note: Estimating aerosol effects on cloud radiative forcing. *Atmospheric Chemistry and Physics, 13*(19), 9971-9974.

Ghan, S. J., Liu, X., Easter, R. C., Zaveri, R., Rasch, P. J., Yoon, J.-H., & Eaton, B. (2012). Toward a minimal representation of aerosols in climate models: Comparative decomposition of aerosol direct, semidirect, and indirect radiative forcing. *Journal of Climate, 25*(19), 6461-6476.

Giglio, L., Randerson, J. T., & Werf, G. R. (2013). Analysis of daily, monthly, and annual burned area using the fourth‐generation global fire emissions database (GFED4). *Journal of Geophysical Research: Biogeosciences, 118*(1), 317-328.

Greve, P., Orlowsky, B., Mueller, B., Sheffield, J., Reichstein, M., & Seneviratne, S. I. (2014). Global assessment of trends in wetting and drying over land. *Nature Geoscience, 7*(10), 716.

Hantson, S., Arneth, A., Harrison, S. P., Kelley, D. I., Prentice, I. C., Rabin, S. S., . . . Artaxo, P. (2016). The status and challenge of global fire modelling. *Biogeosciences, 13*(11), 3359-3375.

Heald, C. L., Ridley, D. A., Kroll, J., Barrett, S., Cady-Pereira, K., Alvarado, M. J., & Holmes, C. (2014). Contrasting the direct radiative effect and direct radiative forcing of aerosols. *Atmospheric Chemistry and Physics, 14*(11), 5513-5527.

Hecobian, A., Zhang, X., Zheng, M., Frank, N., Edgerton, E. S., & Weber, R. J. (2010). Water-Soluble Organic Aerosol material and the light-absorption characteristics of aqueous extracts measured over the Southeastern United States. *Atmospheric Chemistry and Physics, 10*(13), 5965-5977.

Hodnebrog, Ø., Myhre, G., Forster, P. M., Sillmann, J., & Samset, B. H. (2016). Local biomass burning is a dominant cause of the observed precipitation reduction in southern Africa. *Nature communications, 7*.

Hoffer, A., Gelencsér, A., Guyon, P., Kiss, G., Schmid, O., Frank, G., . . . Andreae, M. (2006). Optical properties of humic-like substances (HULIS) in biomass-burning aerosols. *Atmospheric Chemistry and Physics, 6*(11), 3563-3570.

Holben, B. N., Eck, T., Slutsker, I., Smirnov, A., Sinyuk, A., Schafer, J., . . . Dubovik, O. (2006). *AERONET's version 2.0 quality assurance criteria.* Paper presented at the Remote Sensing of the Atmosphere and Clouds.

Holben, B. N., Eck, T., Slutsker, I., Tanre, D., Buis, J., Setzer, A., . . . Nakajima, T. (1998). AERONET—A federated instrument network and data archive for aerosol characterization. *Remote Sensing of Environment, 66*(1), 1-16.

Hseung, Y., & Jackson, M. (1952). Mineral Composition of the Clay Fraction: III. of Some Main Soil Groups of China 1. *Soil Science Society of America Journal, 16*(3), 294-297.

Iacono, M. J., Delamere, J. S., Mlawer, E. J., Shephard, M. W., Clough, S. A., & Collins, W. D. (2008). Radiative forcing by long ‐ lived greenhouse gases: Calculations with the AER radiative transfer models. *Journal of Geophysical Research: Atmospheres, 113*(D13).

Ito, T., Nenes, A., Johnson, M., Meskhidze, N., & Deutsch, C. (2016). Acceleration of oxygen decline in the tropical Pacific over the past decades by aerosol pollutants. *Nature Geoscience, 9*(6), 443.

Jacobson, M. Z. (1999). Isolating nitrated and aromatic aerosols and nitrated aromatic gases as sources of ultraviolet light absorption. *Journal of Geophysical Research: Atmospheres, 104*(D3), 3527-3542.

Jacobson, M. Z. (2012). Investigating cloud absorption effects: Global absorption properties of black carbon, tar balls, and soil dust in clouds and aerosols. *Journal of Geophysical Research: Atmospheres, 117*(D6).

Jiang, Y., Lu, Z., Liu, X., Qian, Y., Zhang, K., Wang, Y., & Yang, X.-Q. (2016). Impacts of global open-fire aerosols on direct radiative, cloud and surface-albedo effects simulated with CAM5. *Atmospheric Chemistry & Physics, 16*(23).

Jo, D. S., Park, R. J., Lee, S., Kim, S.-W., & Zhang, X. (2016). A global simulation of brown carbon: implications for photochemistry and direct radiative effect. *Atmospheric Chemistry and Physics, 16*(5), 3413-3432. doi:10.5194/acp-16-3413-2016

Jolly, W. M., Cochrane, M. A., Freeborn, P. H., Holden, Z. A., Brown, T. J., Williamson, G. J., & Bowman, D. M. (2015). Climate-induced variations in global wildfire danger from 1979 to 2013. *Nature communications, 6*, 7537.

Junker, C., & Liousse, C. (2008). A global emission inventory of carbonaceous aerosol from historic records of fossil fuel and biofuel consumption for the period 1860–1997. *Atmospheric Chemistry and Physics, 8*(5), 1195-1207.

Katich, J., Schwarz, J., FROYD, K., Weinzierl, B., Dollner, M., Bui, T., . . . DEAN-DAY, J. (2018). ATom: Black Carbon Mass Mixing Ratios from ATom-1 Flights. *ORNL DAAC*.

Ke, Z. (2020). The Global Plume-rise Dataset and Its Climate Model Implement. *In Preparation*.

Kirchstetter, T., & Thatcher, T. (2012). Contribution of organic carbon to wood smoke particulate matter absorption of solar radiation. *Atmospheric Chemistry and Physics, 12*(14), 6067-6072.

Kirchstetter, T. W., Novakov, T., & Hobbs, P. V. (2004). Evidence that the spectral dependence of light absorption by aerosols is affected by organic carbon. *Journal of Geophysical Research: Atmospheres, 109*(D21).

Klimont, Z., Kupiainen, K., Heyes, C., Purohit, P., Cofala, J., Rafaj, P., . . . Schoepp, W. (2015). Global anthropogenic emissions of particulate matter: preparation.

Kloster, S., Mahowald, N., Randerson, J., & Lawrence, P. (2012). The impacts of climate, land use, and demography on fires during the 21st century simulated by CLM-CN. *Biogeosciences, 9*, 509-525.

Knox, A., Evans, G., Brook, J., Yao, X., Jeong, C.-H., Godri, K., . . . Slowik, J. (2009). Mass absorption cross-section of ambient black carbon aerosol in relation to chemical age. *Aerosol science and technology, 43*(6), 522-532.

Kumar, K. R., Sivakumar, V., Reddy, R., Gopal, K. R., & Adesina, A. J. (2013). Inferring wavelength dependence of AOD and Ångström exponent over a sub-tropical station in South Africa using AERONET data: Influence of meteorology, long-range transport and curvature effect. *Science of the Total Environment, 461*, 397-408.

Lamarque, J.-F., Bond, T. C., Eyring, V., Granier, C., Heil, A., Klimont, Z., . . . Owen, B. (2010). Historical (1850–2000) gridded anthropogenic and biomass burning emissions of reactive gases and aerosols: methodology and application. *Atmospheric Chemistry and Physics, 10*(15), 7017-7039.

Laskin, A., Laskin, J., & Nizkorodov, S. A. (2015). Chemistry of atmospheric brown carbon. *Chemical reviews, 115*(10), 4335-4382.

Laskin, J., Laskin, A., Nizkorodov, S. A., Roach, P., Eckert, P., Gilles, M. K., . . . Hu, Q. (2014). Molecular selectivity of brown carbon chromophores. *Environmental science & technology, 48*(20), 12047-12055.

Lavi, A., Lin, P., Bhaduri, B., Carmieli, R., Laskin, A., & Rudich, Y. (2017). Characterization of light-absorbing oligomers from reactions of phenolic compounds and Fe (III). *ACS Earth and Space Chemistry, 1*(10), 637-646.

Lawson, S., Selleck, P., Galbally, I., Keywood, M., Harvey, M., Lerot, C., . . . Ristovski, Z. (2015). Seasonal in situ observations of glyoxal and methylglyoxal over the temperate oceans of the Southern Hemisphere. *Atmospheric Chemistry and Physics, 15*(1), 223-240.

Lee, H. J., Aiona, P. K., Laskin, A., Laskin, J., & Nizkorodov, S. A. (2014). Effect of solar radiation on the optical properties and molecular composition of laboratory proxies of atmospheric brown carbon. *Environmental science & technology, 48*(17), 10217-10226.

Lerot, C., Stavrakou, T., Smedt, I. D., Müller, J.-F., & Roozendael, M. V. (2010). Glyoxal vertical columns from GOME-2 backscattered light measurements and comparisons with a global model. *Atmospheric Chemistry and Physics, 10*(24), 12059-12072.

Li, F., Bond-Lamberty, B., & Levis, S. (2014). Quantifying the role of fire in the Earth system–Part 2: Impact on the net carbon balance of global terrestrial ecosystems for the 20th century. *Biogeosciences, 11*(5), 1345-1360.

Liggio, J., Li, S.-M., & McLaren, R. (2005a). Heterogeneous reactions of glyoxal on particulate matter: Identification of acetals and sulfate esters. *Environmental science & technology, 39*(6), 1532-1541.

Liggio, J., Li, S. M., & McLaren, R. (2005b). Reactive uptake of glyoxal by particulate matter. *Journal of Geophysical Research: Atmospheres, 110*(D10).

Lin, P., Liu, J., Shilling, J. E., Kathmann, S. M., Laskin, J., & Laskin, A. (2015). Molecular characterization of brown carbon (BrC) chromophores in secondary organic aerosol generated from photo-oxidation of toluene. *Physical Chemistry Chemical Physics, 17*(36), 23312-23325.

Liousse, C., Assamoi, E., Criqui, P., Granier, C., & Rosset, R. (2014). Explosive growth in African combustion emissions from 2005 to 2030. *Environmental Research Letters, 9*(3), 035003.

Liu, J., Bergin, M., Guo, H., King, L., Kotra, N., Edgerton, E., & Weber, R. (2013). Size-resolved measurements of brown carbon in water and methanol extracts and estimates of their contribution to ambient fine-particle light absorption. *Atmospheric Chemistry and Physics, 13*(24), 12389-12404.

Liu, J., Lin, P., Laskin, A., Laskin, J., Kathmann, S. M., Wise, M., . . . Shilling, J. E. (2016). Optical properties and aging of light-absorbing secondary organic aerosol. *Atmospheric Chemistry and Physics, 16*(19), 12815-12827.

Liu, J., Scheuer, E., Dibb, J., Ziemba, L. D., Thornhill, K., Anderson, B. E., . . . Bergin, M. (2014). Brown carbon in the continental troposphere. *Geophysical Research Letters, 41*(6), 2191-2195.

Liu, X., Easter, R. C., Ghan, S. J., Zaveri, R., Rasch, P., Shi, X., . . . Vitt, F. (2012). Toward a minimal representation of aerosols in climate models: Description and evaluation in the Community Atmosphere Model CAM5. *Geoscientific Model Development, 5*(3), 709.

Liu, Y., Goodrick, S., & Heilman, W. (2014). Wildland fire emissions, carbon, and climate: Wildfire–climate interactions. *Forest Ecology and Management, 317*, 80-96.

Liu, Z., Wang, Y., Vrekoussis, M., Richter, A., Wittrock, F., Burrows, J. P., . . . Wang, H. (2012). Exploring the missing source of glyoxal (CHOCHO) over China. *Geophysical Research Letters, 39*(10).

Ma, P. L., Rasch, P. J., Wang, H., Zhang, K., Easter, R. C., Tilmes, S., . . . Lamarque, J. F. (2013). The role of circulation features on black carbon transport into the Arctic in the Community Atmosphere Model version 5 (CAM5). *Journal of Geophysical Research: Atmospheres, 118*(10), 4657-4669.

Magalhães, A. C. O., Esteves da Silva, J. C., & Pinto da Silva, L. s. (2017). Density functional theory calculation of the absorption properties of brown carbon chromophores generated by catechol heterogeneous ozonolysis. *ACS Earth and Space Chemistry, 1*(6), 353-360.

Martin, R. V., Jacob, D. J., Chance, K., Kurosu, T. P., Palmer, P. I., & Evans, M. J. (2003). Global inventory of nitrogen oxide emissions constrained by space ‐ based observations of NO2 columns. *Journal of Geophysical Research: Atmospheres, 108*(D17).

McMeeking, G. R. (2008). *The optical, chemical, and physical properties of aerosols and gases emitted by the laboratory combustion of wildland fuels*: ProQuest.

Meskhidze, N., Chameides, W., Nenes, A., & Chen, G. (2003). Iron mobilization in mineral dust: Can anthropogenic SO2 emissions affect ocean productivity? *Geophysical Research Letters, 30*(21).

Mlawer, E. J., Taubman, S. J., Brown, P. D., Iacono, M. J., & Clough, S. A. (1997). Radiative transfer for inhomogeneous atmospheres: RRTM, a validated correlated ‐ k model for the longwave. *Journal of Geophysical Research: Atmospheres, 102*(D14), 16663-16682.

Moritz, M. A., Batllori, E., Bradstock, R. A., Gill, A. M., Handmer, J., Hessburg, P. F., . . . Schoennagel, T. (2014). Learning to coexist with wildfire. *Nature, 515*(7525), 58.

Morrison, H., & Gettelman, A. (2008). A new two-moment bulk stratiform cloud microphysics scheme in the Community Atmosphere Model, version 3 (CAM3). Part I: Description and numerical tests. *Journal of Climate, 21*(15), 3642-3659.

Mungall, E. L., Abbatt, J. P., Wentzell, J. J., Lee, A. K., Thomas, J. L., Blais, M., . . . Willis, M. D. (2017). Microlayer source of oxygenated volatile organic compounds in the

summertime marine Arctic boundary layer. *Proceedings of the National Academy of Sciences, 114*(24), 6203-6208.

Nakayama, T., Matsumi, Y., Sato, K., Imamura, T., Yamazaki, A., & Uchiyama, A. (2010). Laboratory studies on optical properties of secondary organic aerosols generated during the photooxidation of toluene and the ozonolysis of α - pinene. *Journal of Geophysical Research: Atmospheres, 115*(D24).

Nakayama, T., Sato, K., Matsumi, Y., Imamura, T., Yamazaki, A., & Uchiyama, A. (2013). Wavelength and NO x dependent complex refractive index of SOAs generated from the photooxidation of toluene. *Atmospheric Chemistry and Physics, 13*(2), 531-545.

NASA Goddard Space Flight Center, O. E. L., Ocean Biology Processing Group. (2014). *Sea-viewing Wide Field-of-view Sensor (SeaWiFS) Ocean Color Data, NASA OB.DAAC.*

Neale, R. B., Chen, C.-C., Gettelman, A., Lauritzen, P. H., Park, S., Williamson, D. L., . . . Lamarque, J.-F. (2010). Description of the NCAR community atmosphere model (CAM 5.0). *NCAR Tech. Note NCAR/TN-486+ STR*.

Nguyen, T. B., Lee, P. B., Updyke, K. M., Bones, D. L., Laskin, J., Laskin, A., & Nizkorodov, S. A. (2012). Formation of nitrogen - and sulfur - containing light - absorbing compounds accelerated by evaporation of water from secondary organic aerosols. *Journal of Geophysical Research: Atmospheres, 117*(D1).

Niang, I., Ruppel, O., Abdrabo, M., Essel, A., Lennard, C., Padgham, J., & Urquhart, P. (2014). Africa Climate Change 2014: Impacts, Adaptation, and Vulnerability. Part B: Regional Aspects. Contribution of Working Group II to the Fifth Assessment Report of the Intergovernmental Panel on Climate Change ed VR Barros et al: Cambridge Univ Press, Cambridge, UK.

O'Dowd, C. D., Facchini, M. C., Cavalli, F., Ceburnis, D., Mircea, M., Decesari, S., . . . Putaud, J.-P. (2004). Biogenically driven organic contribution to marine aerosol. *Nature, 431*(7009), 676.

Odum, J. R., Jungkamp, T., Griffin, R. J., Forstner, H., Flagan, R. C., & Seinfeld, J. H. (1997). Aromatics, reformulated gasoline, and atmospheric organic aerosol formation. *Environmental science & technology, 31*(7), 1890-1897.

Park, R. J., Kim, M. J., Jeong, J. I., Youn, D., & Kim, S. (2010). A contribution of brown carbon aerosol to the aerosol light absorption and its radiative forcing in East Asia. *Atmospheric Environment, 44*(11), 1414-1421.

Park, S., & Bretherton, C. S. (2009). The University of Washington shallow convection and moist turbulence schemes and their impact on climate simulations with the Community Atmosphere Model. *Journal of Climate, 22*(12), 3449-3469.

Pechony, O., & Shindell, D. T. (2010). Driving forces of global wildfires over the past millennium and the forthcoming century. *Proceedings of the National Academy of Sciences, 107*(45), 19167-19170.

Pillar, E. A., Camm, R. C., & Guzman, M. I. (2014). Catechol oxidation by ozone and hydroxyl radicals at the air–water interface. *Environmental science & technology, 48*(24), 14352-14360.

Pillar, E. A., & Guzman, M. I. (2017). Oxidation of substituted catechols at the air–water interface: Production of carboxylic acids, quinones, and polyphenols. *Environmental science & technology, 51*(9), 4951-4959.

Platnick, S., King, M., Meyer, K., Wind, G., Amarasinghe, N., Marchant, B., . . . Ridgway, B. (2017). MODIS Atmosphere L3 Monthly Product. NASA MODIS Adaptive Processing System, Goddard Space Flight Center, USA.

Prather, M. J., Zhu, X., Flynn, C. M., Strode, S. A., Rodriguez, J. M., Steenrod, S. D., . . . Horowitz, L. W. (2017). Global atmospheric chemistry-which air matters. *Atmospheric Chemistry and Physics, 17*(14), 9081-9102.

Randerson, J., Chen, Y., Werf, G., Rogers, B., & Morton, D. (2012). Global burned area and biomass burning emissions from small fires. *Journal of Geophysical Research: Biogeosciences, 117*(G4).

Randerson, J. T., Liu, H., Flanner, M. G., Chambers, S. D., Jin, Y., Hess, P. G., . . . Welp, L. (2006). The impact of boreal forest fire on climate warming. *Science, 314*(5802), 1130-1132.

Remer, L., Mattoo, S., Levy, R., & Munchak, L. (2013). MODIS 3 km aerosol product: algorithm and global perspective. *Atmospheric Measurement Techniques, 6*(7), 1829.

Richter, J. H., & Rasch, P. J. (2008). Effects of convective momentum transport on the atmospheric circulation in the Community Atmosphere Model, version 3. *Journal of Climate, 21*(7), 1487-1499.

Rienecker, M. M., Suarez, M., Todling, R., Bacmeister, J., Takacs, L., Liu, H., . . . Gelaro, R. (2008). The GEOS-5 Data Assimilation System: Documentation of Versions 5.0. 1, 5.1. 0, and 5.2. 0.

Rinaldi, M., Decesari, S., Carbone, C., Finessi, E., Fuzzi, S., Ceburnis, D., . . . Vrekoussis, M. (2011). Evidence of a natural marine source of oxalic acid and a possible link to glyoxal. *Journal of Geophysical Research: Atmospheres, 116*(D16).

Saleh, R., Marks, M., Heo, J., Adams, P. J., Donahue, N. M., & Robinson, A. L. (2015). Contribution of brown carbon and lensing to the direct radiative effect of carbonaceous aerosols from biomass and biofuel burning emissions. *Journal of Geophysical Research: Atmospheres, 120*(19), 10,285-210,296.

Saleh, R., Robinson, E. S., Tkacik, D. S., Ahern, A. T., Liu, S., Aiken, A. C., . . . Yokelson, R. J. (2014). Brownness of organics in aerosols from biomass burning linked to their black carbon content. *Nature Geoscience, 7*(9), 647-650.

Sareen, N., Moussa, S. G., & McNeill, V. F. (2013). Photochemical aging of light-absorbing secondary organic aerosol material. *The Journal of Physical Chemistry A, 117*(14), 2987-2996.

Schulz, M., Textor, C., Kinne, S., Balkanski, Y., Bauer, S., Berntsen, T., . . . Guibert, S. (2006). Radiative forcing by aerosols as derived from the AeroCom present-day and pre-industrial simulations.

Schuster, G., Dubovik, O., & Arola, A. (2016). Remote sensing of soot carbon–Part 1: Distinguishing different absorbing aerosol species. *Atmospheric Chemistry and Physics, 16*(3), 1565-1585.

Schuster, G., Dubovik, O., Arola, A., Eck, T., & Holben, B. (2016). Remote sensing of soot carbon–Part 2: Understanding the absorption Ångström exponent. *Atmospheric Chemistry and Physics, 16*(3), 1587-1602.

Seaman, V. Y., Charles, M. J., & Cahill, T. M. (2006). A sensitive method for the quantification of acrolein and other volatile carbonyls in ambient air. *Analytical chemistry, 78*(7), 2405-2412.

Shapiro, E. L., Szprengiel, J., Sareen, N., Jen, C. N., Giordano, M. R., & McNeill, V. F. (2009). Light-absorbing secondary organic material formed by glyoxal in aqueous aerosol mimics. *Atmospheric Chemistry and Physics, 9*(7), 2289-2300.

Shim, C., Wang, Y., Choi, Y., Palmer, P. I., Abbot, D. S., & Chance, K. (2005). Constraining global isoprene emissions with Global Ozone Monitoring Experiment (GOME) formaldehyde column measurements. *Journal of Geophysical Research: Atmospheres, 110*(D24).

Sinreich, R., Coburn, S., Dix, B., & Volkamer, R. (2010). Ship-based detection of glyoxal over the remote tropical Pacific Ocean. *Atmospheric Chemistry and Physics, 10*(23), 11359-11371.

Sinreich, R., Volkamer, R., Filsinger, F., Frieß, U., Kern, C., Platt, U., . . . Wagner, T. (2007). MAX-DOAS detection of glyoxal during ICARTT 2004. *Atmospheric Chemistry and Physics, 7*(5), 1293-1303.

Smith, J. D., Kinney, H., & Anastasio, C. (2016). Phenolic carbonyls undergo rapid aqueous photodegradation to form low-volatility, light-absorbing products. *Atmospheric Environment, 126*, 36-44.

Song, C. H., & Carmichael, G. R. (2001). A three‐dimensional modeling investigation of the evolution processes of dust and sea‐salt particles in east Asia. *Journal of Geophysical Research: Atmospheres, 106*(D16), 18131-18154.

Spracklen, D. V., Mickley, L. J., Logan, J. A., Hudman, R. C., Yevich, R., Flannigan, M. D., & Westerling, A. L. (2009). Impacts of climate change from 2000 to 2050 on wildfire activity and carbonaceous aerosol concentrations in the western United States. *Journal of Geophysical Research: Atmospheres, 114*(D20).

Stohl, A., Klimont, Z., Eckhardt, S., Kupiainen, K., Shevchenko, V. P., Kopeikin, V., & Novigatsky, A. (2013). Black carbon in the Arctic: the underestimated role of gas flaring and residential combustion emissions. *Atmospheric Chemistry and Physics, 13*(17), 8833-8855.

Suarez, M. J., Rienecker, M., Todling, R., Bacmeister, J., Takacs, L., Liu, H., . . . Gelaro, R. (2008). The GEOS-5 Data Assimilation System-Documentation of Versions 5.0. 1, 5.1. 0, and 5.2. 0.

Toon, O. B., Maring, H., Dibb, J., Ferrare, R., Jacob, D. J., Jensen, E. J., . . . Pfister, L. (2016). Planning, implementation, and scientific goals of the Studies of Emissions and Atmospheric Composition, Clouds and Climate Coupling by Regional Surveys (SEAC4RS) field mission. *Journal of Geophysical Research: Atmospheres, 121*(9), 4967-5009.

Tosca, M., Diner, D., Garay, M., & Kalashnikova, O. (2015). Human‐caused fires limit convection in tropical Africa: First temporal observations and attribution. *Geophysical Research Letters, 42*(15), 6492-6501.

Updyke, K. M., Nguyen, T. B., & Nizkorodov, S. A. (2012). Formation of brown carbon via reactions of ammonia with secondary organic aerosols from biogenic and anthropogenic precursors. *Atmospheric Environment, 63*, 22-31.

Viovy, N. (2013). CRUNCEP Version 4–Atmospheric Forcing Data for the Community Land Model. *Research Data Archive at the National Center for Atmospheric Research, Computational and Information Systems Laboratory, Boulder CO, USA*.

Volkamer, R., Baidar, S., Campos, T. L., Coburn, S., DiGangi, J. P., Dix, B., . . . Ortega, I. (2015). Aircraft measurements of BrO, IO, glyoxal, NO 2, H 2 O, O 2–O 2 and aerosol extinction profiles in the tropics: Comparison with aircraft-/ship-based in situ and lidar measurements. *Atmospheric Measurement Techniques, 8*(5), 2121.

Wang, M., Ghan, S., Easter, R., Ovchinnikov, M., Liu, X., Kassianov, E., . . . Schanen, D. (2011). The multi-scale aerosol-climate model PNNL-MMF: Model description and evaluation. *Geoscientific Model Development, 4*(1), 137.

Wang, X., Heald, C., Ridley, D., Schwarz, J., Spackman, J., Perring, A., . . . Clarke, A. (2014a). Exploiting simultaneous observational constraints on mass and absorption to estimate the global direct radiative forcing of black carbon and brown carbon. *Atmospheric Chemistry and Physics, 14*(20), 10989-11010.

Wang, X., Heald, C., Ridley, D., Schwarz, J., Spackman, J., Perring, A., . . . Clarke, A. (2014b). Exploiting simultaneous observational constraints on mass and absorption to estimate the global direct radiative forcing of black carbon and brown carbon.

Wang, X., Heald, C. L., Liu, J., Weber, R. J., Campuzano-Jost, P., Jimenez, J. L., . . . Perring, A. E. (2018). Exploring the observational constraints on the simulation of brown carbon. *Atmospheric Chemistry and Physics, 18*(2), 635.

Wang, X., Heald, C. L., Sedlacek, A. J., de Sá, S. S., Martin, S. T., Alexander, M. L., . . . Artaxo, P. (2016). Deriving brown carbon from multiwavelength absorption measurements: method and application to AERONET and Aethalometer observations.

Ward, D. S., Kloster, S., Mahowald, N. M., Rogers, B. M., Randerson, J. T., & Hess, P. G. (2012). The changing radiative forcing of fires: global model estimates for past, present and future. *Atmospheric Chemistry and Physics, 12*(22), 10857-10886. doi:10.5194/acp-12-10857-2012

Washenfelder, R., Attwood, A., Brock, C., Guo, H., Xu, L., Weber, R., . . . Baumann, K. (2015). Biomass burning dominates brown carbon absorption in the rural southeastern United States. *Geophysical Research Letters, 42*(2), 653-664.

Wong, J. P., Nenes, A., & Weber, R. J. (2017). Changes in light absorptivity of molecular weight separated brown carbon due to photolytic aging. *Environmental science & technology, 51*(15), 8414-8421.

Wong, J. P., Tsagkaraki, M., Tsiodra, I., Mihalopoulos, N., Violaki, K., Kanakidou, M., . . . Weber, R. J. (2019). Atmospheric evolution of molecular-weight-separated brown carbon from biomass burning. *Atmospheric Chemistry and Physics, 19*(ARTICLE), 7319-7334.

Xiao, Y., Jacob, D. J., & Turquety, S. (2007). Atmospheric acetylene and its relationship with CO as an indicator of air mass age. *Journal of Geophysical Research: Atmospheres, 112*(D12).

Xie, M., Hays, M. D., & Holder, A. L. (2017). Light-absorbing organic carbon from prescribed and laboratory biomass burning and gasoline vehicle emissions. *Scientific Reports, 7*(1), 7318.

Yan, C., Zheng, M., Bosch, C., Andersson, A., Desyaterik, Y., Sullivan, A. P., . . . He, K. (2017). Important fossil source contribution to brown carbon in Beijing during winter. *Scientific Reports, 7*, 43182.

Yang, M., Howell, S., Zhuang, J., & Huebert, B. (2009). Attribution of aerosol light absorption to black carbon, brown carbon, and dust in China–interpretations of atmospheric measurements during EAST-AIRE. *Atmospheric Chemistry and Physics, 9*(6), 2035-2050.

Yang, Y., Saatchi, S. S., Xu, L., Yu, Y., Choi, S., Phillips, N., . . . Myneni, R. B. (2018). Post-drought decline of the Amazon carbon sink. *Nature communications, 9*(1), 3172.

Yoshimori, M., & Broccoli, A. J. (2008). Equilibrium response of an atmosphere–mixed layer ocean model to different radiative forcing agents: Global and zonal mean response. *Journal of Climate, 21*(17), 4399-4423.

Yu, L., Smith, J., Laskin, A., Anastasio, C., Laskin, J., & Zhang, Q. (2014). Chemical characterization of SOA formed from aqueous-phase reactions of phenols with the triplet excited state of carbonyl and hydroxyl radical. *Atmospheric Chemistry and Physics, 14*(24), 13801-13816.

Yu, L., Smith, J., Laskin, A., George, K. M., Anastasio, C., Laskin, J., . . . Zhang, Q. (2016). Molecular transformations of phenolic SOA during photochemical aging in the aqueous phase: competition among oligomerization, functionalization, and fragmentation. *Atmospheric Chemistry and Physics, 16*(7), 4511-4527.

Yu, P., Froyd, K. D., Portmann, R. W., Toon, O. B., Freitas, S. R., Bardeen, C. G., . . . Katich, J. M. (2019). Efficient in ‐ cloud removal of aerosols by deep convection. *Geophysical Research Letters, 46*(2), 1061-1069.

Zeng, L., Zhang, A., Wang, Y., Katich, J. M., Schwarz, J. P., Brock, C., . . . Weber, R. J. (2020). Brown Carbon Global Direct Radiative Effects. *In Preparation*.

Zhang, G., & McFarlane, N. A. (1995). Sensitivity of climate simulations to the parameterization of cumulus convection in the Canadian Climate Centre general circulation model. *Atmosphere-ocean, 33*(3), 407-446.

Zhang, Q., Streets, D. G., Carmichael, G. R., He, K., Huo, H., Kannari, A., . . . Fu, J. (2009). Asian emissions in 2006 for the NASA INTEX-B mission. *Atmospheric Chemistry and Physics, 9*(14), 5131-5153.

Zhang, X., Lin, Y. H., Surratt, J. D., Zotter, P., Prévôt, A. S., & Weber, R. J. (2011). Light ‐ absorbing soluble organic aerosol in Los Angeles and Atlanta: A contrast in secondary organic aerosol. *Geophysical Research Letters, 38*(21).

Zhang, Y., Forrister, H., Liu, J., Dibb, J., Anderson, B., Schwarz, J. P., . . . Wang, Y. (2017). Top-of-atmosphere radiative forcing affected by brown carbon in the upper troposphere. *Nature Geoscience, 10*(7), 486.

Zhao, R., Lee, A., Huang, L., Li, X., Yang, F., & Abbatt, J. (2015). Photochemical processing of aqueous atmospheric brown carbon. *Atmospheric Chemistry and Physics, 15*(11), 6087-6100.

Zhong, M., & Jang, M. (2011). Light absorption coefficient measurement of SOA using a UV–Visible spectrometer connected with an integrating sphere. *Atmospheric Environment, 45*(25), 4263-4271.

Zhong, M., Jang, M., Oliferenko, A., Pillai, G. G., & Katritzky, A. R. (2012). The SOA formation model combined with semiempirical quantum chemistry for predicting UV-Vis absorption of secondary organic aerosols. *Physical Chemistry Chemical Physics, 14*(25), 9058-9066.

Zhou, S., Gonzalez, L., Leithead, A., Finewax, Z., Thalman, R., Vlasenko, A., . . . Bureekul, S. (2014). Formation of gas-phase carbonyls from heterogeneous oxidation of polyunsaturated fatty acids at the air–water interface and of the sea surface microlayer. *Atmospheric Chemistry and Physics, 14*(3), 1371-1384.

Zhou, X., & Mopper, K. (1990). Measurement of sub-parts-per-billion levels of carbonyl compounds in marine air by a simple cartridge trapping procedure followed by liquid chromatography. *Environmental science & technology, 24*(10), 1482-1485.

Zhou, Y., Xu, K. M., Sud, Y., & Betts, A. (2011). Recent trends of the tropical hydrological cycle inferred from Global Precipitation Climatology Project and International Satellite Cloud Climatology Project data. *Journal of Geophysical Research: Atmospheres, 116*(D9).

Zhu, Y., & Kieber, D. J. (2019). Concentrations and Photochemistry of Acetaldehyde, Glyoxal, and Methylglyoxal in the Northwest Atlantic Ocean. *Environmental science & technology, 53*(16), 9512-9521.

Zou, Y., Wang, Y., Ke, Z., Tian, H., Yang, J., & Liu, Y. (2019). Development of a REgion‐Specific Ecosystem Feedback Fire (RESFire) Model in the Community Earth System Model. *Journal of advances in modeling earth systems, 11*(2), 417-445.